Robust Estimation of Road Friction Coefficient for Vehicle Active Safety Systems

by

Chang Sun Ahn

A dissertation submitted in partial fulfillment
of the requirements for the degree of
Doctor of Philosophy
(Mechanical Engineering)
in The University of Michigan
2011

Doctoral Committee:

Professor Huei Peng, Chair
Professor Timothy J. Gordon
Professor Jeffrey L. Stein
Assistant Professor Ryan M. Eustice

ACKNOWLEDGEMENTS

First and foremost I would like to express my gratitude to my advisor, Huei Peng, for his guidance, support, and motivation throughout my doctoral study. Without his encouragement, this dissertation and my doctoral study would not have been possible. I would also like to thank my committee members: Professor Timothy J. Gordon, Professor Jeffrey L. Stein, and Professor Ryan M. Eustice. Their advice and comments were greatly helpful to complete this dissertation.

I gratefully acknowledge the support from Ford Motor Company through the Ford-University of Michigan Innovation Alliance Project program. Particularly, my gratitude goes to Dr. H. Eric Tseng for his guidance, insights into vehicle dynamics, and care for my personal development. In addition, I would like to thank Mitch McConnell at Ford Motor Company for his assistance in the vehicle winter test.

My colleagues at the University of Michigan's Vehicle Dynamics Lab (VDL) have been crucial part of my life at Ann Arbor. Many thanks for the unforgettable years to my friends: Chiao-Ting Li, Sean Yang, Jongwha Yoon, Youseok Kou, William Smith, Shenbo Li, Byung-Joo Kim, and Tianyou Guo.

Finally, I would like to express my loving appreciation to my wife, Yeon Kim, and my mother. Their sustained love and support made this work possible.

TABLE OF CONTENTS

LIST OF FIGURES

LIST OF TABLES

LIST OF SYMBOLS

Symbol	Meaning
m	Vehicle mass
I_z	Vehicle yaw moment of inertia
v_x, v_y	Vehicle longitudinal and lateral velocity
F_{yf}	Lateral force at the front axle
F_{yr}	Lateral force at the rear axle
τ_a	Self-aligning moment of tire
a	Distance from the vehicle center of gravity to the front axle
b	Distance from the vehicle center of gravity to the rear axle
w	Length of tire tread
h	Height of the vehicle center of gravity
r	Yaw rate
δ	Tire steering angle
κ	Tire longitudinal slip ratio
α	Tire lateral slip angle
μ	Friction coefficient
c_p	Tread stiffness per unit length
l	Half of the contact patch length
W	Width of the contact patch
g	Gravity acceleration
φ_r	Road bank angle

Symbol	Meaning
φ_v	Vehicle roll angle
a_x	Vehicle longitudinal acceleration
a_y	Vehicle lateral acceleration
R_{xf}, R_{xr}	Rolling resistance of front and rear tires

ABSTRACT

Vehicle active safety systems stabilize the vehicle by controlling tire forces. They work well only when the tire force command computed by the safety systems is within the friction limit. Therefore, knowledge of the tire/road friction coefficient is important to improve their performance. The objective of this dissertation is to develop a robust friction coefficient estimation algorithm for vehicle active safety systems. The algorithm should be operational in a wide range of vehicle states, robust to plant uncertainties, and use information from sensors that are readily available on typical passenger vehicles.

This study presents two methods of estimating the friction coefficient: a lateral dynamics based method and a longitudinal dynamics based method. These two methods are then integrated to improve the working range and robustness of the estimator. The first method is a nonlinear observer based on vehicle lateral/yaw dynamics and the Brush tire model, whereas the second method is a recursive least squares method based on the relationship between tire longitudinal slip and traction force. The two methods are complementary to each other because they rely on different excitation conditions. Therefore, they can be integrated by a switching method where the switching signal depends on the level and kind of excitation.

The performance of the estimation algorithm was verified using simulations and test data under a wide range of friction and speed conditions. The test was performed on three different road surfaces: concrete, snow, and ice. The algorithm is able to estimate the friction coefficient of these three surfaces, including during abrupt surface changes and tracks the friction coefficient variance. It exhibits reasonable performance under various driving conditions based on the basic sensors used in vehicle stability control systems. The overall results from simulations and the experiments demonstrate that the proposed approach has the potential for practical applicability to vehicle active safety control.

CHAPTER 1
INTRODUCTION

1.1 Motivation

The safety of ground vehicles relies heavily on road friction. The risk of traffic accidents increases significantly on slippery surfaces [1]. Tire-road friction influences the ability of tires to generate steering, traction and braking forces, which in turn affect vehicle motions. Knowledge of the road friction coefficient is thus important for the design and analysis of active safety systems [2]. Examples of vehicle control systems that can benefit from the knowledge of tire-road friction include anti-lock braking systems (ABS), electronic stability control (ESC), adaptive cruise control, and collision warning or collision avoidance systems. The quality of traffic management and road maintenance work (e.g., salt application and snow plowing) can also be improved if the estimated friction value is communicated to the traffic and highway authorities.

With the rapid growth in hybrid vehicle sales, EPAS (Electric Power Assisted Steering) and AFS (Active Front Steering), both of which greatly enhance the overall X-by-wire implementation of future vehicles, are becoming more widely available. These advanced chassis control systems, similar to ESC, function well only when the road friction coefficient is known. When the road friction coefficient is unknown, the control design is usually conservative, resulting in reduced performance.

The penetration rate of electronic safety controllers has been increasing over the past decade. For example, a regulation of the U.S National Highway Traffic System Authority (NHTSA) requires all new vehicles lighter than 10,000lb to have ESC by 2011 [3]. TRW [4] forecasts that by 2010, 50% of all cars produced worldwide will incorporate some form of electrical assistance in their steering systems. These two systems (ESC and electric power steering) deploy sensors that provide useful information for the estimation of friction coefficient.

1.2 Problem Description

The tire-road friction coefficient, frequently referred as μ in the automotive engineering field, defines the ratio of the maximum horizontal force to the vertical forces acting between the vehicle's tires and the road. In other words, the friction coefficient quantifies the potential friction force that can be generated by vehicle tires. The horizontal tire forces, consisting of longitudinal and lateral components, are generated by braking, acceleration, and steering actions but are also affected by vehicle handling states. The vehicle performance in the horizontal plane is thus limited by the friction coefficient. This limitation can be represented by a friction circle, where the radius of the circle is the friction coefficient, as shown in Figure 1.1.

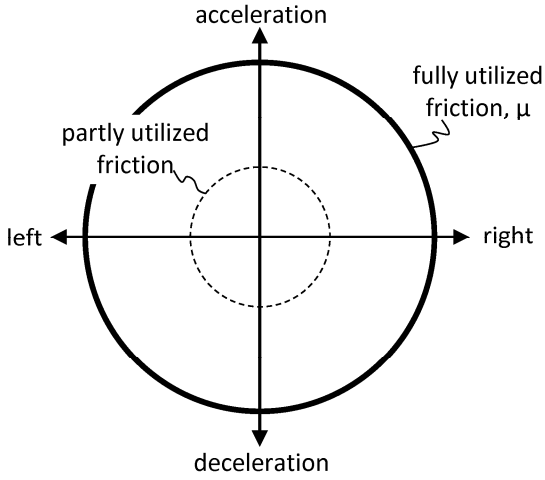

Figure 1.1 Friction circle of a tire [2]

Braking and traction torques induce longitudinal forces between the tire and road while steering produces lateral forces. The direction of the force generated when steering is combined with braking or acceleration is determined by magnitudes of the longitudinal and lateral tire relative deflections. Tire forces are generated by relative deflections between the tire contact patch and the road, referred to as tire slip, which is a major factor affecting tire forces. Furthermore, the friction coefficient affects not only the maximum magnitude of horizontal forces but also the sensitivity of tire force to the tire slip. An example of the relationship between tire force, friction coefficient, and tire slip is depicted in Figure 1.2.

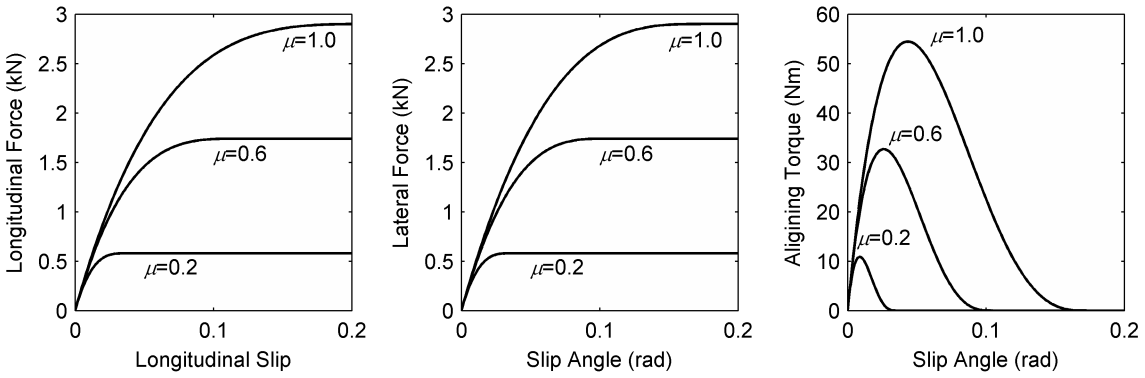

Figure 1.2 Tire force/moment characteristics [5]

Under normal driving conditions, excitations (steering or traction/braking) are small and it is difficult to calculate or infer the friction coefficient using the generated force and tire behavior models. This difficulty is due to the fact that uncontrolled factors (camber, vertical vibration, load transfer) or model uncertainties inject significant disturbances and thus the computed results may contain significant errors. Although it becomes easier to estimate the friction coefficient when excitations exceed the tire force limit, driving under these sliding or near-sliding conditions is risky as we are on the verge of losing grip, or have already lost grip. In addition, these conditions rarely occur in daily driving and cannot be introduced deliberately. Therefore, driving scenarios with "large enough" excitations are more useful for the purpose of friction coefficient estimation. In other words, while we will develop algorithms for estimating the road friction coefficient under small and extremely large excitations, it is the medium excitation results that are the most useful.

1.3 Literature Review

Many approaches to estimating tire-road friction have been proposed in the literature, with different requirements for sensors and levels of excitations. The estimation methods can be categorized into "cause-based" and "effect-based" approaches according to the fundamental phenomena. These approaches are depicted in Figure 1.3 and are reviewed in the following sub-sections.

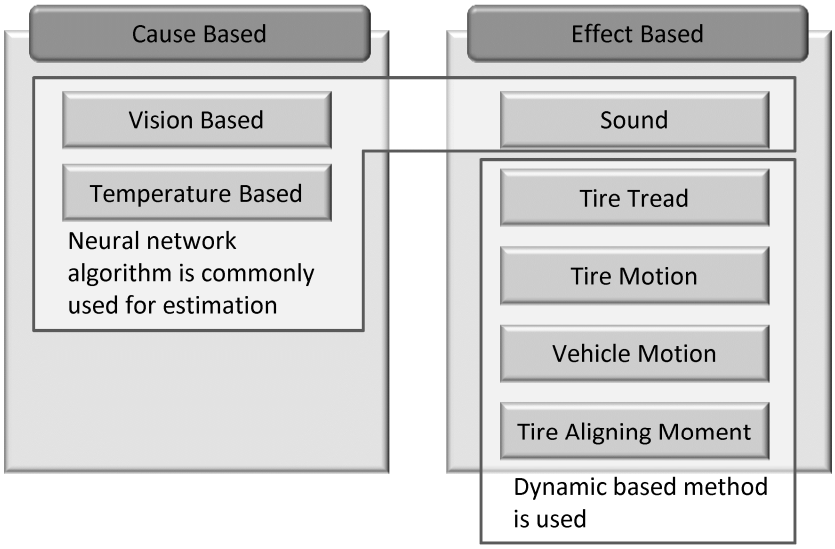

Figure 1.3 Classification of friction coefficient estimation algorithms

1.3.1 Vision/Temperature Based Methods

Holzmann [6] analyzed the texture of road images taken by camera to classify possible road types. The basic concept of Holzmann's work is that the image of a rough surface has a wider distribution of pixel luminance levels than the image of a smooth surface. His method provides six levels of predicted friction of the road ahead. However, the reliability of the texture analysis deteriorates when the image is blurred by vehicle speed and vibration. Sato [7] and Yamada [8] measured road wetness by detecting reflected light using optical sensors. These optical methods are effective in detecting road conditions, but are seriously affected by the intensity and direction of light.

Generally, vision information alone is not sufficient to estimate road conditions because many factors affect the road conditions which may not be easily discerned through this information exclusively. Therefore, when other pieces of information, such as temperature, are fused with vision information a more accurate estimate is obtained. Sato [7] fused three types of information: texture, reflected light, and temperature, using a fuzzy logic algorithm. He was able to differentiate between snow covered asphalt and snow covered ice using the fused algorithm.

These methods are called cause-based methods because they detect the factors affecting the tire-road friction. There are two potential advantages of these methods,

especially optical based methods: i) the friction coefficient of the road surface ahead of the vehicle may be detected, which enables preview and preemptive actions; and ii) estimation is possible without physical excitation, and could work well even when the vehicle is not being driven. These methods, however, only detect one aspect of road conditions. Therefore, other factors that affect tire force generation, such as tire types and wear/pressure, hydroplaning and change in normal load on driven wheels, are not taken into account. In other words, while these algorithms might have the potential to provide reliable and accurate estimation, they also have fundamental and inherent limitations due to their choice of detected phenomena.

1.3.2 Tire Tread Based Methods

Eichhorn [9] inserted strain sensors into tire treads to measure tire deformation and estimates the road friction coefficient by comparing the deformation at the center and edge of the contact patch. While the basic concept of Eichhorn'work is sound and has potential, this method, as the authors pointed out, is not a real-time algorithm and the verification was only done at low speeds. Tuononen [10, 11] estimated tire forces using tire carcass displacements measured by an LED sensor module. The measured signals were transmitted from the tires to the chassis through a wireless network. The displacement information was then processed and converted to tire force information that was being broadcasted through a CAN-bus. It is difficult to use these methods for production vehicles because of both the costs involved and technical challenges in embedding strain sensors and related power, signal conditioning and communication devices in tires.

1.3.3 Wheel Dynamics Based Methods

Ito [12] and Gustafsson [13] presented a road friction estimation method using wheel rotational behavior. When traction forces are applied to wheels, the resulting wheel speed difference between driven and non-driven wheels varies by road surface conditions. Consequently, road friction can be estimated. The same concept can also be applied during braking. However, it is well known that road friction estimation based on ABS/TCS excitations is generally inadequate due to controller intervention. Liu and Peng

[14] applied the special structure of the Brush tire model and used wheel speed signal to estimate the road friction coefficient and the cornering stiffness. Umeno [15] proposed a method based on frequency characteristics of wheel speed vibrations, which exhibit different resonance characteristics under different road conditions. Wheel dynamics based methods usually use wheel speed signals and tire traction/braking forces provided by a power train controller or electronic brake controller. Therefore, these methods do not require additional sensors and are easier to implement. However, the existing ABS/TCS sensors might not provide adequate accuracy, and, therefore, wheel-based estimation might require an upgrade of these sensors in order for the friction estimation methods to become feasible to use.

1.3.4 Vehicle Dynamics Based Methods

As indicated in the studies described below, vehicle dynamics based methods have advantages in robustness to disturbances. Andersson [2] presented an estimation method based on lateral excitation. He installed sensors in the steering system and in the front wheels to measure the tire self-aligning moment and he estimated the friction coefficient based on a Brush tire model. Using an input data set of tire lateral forces and the self-aligning moment measured using several force sensors installed at the suspension structures, Pasterkamp [16] proposed a neural network estimation algorithm based on a Brush tire model. Pal [17] applied the neural network based identification technique to predict the road friction coefficient based on steady-state vehicle response signals. Hahn [18] used lateral dynamics to estimate the friction coefficient, formulating an algorithm that specifically relied on GPS-based vehicle lateral speed. Sierra [19] utilized lateral dynamics, including lateral speed and yaw angular acceleration, to detect cornering stiffness, which is closely related to the friction coefficient. Yi [20] suggested an estimation algorithm based on vehicle longitudinal dynamics. He estimated tire traction forces using a power train model and detected the friction levels using the slip-traction force relationship.

These vehicle dynamics based methods are robust to high frequency disturbances due to the low bandwidth of the dynamics therefore these methods are preferable in case of using noisy sensors. An increasing penetration rate of active safety controllers along

with the availability of satellite-based position signals enable access to many vehicle dynamic states. Consequently, friction estimation based on vehicle dynamics has drawn increasing interest in recent years.

1.3.5 Tire Self-Aligning Moment Based Methods

Thanks to the introduction of electric power steering systems into passenger vehicles, access to the information of front tires' self-aligning moment is possible. The studies below incorporate the self-aligning moment in their methodology. Recently, Toyota published a series of papers [21-24] based on methods that involved either measuring the self-aligning moment or lateral compliance of the rotational shaft. The experimental results presented by Umeno [21] showed excellent estimation results (less than 5% error of forces up to 2500N) for both lateral force and the self-aligning moment by using the measurements from a resolver mechanism. Ono [24] used estimated tire forces and the self-aligning moment to calculate the 'tire grip margin', which indicates the remaining tire lateral force potential. He proposed an algorithm estimating the friction coefficient using the estimated 'tire grip margin'. Hsu [25] introduced an algorithm to estimate the friction coefficient using nonlinear least squares based on the self-aligning moment and GPS-based sideslip measurements. He also presented a nonlinear observer using the self-aligning moment and lateral acceleration in [26].

1.3.6 Summary

Table 1.1 shows a summary of the approaches reviewed in this section. Vision/ temperature based methods are typically not robust under environmental uncertainties. Tire tread based methods are impractical in today's environment because of the requirement for specially engineered strain sensors and power systems, both of which are costly and difficult to implement. Wheel dynamics based methods are inherently susceptible to high frequency disturbances, such as road roughness and ABS/TCS operations. However, if higher-precision wheel speed sensors are available and the effect of tire vertical motion can be eliminated, wheel-based methods have the advantage of fast response and may become a good choice. Lateral dynamics based methods with GPS are promising because GPS can provide several vehicle states, such as a vehicle side slip

angle that had previously been very difficult to obtain. The GPS used for the study of the literature is expensive, however, and the GPS signals require line-of-sight and are vulnerable to multi-path induced errors. Yet, notwithstanding these disadvantages, these methods deserve a second look in light of continued cost reduction and growing rates of GPS installation for vehicle navigation along with the prospect of having new European GPS system (Galileo) become available in a few years. Lateral dynamics based-methods using inertial sensors, which are reliable and cost effective, are already available in many active safety systems, such as ESC and ABS. Therefore, from a practical viewpoint, these methods appear to represent a good choice.

Table 1.1 Comparison of several estimation approaches

Category	Special sensors	Sensor reliability	Vulnerability	Cost	References
Vision/ temperature	Optical/Temperature sensor	Need clear vision	Snow, ice	High	[6], [7], [8], [9]
Tire tread	strain sensor	-	Sensor noise	High	[9], [10], [11]
Wheel dynamics	-	-	High frequency disturbances	Low	[12], [13], [14], [15]
Vehicle dynamics	D-GPS	Need line of sight	-	Medium	[18]
	Inertial	-	-	Low	[2], [16], [17], [19], [20]
Tire aligning moment	-	-	-	Low	[21], [24], [25], [26]

1.4 Objective, Approaches, and Scope of Study

The main objective of this research is to develop a robust and cost effective road friction estimation algorithm with a wide range of operation. Having adequate and rich excitations is crucial for the estimation algorithms. In ground vehicle applications, we do not have the luxury of choosing the level and type of excitations; the nature of excitations are typically dependent on the discretion of the driver, in response to road and traffic

conditions. Since we cannot actively impose excitations on the vehicle, it is expected that a single estimation approach would not be able to achieve reliable performance for all situations. For example, daily driving involves a lot of driving on straight roads, with only longitudinal excitations, and at very low excitation levels most of the time. In such situations, a road friction estimation method based on longitudinal dynamics and wheel dynamics [20] may be a viable choice, whereas a lateral dynamic based method will not be very useful. On the other hand, when adequate lateral excitations exist, a method based on vehicle lateral and steering system dynamics does become appropriate, as will be explained later in this study. Furthermore, under conditions involving extreme maneuvering of the vehicle (plowing out or spinning out), the algorithms based on normal maneuvers may not work appropriately. Therefore, it is necessary to develop and combine different approaches to form a comprehensive estimation strategy that works under a wide range of maneuvers.

The methods we aim to develop need to work under actual driving, and we plan to fully validate their performance using experimental data. The estimation algorithm will have to be robust against measurement noise and system uncertainties. Using both simulations and test results, we will study the achievable performance of the developed estimation algorithms, the proper fusion of different methods under different driving conditions, and the evaluation of the algorithm with respect to sensor accuracy, sensitivity to vehicle parameters and states, and excitation levels using both simulations and test results.

1.5 Contributions

Although knowledge of the frictional coefficient between tire and road is important for vehicle active safety systems, measuring or estimating the coefficient is challenging because it is a property of extreme phenomenon such as the skidding of tires. This dissertation focuses on the development of a friction coefficient estimation algorithm based on vehicle dynamics. Its major parts include a study of the physics relevant to the tire contact patch, mathematical derivation of a robust nonlinear observer,

and integration and implementation of the estimators. The main contributions of this work are summarized as follows:

- This research analyzes the physics related to the friction coefficient by using a tire model and a vehicle model. In particular, this work shows that the internal slip in the contact patch causes inconsistency between the physical tire models and experimental results in small longitudinal slip cases. The advantages and limitations of using tire physics and vehicle dynamics for parameter estimation are analyzed, and the inherent difficulty of using them for friction estimation is explained.
- A design methodology for parameter/state estimation of a class of nonlinear systems is proposed. The estimator is based on an adaptive observer to estimate states and parameters concurrently and guarantees local stability. Furthermore, an index for stability and robustness is suggested for the observer design process. Lyapunov stability conditions are numerically evaluated and the results are used as an index of stability and robustness. An optimal stable and robust observer is designed by optimizing the index. This design methodology can be used to determine estimator parameters such as observer gain for dynamic observers.
- In terms of contributions for applications, estimation algorithms for the friction coefficient will be formulated and divided into two groups based on the types of excitation they use: the first type of estimator is based on lateral excitation and involves a nonlinear least squares method and a nonlinear observer are designed; the second type of estimator is based on longitudinal excitation, and utilizes the relationship between the tire longitudinal stiffness and the friction coefficient at a small slip range. In addition, an integrated estimator will be formulated, combining the estimators from both types. This integrated estimator can work in combined slip cases as well as pure slip cases. Because the integrated estimator inherits the characteristics of the individual estimators, it works for both small and large excitations and has a wider operation range than single excitation based methods.

CHAPTER 2
SYSTEM MODELS

This chapter discusses the system models required for estimation. As discussed in the previous chapter, no single approach is likely to cover the wide range of vehicle maneuvers. Accordingly, combination of several different approaches will be used as the basis for the overall estimation method. In particular, when sufficient excitations exist in the lateral direction, vehicle lateral dynamics and the tire self-aligning moment will be used as the basis of estimation because of their robustness and the availability of related sensors. The 'low' excitation case is based on a vehicle longitudinal motion based algorithm. Four models will be introduced in this chapter: a vehicle lateral dynamic model, a vehicle longitudinal dynamic model, a tire force/moment model, and a steering system model.

2.1 Vehicle Lateral Dynamics Model

This section presents dynamic models to show vehicle excitation and response in the lateral and yawing directions. Models on both a level road and on a banked road are considered in the following sections. Tire vertical forces vary as the vehicle is in accelerated motion known as load transfer. A simple load transfer model will be described in Chapter 2.1.3 subsequent to the following introduction of vehicle models without load transfer.

2.1.1 Vehicle Model on a Level Road

The centerpiece of our estimation method is the vehicle bicycle model, which describes the vehicle lateral and yaw dynamics of a two-axle, one-rigid body ground vehicle, represented in Figure 2.1. Derivation of the equations of motion for the bicycle model follows from the force and moment balance:

$$
\begin{aligned}
m\left(\dot{v}_y + v_x r\right) &= F_{yf} + F_{yr}, \\
I_z \dot{r} &= aF_{yf} - bF_{yr},
\end{aligned}
\tag{2.1}
$$

where v_x is the vehicle forward speed, v_y is the vehicle lateral speed, r is the yaw rate, m is the vehicle mass, and I_z is the yaw moment of inertia. F_{yf} and F_{yr} are the lateral forces at the front and rear axle, respectively, δ is the front wheel steering angle, and a and b are the distances from the vehicle's center of gravity to front and rear axles. Using small angle approximations, the slip angles α_f and α_r of the front and rear tires in terms of v_x, v_y, and r are

$$
\begin{aligned}
\alpha_f &= \left(v_y + ar\right)/v_x - \delta, \\
\alpha_r &= \left(v_y - br\right)/v_x .
\end{aligned}
\tag{2.2}
$$

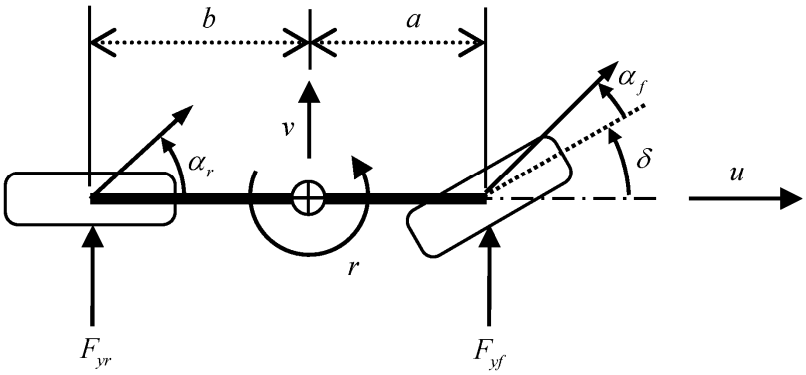

Figure 2.1 Vehicle bicycle model

This vehicle model is simple yet effective in representing vehicle lateral dynamics. This model has two degrees of freedom, one being lateral speed and the other yaw rate. The external forces to the model are from the front and rear tires. This means that if we know how the vehicle motions are changing, then we can know the tire forces. For example, from the vehicle lateral acceleration measured from an accelerometer, we can calculate the sum of the front and rear tire forces. Ignoring suspension roll, the sum of tire lateral force can be calculated by using the vehicle lateral acceleration measured at the center of mass as follows:

$$F_{yf} + F_{yr} = ma_{y,m}, \tag{2.3}$$

where $a_{y,m}$ is the measured lateral acceleration.

2.1.2 Vehicle Model on a Banked Road

Road bank angle is a common disturbance to vehicle lateral dynamics. This disturbance can be taken into account by using a road bank model as shown in Figure 2.2.

$$\begin{aligned} m\left(\dot{v}_y + v_x r\right) &= F_{yf} + F_{yr} + mg\sin(\varphi_r), \\ I_z \dot{r} &= aF_{yf} - bF_{yr}. \end{aligned} \tag{2.4}$$

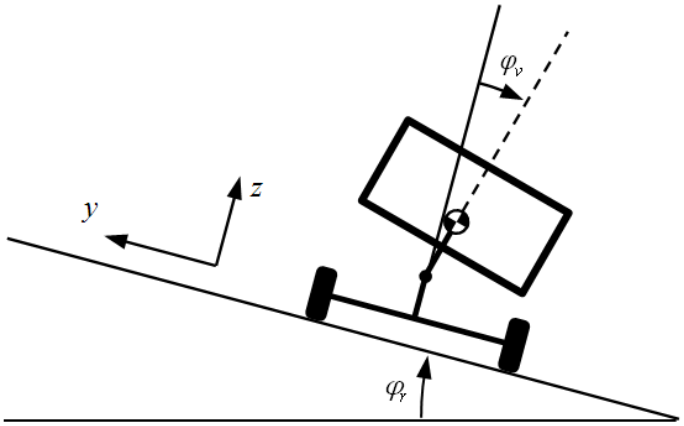

Figure 2.2 Vehicle on a banked road

In this case, the sum of the tire lateral forces is not the sole source for lateral acceleration because the accelerometer output is also affected by gravity, bank angle (φ_r), and vehicle roll angle (φ_v). The lateral acceleration at the center of mass located in the sprung mass is

$$a_{y,m} = \left(\dot{v}_y + v_x r\right)\cos(\varphi_v) - g\sin(\varphi_r + \varphi_v). \tag{2.5}$$

The relationship between the sum of lateral tire forces and measured lateral acceleration can then be derived from (2.4) and (2.5):

$$F_{yf} + F_{yr} = m\left(a_{y,m} + mg\sin(\varphi_r + \varphi_v)\right)/\cos(\varphi_v) - mg\sin(\varphi_r). \tag{2.6}$$

Note that (2.6) is the same as (2.3) if the road bank angle and vehicle roll angle are ignored. This equation demonstrates that if a vehicle is experiencing road bank or excessive roll motion, measuring lateral acceleration alone is not sufficient to determine tire lateral forces. Estimation or measurement of bank and roll is a challenging topic in research on vehicle dynamics. However, Tseng [27] successfully estimated road bank angle by decoupling the lateral dynamics and road bank disturbances. In addition, Ryu [28] estimated both the vehicle roll angle and the road bank angle using GPS sensors. Acknowledging both the importance of calculating these disturbances for real applications, and the difficulties of measuring them, we here assume, for the purposes of this research study, that these disturbances resulting from road bank angle and roll angle have been measured or estimated.

2.1.3 Load Transfer Model

Vertical loads exerted on vehicle tires vary as the vehicle experiences lateral and longitudinal acceleration. If we ignore vertical movement of vehicle mass, the vertical loads exerted on the tires can be calculated using longitudinal and lateral acceleration.

$$\begin{aligned}
F_{z,fl} &= \frac{1}{2}\left(\frac{b}{a+b}mg - \frac{h}{a+b}ma_x\right) - \frac{K_f}{K_f+K_r}\frac{h}{w}ma_y, \\
F_{z,fr} &= \frac{1}{2}\left(\frac{b}{a+b}mg - \frac{h}{a+b}ma_x\right) + \frac{K_f}{K_f+K_r}\frac{h}{w}ma_y, \\
F_{z,rl} &= \frac{1}{2}\left(\frac{a}{a+b}mg + \frac{h}{a+b}ma_x\right) - \frac{K_r}{K_f+K_r}\frac{h}{w}ma_y, \\
F_{z,rr} &= \frac{1}{2}\left(\frac{a}{a+b}mg + \frac{h}{a+b}ma_x\right) + \frac{K_r}{K_f+K_r}\frac{h}{w}ma_y,
\end{aligned} \tag{2.7}$$

where K_f is the roll stiffness of front suspension, and K_r is the roll stiffness of rear suspension. Lateral acceleration (a_y) in the equations is easily measured. However measurement of longitudinal acceleration (a_x) is not available in production vehicles. Thus, the longitudinal acceleration should be estimated using other available sensor

signals, such as the transmission output shaft speed, wheel speed of each tire, or GPS signals.

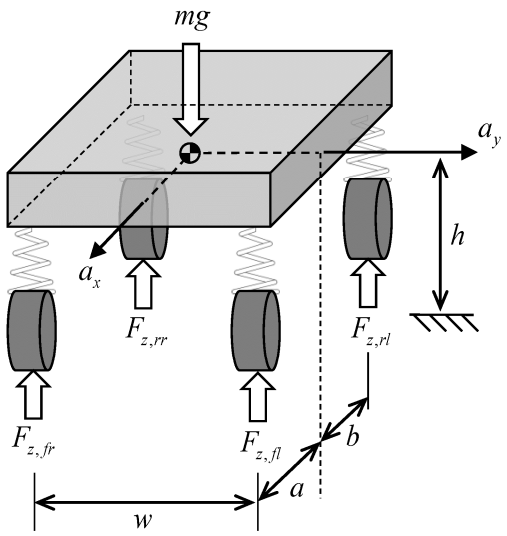

Figure 2.3 Load transfer model

2.2 Vehicle Longitudinal Dynamics Model

When a vehicle is under longitudinal forces such as straight driving on a highway, the vehicle dynamics are different from those explained in the previous chapter. The equation of motion can be derived by force equilibrium as shown in Figure 2.4 and the resulting equation is

$$ma_x = F_{xf} + F_{xr} - mg\sin\Theta - R_{xf} - R_{xr} - D_A, \tag{2.8}$$

where a_x is the longitudinal acceleration, F_{xf} and F_{xr} are the total tractive forces on the front and rear tires respectively, Θ is a road inclined angle, R_{xf} and R_{xr} are the rolling resistance of the front and rear tires respectively, and D_A is the aerodynamic drag force. The rolling resistance of a tire is usually determined by coast down tests. The aerodynamic drag force is proportional to velocity squared as follows:

$$D_A = \frac{C_d A \rho v_x^{\,2}}{2}, \tag{2.9}$$

where C_d is the drag coefficient and can be determined experimentally, A is the cross-sectional area of the vehicle, and ρ is the air density.

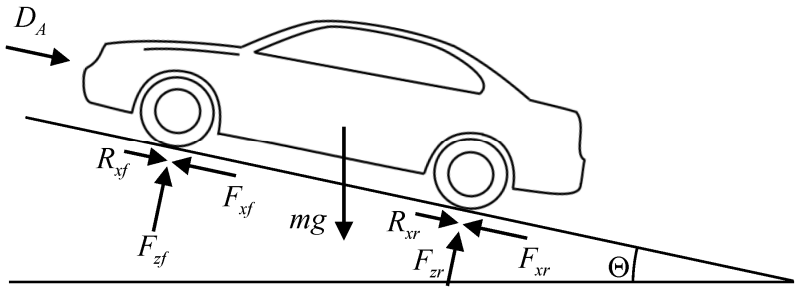

Figure 2.4 Forces related to vehicle longitudinal dynamics

The vehicle model above shows that if the rolling resistance is given and the vehicle is moving on a level surface, we can compute the total tractive force of the vehicle by measuring the longitudinal acceleration and velocity.

2.3 Tire Model

A tire model describes the relationship between tire parameters, tire dynamic states, and tire forces. Therefore, given tire forces, a tire model serves as the basis to estimate parameters, i.e. the friction coefficient. A linear tire model is commonly used for the vehicle bicycle model because it provides a good representation of tire behavior when the tire slip angle is small and the road frictional coefficient is high. Furthermore, with a linear tire model, the combined vehicle-tire bicycle model has a linear state space form. However, the linear tire model does not reflect the effect of friction variations. Many other tire models, such as the Magic Formula model [29] and the Brush model [5], have parameters that can capture this effect. Among the possible choices of existing models, we select the Brush model because it has fewer parameters compared to many other tire models [29-32] and it captures the effect of friction as well as nonlinearity when the tire slip angle increases.

The basic concept of the Brush model is that a tire consists of a row of elastic bristles which touch the road plane and can deflect in a direction that is parallel to the road surface. As a result, a tire can be modeled as a thin disk with brushes along the circumference that represent the tire treads, as shown in Figure 2.5. Treads in the contact

patch are compressed and experience vertical stresses. The distribution of vertical stress is assumed to be parabolic as shown in Figure 2.6. The parabolic distribution can be derived as follows:

$$\sigma_z(x) = \frac{3F_z}{2l}\frac{x}{l}\left(1-\frac{x}{2l}\right), \tag{2.10}$$

where F_z is the vertical tire load, l is half of the contact patch length, and x is the distance from the leading edge.

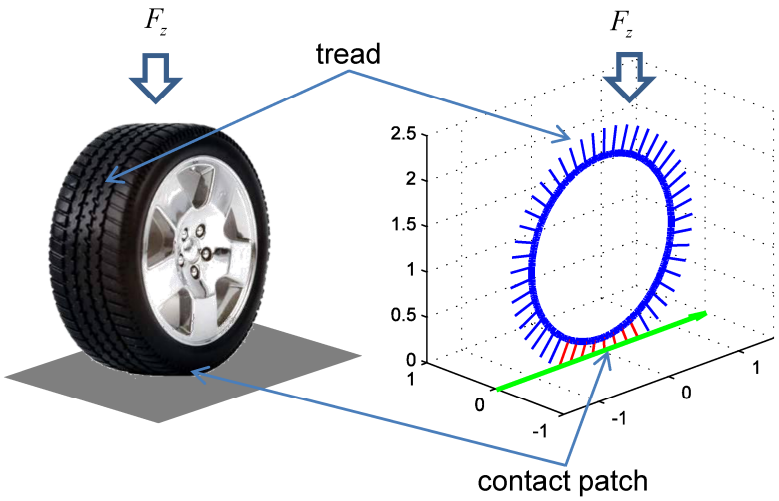

Figure 2.5 Tire and Brush model

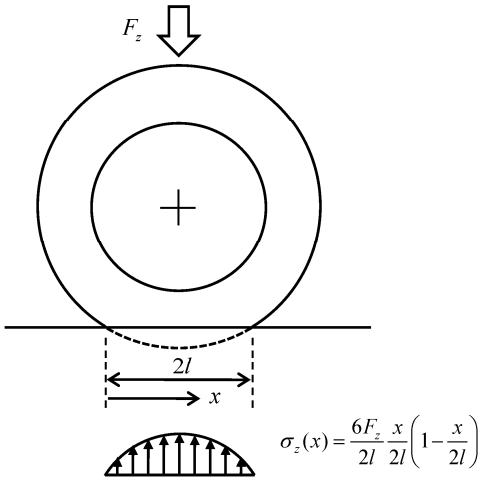

Figure 2.6 Pressure distribution in the contact patch of the Brush model

When slip exists in a tire due to acceleration or turning, forces exist between the tire/road interface. Under pure-slip conditions, the longitudinal force, lateral force, or self-aligning moment are caused by the deformation of tire treads. A simplified explanation of the forces and moment generation mechanism is shown in Figure 2.7, where the brushes are deformed by the longitudinal velocity difference (longitudinal slip) or the angle difference between tire heading direction and moving direction (lateral slip).

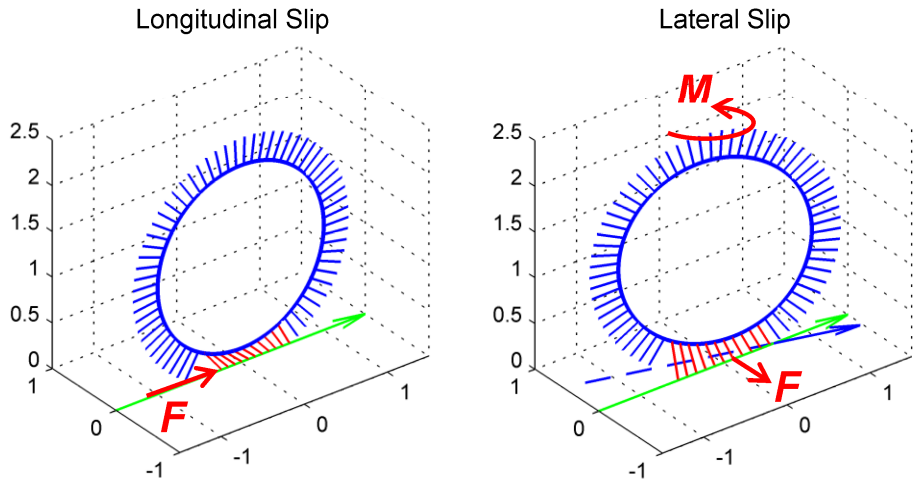

Figure 2.7 Forces and moment generation mechanism in the Brush model

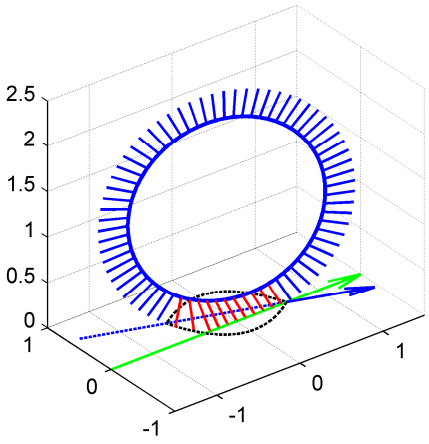

Figure 2.8 Brush deformation when the friction limit is applied to the lateral slip case

Once the tip of a brush contacts the ground, it will not move until it is raised at the trailing edge if the friction force is enough to resist the stress caused by the brush deformation. However, if the stress of a brush exceeds the friction force limit, then the

brush will slide. The distribution of friction force limit is parabolic because friction force limit is determined by the friction coefficient and the vertical stresses. Therefore, brushes start to slide once their deformation reaches the deformation limit as shown in Figure 2.8 where the black dashed line represents the deformation limit due to the friction limit.

The generated forces or moment can be computed by integrating the stress of all brushes in the contact patch. The detailed computation methods are provided by Pacejka [5]. In a pure longitudinal slip case, the tire longitudinal force, f_x, can be represented as follows:

$$f_x(\kappa,\ \mu) = \begin{cases} 3\mu F_z \theta_x \sigma_x \left\{ 1 - \left|\theta_x \sigma_x\right| + \frac{1}{3}\left|\theta_x \sigma_x\right|^2 \right\} & for \quad |\kappa| \le |\kappa_{sl}| \\ \mu F_z \cdot sign(\kappa) & for \quad |\kappa| > |\kappa_{sl}| \end{cases}, \qquad (2.11)$$

where

$\theta_x = 2c_p l^2 / (3\mu F_z)$,
$\sigma_x = \kappa / (\kappa + 1)$,
$\kappa_{sl} = 1 / (\theta_x - 1)$,
$\kappa = \dfrac{r_e \omega - v_x}{v_x}$: *tire slip ratio*,
r_e : *effective rolling radius of the tire*,
ω : *wheel rotational speed*,
v_x : *vehicle longitudinal speed*,
μ : *road-tire frictional coefficient*,
l : *half of the tire contact length*,
F_z : *tire normal force*,
c_p : *stiffness coefficient of tread in unit length.*

In a pure lateral slip case, the tire lateral force, f_y, and tire aligning moment, τ_a, can be represented as follows:

$$f_y(\alpha,\ \mu) = \begin{cases} -3\mu F_z \theta_y \sigma_y \left\{ 1 - \left|\theta_y \sigma_y\right| + \frac{1}{3}\left|\theta_y \sigma_y\right|^2 \right\} & for \quad |\alpha| \le |\alpha_{sl}| \\ -\mu F_z \cdot sign(\alpha) & for \quad |\alpha| > |\alpha_{sl}| \end{cases}, \qquad (2.12)$$

$$\tau_a(\alpha,\ \mu) = \begin{cases} \mu F_z l \theta_y \sigma_y \left(1 - \left|\theta_y \sigma_y\right|\right)^3 & for \quad |\alpha| \le |\alpha_{sl}| \\ 0 & for \quad |\alpha| \le |\alpha_{sl}| \end{cases}, \qquad (2.13)$$

where

$\theta_y = 2c_p l^2 / (3\mu F_z)$,

$\sigma_y = \tan(\alpha)$,

$\alpha_{sl} = \tan^{-1}(1/\theta_y)$: the slip angle when tire start complete sliding,

α: tire slip angle.

The force and moment curves are plotted for several friction coefficients in Figure 2.9 below. Initially, the longitudinal and lateral forces increase linearly with slip and eventually the forces reach saturation values due to the limited friction potential. The tire aligning moment also shows a linear relationship to tire slip angle when the slip angle is small. It then reaches a peak and goes down to zero as the tire slip angle increases, because the pneumatic trail decreases, whereas tire lateral force increases as the tire slip angle increases.

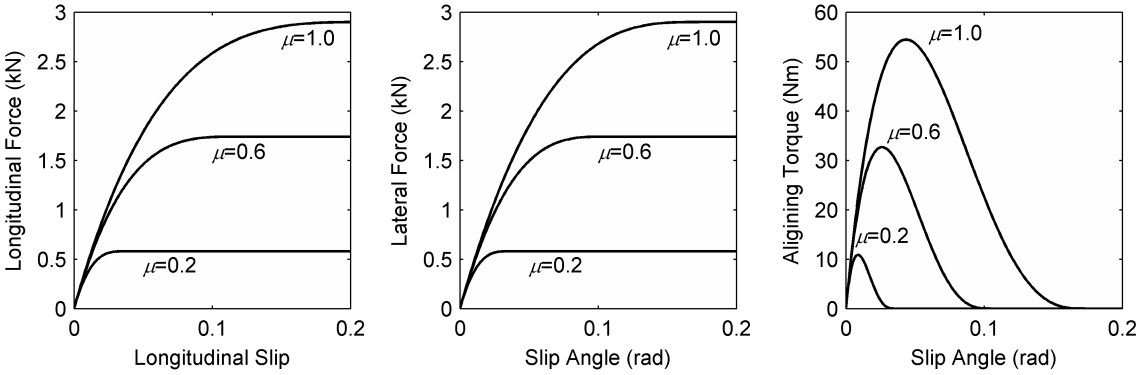

Figure 2.9 Forces and moment curves of the Brush model

The force and moment equations in combined slip cases are similar to the equations for pure slip cases. If both lateral slip and longitudinal slip exist, the treads are deformed in the direction determined by the magnitudes of both slips. The Brush model for the combined slip case is shown in the following equation:

$$F(\alpha,\ \kappa,\mu)=\begin{cases}\mu F_z(1-\rho^3) & for\ \ |\sigma|\le|\sigma_{sl}|\\ \mu F_z sgn(\alpha) & for\ \ |\sigma|>|\sigma_{sl}|\end{cases},$$
$$F_x=F\frac{\sigma_x}{\sigma},\ \ F_y=F\frac{\sigma_y}{\sigma},\ \ M_z=-t(\sigma)\cdot F_y, \tag{2.14}$$

where

$$\rho=1-\theta\sigma,$$
$$\theta=2c_p l^2/(3\mu F_z),$$
$$\sigma=\sqrt{\sigma_x^2+\sigma_y^2},$$
$$\sigma_x=\kappa/(\kappa+1),$$
$$\sigma_y=(\tan\alpha)/(\kappa+1),$$
$$\sigma_{sl}=1/\theta,$$
$$t(\sigma)=\frac{l\left(1-|\theta\sigma|\right)^3}{3-3|\theta\sigma|+|\theta\sigma|^2}.$$

These simple equations and the plot in Figure 2.9 illustrate the basic concept of the tire model estimation methods as well as their limitations. When we measure a friction coefficient between two surfaces in contact with each other, a relative tendency for movement of the two contacting surfaces needs to exist. Then, the friction coefficient is easily obtained by measuring the horizontal force (F_h) and the vertical (F_z) force during the movement and using the simple relation, $F_z=\mu F_z$. This simple method can be applied to vehicle motion. If we measure acceleration when the vehicle is completely sliding, then we can calculate the friction coefficient between the tire and the road. However, this approach is valid only when the vehicle is in excessive acceleration that might lead the vehicle to be unstable. Fortunately, we can estimate the friction coefficient even when the vehicle is not sliding because the tire is not a rigid body. In fact, tire lateral force and aligning moment gradually build up as the treads deform. This tendency of tire force and moment to build up (gradient) is different under different friction conditions. Using this phenomenon, we can differentiate the friction coefficient from the tire force and moment measurements.

An examination of Figure 2.9 shows that the curves are close to each other when the slip angle is small and that the curves are approximately linear functions of the slip

angle. Therefore, it is hard to differentiate the friction coefficient, but easy to differentiate the slip. This means that the estimation of slip angle is much easier than the estimation of the friction coefficient when the slip angle is small. On the contrary, when the slip angle is larger than the saturation point, we can differentiate the friction coefficient, but not the slip angle. This observation can be illustrated by examining the sensitivity of tire force/moment to slip angle and friction coefficient. The sensitivity when friction coefficient is 1.0 is shown in Figure 2.10. Tire force/moment sensitivities to slip angle ($\partial F_y/\partial\alpha$ and $\partial\tau_y/\partial\alpha$) are zero when the slip angle is larger than 0.2, and tire force/moment sensitivity to friction coefficient ($\partial F_y/\partial\mu$ and $\partial\tau_y/\partial\mu$) are zero when the slip angle is 0. This is why we need sufficient excitation (large slip angle) to estimate the friction coefficient.

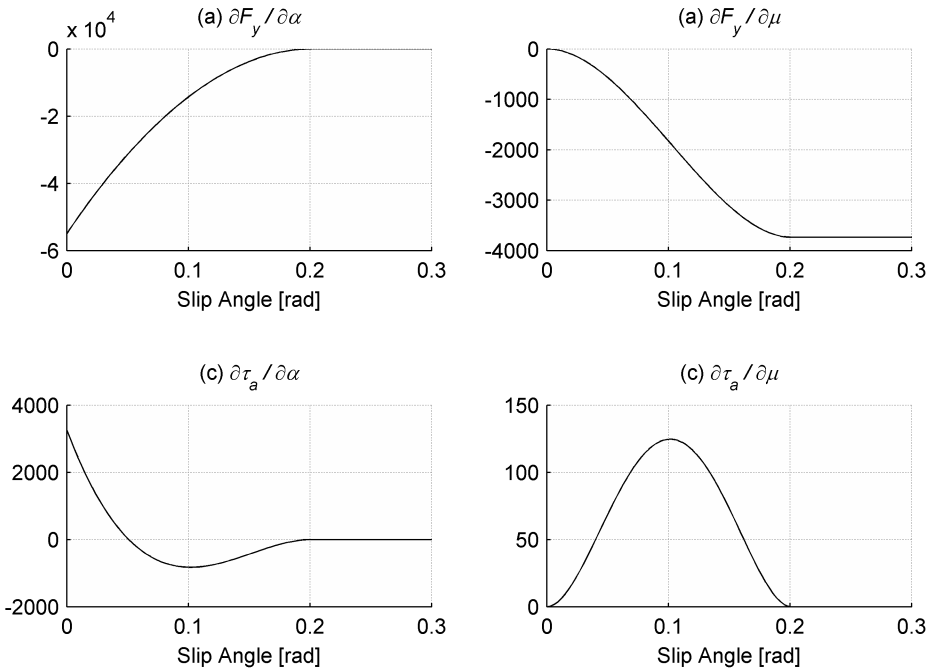

Figure 2.10 Tire force/moment sensitivity with respect to slip angle and friction coefficient

2.4 Steering System Model

Although the tire aligning moment is typically not measured in production vehicles, electrically powered steering systems provide signals, fortunately, enabling us to estimate the aligning moment of front tires. The aligning moment of front tires are

dynamically balanced by the sum of the driver's steering moment, the assist-motor's moment, and the frictional moment of the steering system. These moments and related signals are measured through the power steering assist system. Therefore, the aligning moment of front tires can be estimated using steering system dynamics and the measured signals.

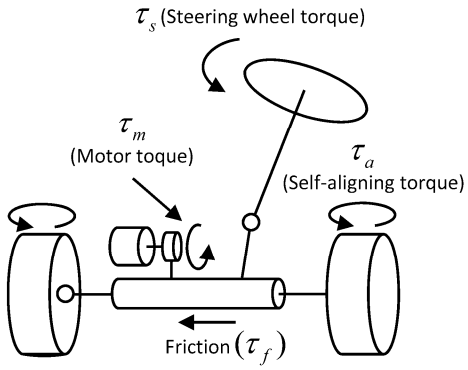

Figure 2.11 Steering system dynamics

The steering system shown in Figure 2.11 is described by the following differential equation:

$$J_{eff}\ddot{\delta} + b_{eff}\dot{\delta} + k\delta = \tau_a + \tau_s + \tau_m - \tau_f, \tag{2.15}$$

where J_{eff} is the effective moment of inertia, b_{eff} is the effective damping of the steering system with respect to the road wheels, and k is the jack up moment coefficient.[1] τ_a, τ_s, τ_m, and τ_f, represent the self-aligning moment, steering wheel torque, motor torque, and friction torque with respect to the road wheel, respectively. We can measure τ_s with a torque sensor installed on the steering column and can predetermine τ_f from a Coulomb friction model. The motor torque, τ_m, is expressed as the following equation:

$$\tau_m = K_m i_{eff}, \tag{2.16}$$

where K_m is the motor constant and i_{eff} is the effective motor current considering the gear ratio and the motor efficiency.

[1] The jack up moment is another source of self-aligning moment caused by the tendency of the lifted vehicle body to return to the lower position when the steering wheel is steered.

2.4.1 Tire Self-Aligning Moment Observer

The tire self-aligning moment can be obtained by using a disturbance observer. Equation (2.15) can be expressed as a state space form as shown in (2.18) if we assume that the self-aligning moment is slowly changing [26]. The states of the system are the steering angle, the steering angle speed, and the tire aligning moment, and the measurement is the steering wheel angle. The inputs include effective motor current (i_{eff}) and the effective torque input ($\tau_s - \tau_f$). The slowly changing self-aligning moment can be assumed as follows:

$$\dot{\tau}_a = 0 \tag{2.17}$$

and an augmented linear system model is

$$\begin{aligned} \dot{x} &= Ax + Bu, \\ y &= Cx, \end{aligned} \tag{2.18}$$

where,

$$x = \left[\delta,\ \dot{\delta},\ \tau_a\right]^T,\quad u = \left[i_{eff},\ \tau_s - \tau_f\right]^T,$$

$$A = \begin{bmatrix} 0 & 1 & 0 \\ 0 & -\frac{b_{eff}}{J_{eff}} & \frac{1}{J_{eff}} \\ 0 & 0 & 0 \end{bmatrix},\ B = \begin{bmatrix} 0 & 0 \\ \frac{K_m}{J_{eff}} & \frac{1}{J_{eff}} \\ 0 & 0 \end{bmatrix},\ C = \begin{bmatrix} 1 & 0 & 0 \end{bmatrix}.$$

We constructed a Luenberger observer to estimate the tire self-aligning moment and the steering wheel speed. By selecting an appropriate observer gain L, we aim to ensure asymptotic convergence of the estimation error.

$$\begin{aligned} \dot{\hat{x}} &= (A - LC)\hat{x} + Bu + Ly, \\ \hat{\tau}_a &= \begin{bmatrix} 0 & 0 & 1 \end{bmatrix}\hat{x}. \end{aligned} \tag{2.19}$$

Figure 2.12 shows an example of the estimation of self-aligning moment signals, where measurement noises are not included. If these noises are a matter of concern, optimal filter theories [33] can be used to design the gain L for the observer of a linear time invariant system.

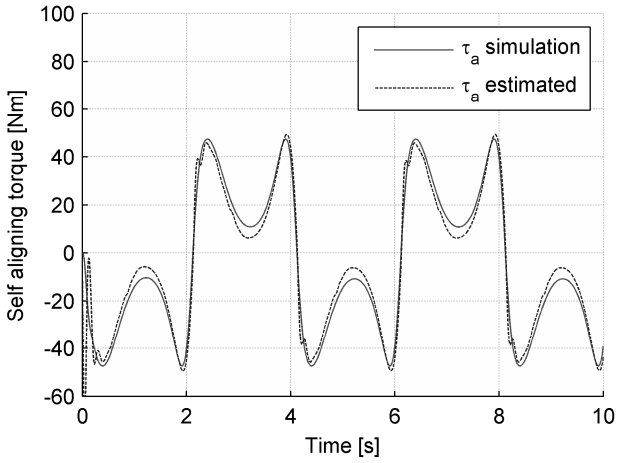

Figure 2.12 Performance evaluation of the self-aligning moment observer. "τ_a simulation" comes from the vehicle model because this is a simulation evaluation. The data was obtained from vehicle dynamics software, Carsim.

The system parameters can be obtained from design specification of the steering system or experimental results. In our case, the parameters are identified through experiments and the identification process will be further discussed in CHAPTER 6.

CHAPTER 3
LATERAL DYNAMICS BASED ESTIMATION

3.1 Estimation Algorithm for Large Lateral Excitation

Road friction affects not only the maximum tire force at very large slip, but also the tire force at small slip. The maximum tire force and maximum self-aligning moment were found to be directly proportional to the friction coefficient. In this chapter, we aim to explore the fundamental relations between road friction and tire force and aligning moment generation in order to estimate the friction coefficient.

3.1.1 Maximum Self-Aligning Moment Detection

When the tire-road friction coefficient changes, the self-aligning moment characteristic, as well as its peak value varies; this variation can be used as the basis for friction estimation. The relationship between the friction coefficient (μ) and the peak value is found from the extremum of the aligning moment curve. Assuming the Brush tire model is a good representation of tire aligning moment behavior, the maximum value of the aligning moment can be found through the following equations

$$\frac{\partial \tau_a}{\partial \sigma_y} = \mu F_z l \theta_y (1 - 4\theta_y \sigma_y)(1 - \theta_y \sigma_y)^2 = 0, \tag{3.1}$$

where τ_a is in (2.13). Equation (3.1) is satisfied when σ_y =1/(4θ_y) or σ_y =1/ θ_y. The aligning moment curve reaches its peak value in the first case and returns to the zero in the second case. At the true extremum point, we have two equations:

$$\begin{aligned} &\sigma_{y,peak} = \tan(\alpha_{peak}) = 1/(4\theta_y) = \frac{3\mu F_z}{8 c_p l^2}, \\ &\Rightarrow \mu = \frac{\tan(\alpha_{peak}) \cdot 8 c_p l^2}{3 F_z}, \end{aligned} \tag{3.2}$$

$$\tau_{a,peak} = \tau_a\left(\sigma_y = \frac{1}{4\theta_y}\right) = \frac{27}{256}\mu F_z l,$$
$$\Rightarrow \mu = \frac{256}{27}\frac{\tau_{a,peak}}{F_z l}. \tag{3.3}$$

These two equations show that if we know either the tire slip angle or the aligning moment when the self-aligning moment reaches its peak value, then we can calculate the friction coefficient. In addition, the two equations also indicate that the friction coefficient is linearly related to the peak slip angle, and the peak aligning moment. Equation (3.3) is typically more useful than (3.2) because tire slip angle is harder to acquire.

To use (3.3) for friction estimation, we can use the maximum value of the aligning moment within a past time window. The problem with this method is that the estimation result is accurate only when (i) lateral excitation is strong enough, and (ii) the window of data observation is large—which may have the drawback of resulting in a slow response to sudden friction change. This method is still valuable, however, in that a lower bound of the friction coefficient can be calculated from the maximum aligning moment data in the window:

$$\tau_{a,\max} = \max_{\tau\in[t-t_h,t]}\left(\tau_a(\tau)\right),$$
$$\mu_{lower\ bound} = \frac{256}{27}\frac{\tau_{a,\max}}{F_z c}. \tag{3.4}$$

This direct calculation algorithm only provides an estimated lower bound of the true friction coefficient and it may be far below the true value if the excitation is small. Therefore, this algorithm is useful only when lateral excitation is large enough. An algorithm that works for less demanding excitation condition is proposed in Chapter 3.2.

3.1.2 Simulation Results

The estimation performance is evaluated in this section using the commercial software Carsim. The target vehicle is a compact sedan modeled as a multi-body-object

with 27 degrees of freedom, and the tire model used is the Magic Formula model. The vehicle and tire parameters are listed in Table 3.1 and these parameters will be used for all simulation hereafter.

Table 3.1 Vehicle and tire parameters used in the simulations

Parameter	Value	Unit	Description
m	1412	kg	Vehicle mass
I_z	1523	$kg \cdot m^2$	Moment of inertia
a	1.016	m	Distance from the front axle to the center of mass
b	1.562	m	Distance from the rear axle to the center of mass
l	0.178	m	Half of the tire contact length
c_p	7.9×10^5	N/m^2	Tread stiffness in unit length

The maximum self-aligning moment method was evaluated under several conditions. In the following simulations shown in Figure 3.1, the vehicle speed is 60 km/h and the steering input is 0.25Hz sine wave with a magnitude of 0.04 radians, equivalent to 50 degrees at the steering wheel. The tire-road friction coefficients are set at four levels: 1.0, 0.5, 0.2, and a time varying value. The estimation results, shown in Figure 3.1, demonstrate that the maximum moment method performs poorly in estimating friction coefficient and does not estimate slip angle accurately, but works well when the front tire slip angle is large enough. However, as mentioned earlier, the friction coefficient estimated by the maximum aligning moment method is a lower bound of the real friction coefficient and can be useful if used in the appropriate context. Indeed, it was confirmed that the coefficient estimated by this method is always smaller than the actual value, as shown in Figure 3.1. Even though the maximum moment method is not always accurate, it can nevertheless provide a lower limit for the friction coefficient for other estimators if tire model matches to the actual tire. In fact, some other methods considered in this paper use this underestimated friction coefficient as a lower bound.

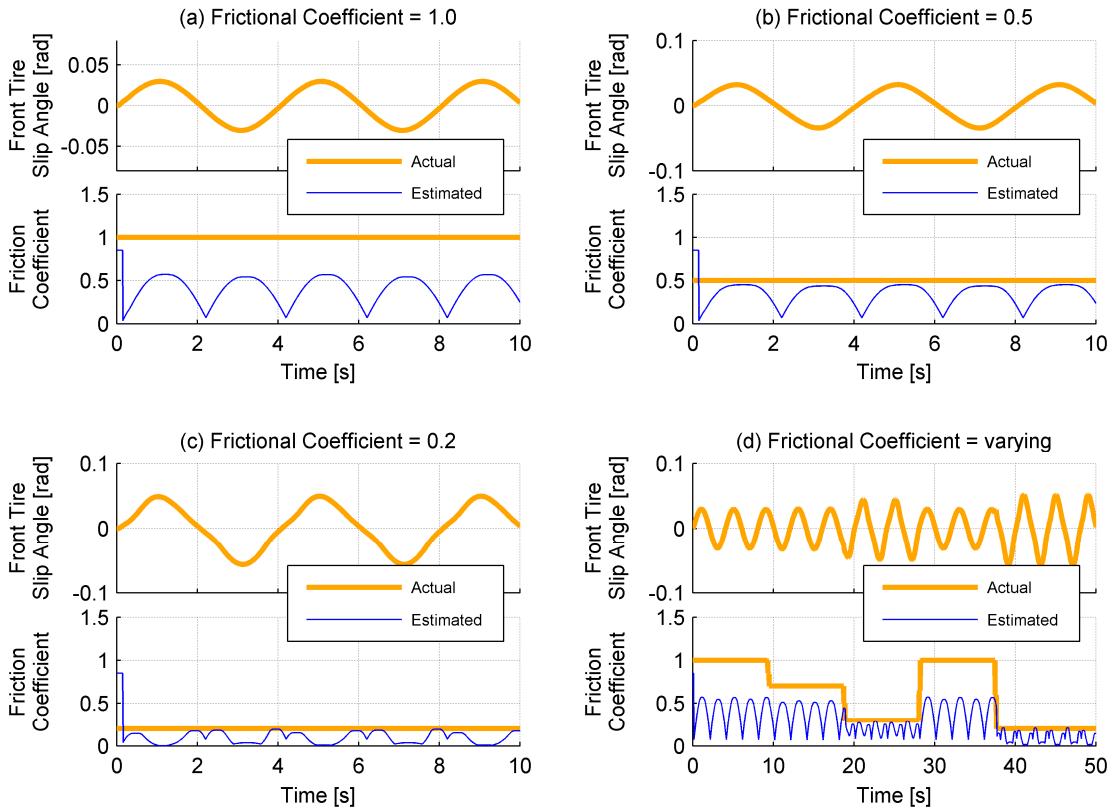

Figure 3.1 Simulation results of the maximum self-aligning moment detection method with sinusoidal steering input and v_x=60km/h

3.2 Estimation Algorithm for Medium Lateral Excitation

The maximum self-aligning moment detection method is useful only when the lateral excitation level is sufficiently large. Actually, there are two measurements (lateral acceleration and front tire aligning moment) characterized by two independent variables (slip angle and friction coefficients) affecting not only the peak value of the two measurements but also the overall distribution of the measurements. This means that we can estimate road friction (and as a side product, the slip angle) through a series of the measured signals even when at small excitations. In this chapter, parameter estimation algorithms based on a least squares process and a nonlinear observer design will be described.

3.2.1 Nonlinear Least Squares Method

3.2.1.1 Basic Equations

The least squares method is useful for solving over-determined nonlinear problems. It can also be seen as a method for the identification of parameters through determining the best fit between modeled and observed data. Hsu [25] used nonlinear least squares to identify the friction coefficient, which he identified as a parameter of the self-aligning moment equations. Tire slip angles, an important but hard-to-estimate variable, are provided from a GPS-based sideslip measurement system. In this section, we introduce a nonlinear least squares method based on lateral acceleration measured with an accelerometer and the front tires' self-aligning moment, which is obtained using the tire aligning moment observer described in the previous chapter. The sum of the lateral tire forces can be determined using measured vehicle lateral acceleration, as described in (2.3) and (2.6).

$$F_{yf} + F_{yr} = f_y(\alpha_f, \mu)\cos\delta + f_y(\alpha_r, \mu), \tag{3.5}$$

where, f_y is the tire lateral force, a function of tire slip angle and the friction coefficient when the tire normal force is estimated using the load transfer model described in (2.7). The rear tire slip angle α_r is determined by (2.2) if front tire slip angle α_f is known and u, r, δ are measured. As a result, the left side of (3.5) is determined by measurement and the right side is a function of α_f and μ. This equation relates the measurement and the two unknowns (α_f and μ). Obviously, this equation alone is not enough to estimate both unknown parameters unless we have batch data.

The tire self-aligning moment is also a function of α_f and μ, and it can be monitored by the aligning moment observer developed in Section 2.4.1. Tire normal forces can be estimated using (2.7). Therefore, we have the second relationship:

$$\tau_{a,obs} = \tau_a(\alpha_f, \mu), \tag{3.6}$$

where $\tau_{a,obs}$ is the observed tire self-aligning moment. Ultimately, we have two unknowns, α_f and μ, and two equations, (3.5) and (3.6), so that theoretically we are able

to determine two unknowns. Nevertheless, the two equations are nonlinear and thus the invertibility of these equations depends on the linearized Jacobian matrix, which may be close to singular under certain conditions. For example, it is clear that when the slip angle α_f is small, the aligning moment and lateral force are both small as well, and thus it becomes difficult to estimate the road friction. The larger the value of singularity, the less invertible the matrix becomes.

$$\begin{bmatrix} F_{yf} + F_{yr} \\ \tau_{a,obs} \end{bmatrix} = J \begin{bmatrix} \alpha_f \\ \mu \end{bmatrix}, \tag{3.7}$$

where

$$J = \begin{bmatrix} \frac{\partial f_{yf}}{\partial \alpha}|_{\alpha_f,\mu} \cos\delta + \frac{\partial f_{yr}}{\partial \alpha}|_{\alpha_r,\mu} & \frac{\partial f_{yf}}{\partial \mu}|_{\alpha_f,\mu} \cos\delta + \frac{\partial f_{yr}}{\partial \mu}|_{\alpha_r,\mu} \\ \frac{\partial \tau_{a,obs}}{\partial \alpha}|_{\alpha_f,\mu} & \frac{\partial \tau_{a,obs}}{\partial \mu}|_{\alpha_f,\mu} \end{bmatrix}.$$

The singularity of a matrix J is defined as the condition number, κ, as follows:

$$\kappa(J) = \frac{\sigma_{\max}(J)}{\sigma_{\min}(J)}, \tag{3.8}$$

where $\sigma_{\max}(J)$ and $\sigma_{\min}(J)$ are the maximum and minimum singular values of J, respectively.

Figure 3.2 shows the singularity of the Jacobian matrix. The x and y axes are normalized where ±1 mean that the tire force starts to saturate. The Jacobian matrix is not always invertible: when the front tire slip angle is small, it is hard to invert and, consequently, parameter estimation may not be accurate. In this case, estimating the friction coefficient is difficult because $\partial F_y/\partial\mu$ and $\partial\tau_a/\partial\mu$ are almost zero as shown in Figure 2.10. If the front tire slip angle is very large, the normalized value is larger than 1 or smaller than −1, which makes it impossible to estimate the slip angle because $\partial F_y/\partial\alpha$ and $\partial\tau_a/\partial\alpha$ are zero, as shown in Figure 2.10. Thus, neither small tire slip angles nor large tire slip angles are desirable for estimation. Assuming the excitation level is neither too large nor too small, the nonlinear least squares method can be used to find the unknowns.

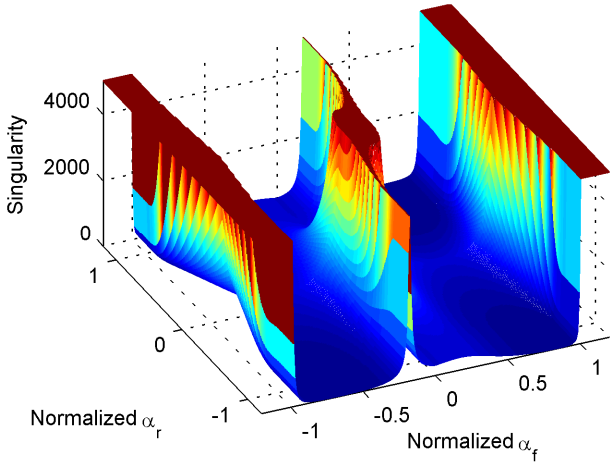

Figure 3.2 Singularity of the Jacobian matrix; The larger the value of singularity, the closer the matrix is to a singular matrix, the *x* and *y* axis are normalized and μ=1.0.

3.2.1.2 Formulation of a Nonlinear Least Squares Problem

We can solve the two nonlinear equations, (3.5) and (3.6), with a single datum. However, the result will be vulnerable to measurement noise or observer error in a_y and $\tau_{a,obs}$. In order to achieve results that are robust against noise and model uncertainties, we use the nonlinear least squares method with *n* sets of the measurement data. The formulation of the nonlinear least squares problem is

$$\hat{\vec{x}}_k = \arg\min_{\vec{x}_k} J(k, \vec{x}_k), \tag{3.9}$$

where

k=1, 2, 3, …

$$J(k,\vec{x}_k) = \left|\vec{F}_y(k) - \hat{\vec{F}}_y(k,\vec{x}_k)\right|^2 + \gamma\left|\vec{\tau}_a(k) - \hat{\vec{\tau}}_a(k,\vec{x}_k)\right|^2,$$

$$\gamma : weighting \quad factor,$$

$$\vec{x}_k = \left[\alpha_{f,k-n+1},\ \alpha_{f,k-n+2},\cdots,\alpha_{f,\mathrm{k}},\ \mu_k\right]^T,$$

$$\vec{F}_y(k) = \left[ma_{y,k-n+1},\ ma_{y,k-n+2},\cdots,ma_{y,k}\right]^T,$$

$$\hat{\vec{F}}_y(k,\vec{x}_k) = \left[\hat{F}_y(k-n+1,\vec{x}_k),\cdots,\hat{F}_y(k,\vec{x}_k)\right]^T,$$

$$\hat{F}_y(j,\vec{x}_k) = f_{yf}(\alpha_{f,j},\mu_k)\cos\delta_j + f_{yr}(\alpha_{r,j},\mu_k),$$

$$\hat{\vec{\tau}}_a(k) = \left[\tau_{a,k-n+1},\ \tau_{a,k-n+2},\cdots,\tau_{a,k}\right]^T,$$

$$\hat{\vec{\tau}}_a(j,\vec{x}_k)=\left[\hat{\tau}_a(\alpha_{f,k-n+1},\,\mu_k),\cdots,\,\hat{\tau}_a(\alpha_{f,k},\,\mu_k)\right]^T,$$

$$\alpha_{r,j}=\alpha_{f,j}-\frac{Lr_j}{v_{xj}}+\delta_j,$$

$(\,)_j$: an estimated or measured property at time step *j*.

In the above least squares problem, we assume the friction coefficient is constant throughout the *n*-step horizon, whereas the slip angles are assumed to vary with time. As a result, we have *n*+1 unknowns (*n* slip angles and one friction coefficient) and 2*n* equations (*n* force equations and *n* torque equations). These nonlinear equations are over-determined and the least-squares solution is obtained numerically.

3.2.1.3 Initial Values for the Nonlinear Least Squares Method

A nonlinear least squares method starts from an initial guess and searches for better results iteratively. Therefore, the quality of the solution depends on the initial guess. The choice of an appropriate initial guess of α_f and μ at each time step is thus important. The solution obtained at the previous time step is generally a good initial guess. A better initial guess can reduce iteration time and improve convergence. Furthermore, if there are several local minima in the cost function, offering a plausible initial value may be helpful. The most plausible candidates for the parameters of a subsequent time step can be projected from the parameters of the preceding time step based on their dynamics. We can obtain the dynamics of α_f from (2.1) and (2.2) where all model parameters are assumed to be constant.

$$\begin{aligned}\dot{\alpha}_f&=\left(\frac{1}{mv_x}+\frac{a^2}{I_z v_x}\right)F_{yf}+\left(\frac{1}{mv_x}-\frac{ab}{I_z v_x}\right)F_{yr}-r-\dot{\delta},\\ \dot{\mu}&=0.\end{aligned}\tag{3.10}$$

where $F_{yf}=f_{yf}(\alpha_f,\mu)\cos(\delta)$ is the lateral force at the front axle and $F_{yr}=f_{yr}(\alpha_r,\mu)$ is the lateral force at the rear axle. The plausible initial value can be set as follows:

$$\begin{aligned}\alpha_{f0}(t+\Delta t)&=\alpha_f^{\,*}(t)+\Delta t\cdot\dot{\alpha}_f(t),\\ \mu_0(t+\Delta t)&=\mu^*(t).\end{aligned}\tag{3.11}$$

where α_{f0} and μ_0 are the initial values at $t+\Delta t$, α^*_0 and μ^*_0 are the optimal values obtained at t, and $\dot{\alpha}_f(t)$ is the slip angle dynamics at t as presented in (3.10).

3.2.1.4 Simulation Results

The estimation error and the convergence of the nonlinear least square method are evaluated by also using Carsim. The nonlinear least squares method is tested under several conditions. In the following simulations, the vehicle speed is 60 km/h and the steering input is 0.25Hz sine wave with a magnitude of 0.04 radians, equivalent to 50 degrees at the steering wheel. The tire-road friction coefficients are set at four levels: 1.0, 0.5, 0.2, and a time varying value. The estimation results are shown in Figure 3.3.

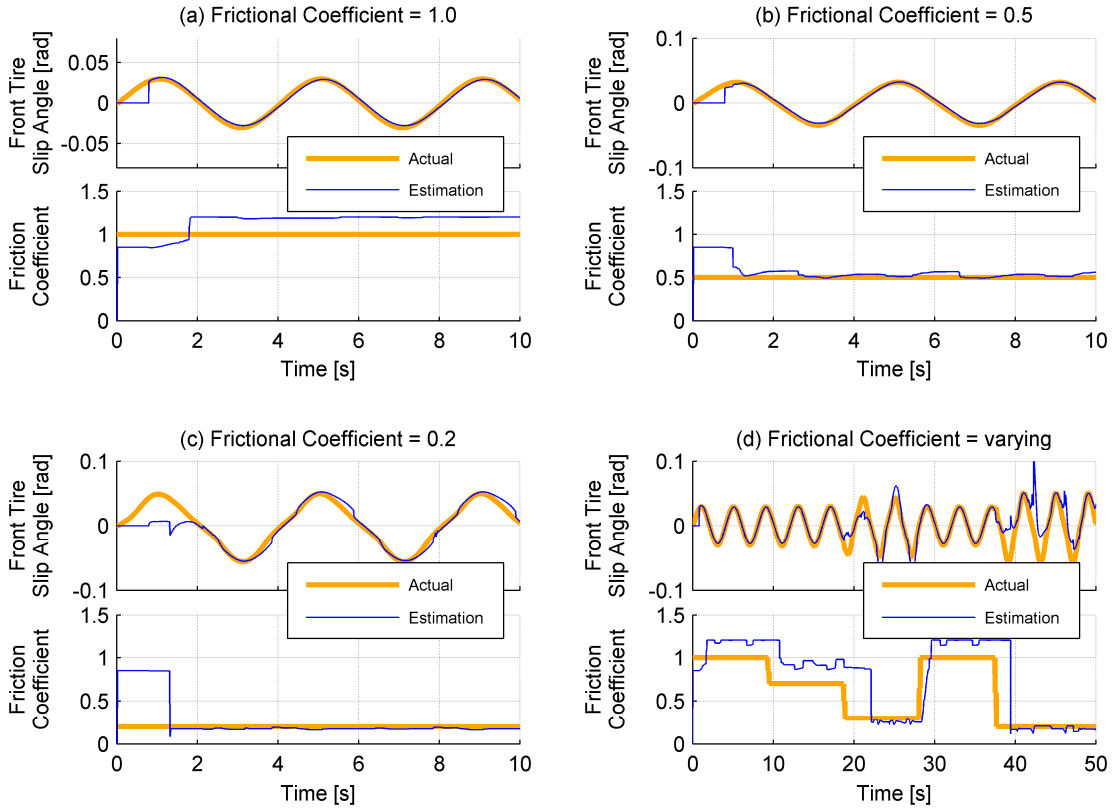

Figure 3.3 Simulation results of the nonlinear least squares method with sinusoidal steering input and v_x=60km/h

The nonlinear least squares method achieves acceptable estimation results when the real friction coefficient is low (0.5 and 0.2). However, when μ =1.0, the friction coefficient is overestimated. The Brush tire model used in the estimation algorithm is

different from the Magic Formula tire model used in Carsim, as shown in Figure 3.4. These two models show similar behaviors when the vertical tire force is 3000N; however, as the vertical force increases, the behaviors, especially aligning moment curves, deviate from each other. In addition, our simple tire and vehicle models do not capture the complex behavior, such as suspension, roll and pitch motions, tire normal force variation, and camber. In the Brush tire model, the normalized peak value of the lateral force is constant as the vertical tire force changes, whereas, in the Magic Formula tire model, the normalized peak values of lateral forces vary with the tire normal forces, as shown in Figure 3.5. The model error becomes apparent as the friction coefficient increases, which is a major reason for overestimation at high friction surfaces. Because of these inevitable model differences, the estimation is never precise. For example, if the estimated coefficient is 1.0, the real coefficient may be between 0.9 and 1.1. Therefore, the model errors and the estimation errors should be considered when the estimated result is used for control purposes.

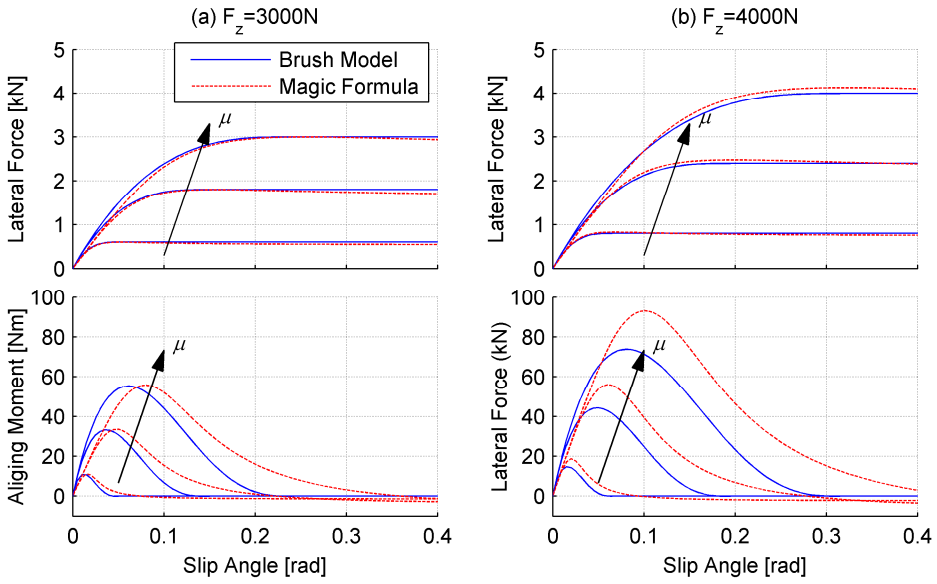

Figure 3.4 Comparison between the Brush model and the Magic Formula model

When the friction coefficient is time-varying, the nonlinear least squares method presents a slow response. The assumption of a constant friction coefficient and size of batch window (0.8 second) are the main reasons for this slow response. In addition, the fact that the initial guess uses the previous identified solution also favors remaining at the

previous local minimum rather than quickly following the plant variation to the new minimum. It can be seen that the estimated values of both slip angle and friction coefficient are incorrect at 20~21 second interval. The slip angle is underestimated, and the friction coefficient overestimated, because the initial values for the nonlinear least squares algorithm differ greatly from the true values. Abrupt changes of road surface condition, for example, μ=0.7 to 0.2, result in a large difference between the actual friction coefficient and the initial value. This large difference requires a long computation time and sometimes this process fails to reach to the true optimal values. The estimation algorithm limits the computation time to satisfy the real time requirement; therefore, when a large initial error exists, it may take several iteration cycles before convergence to the true optimal value takes place.

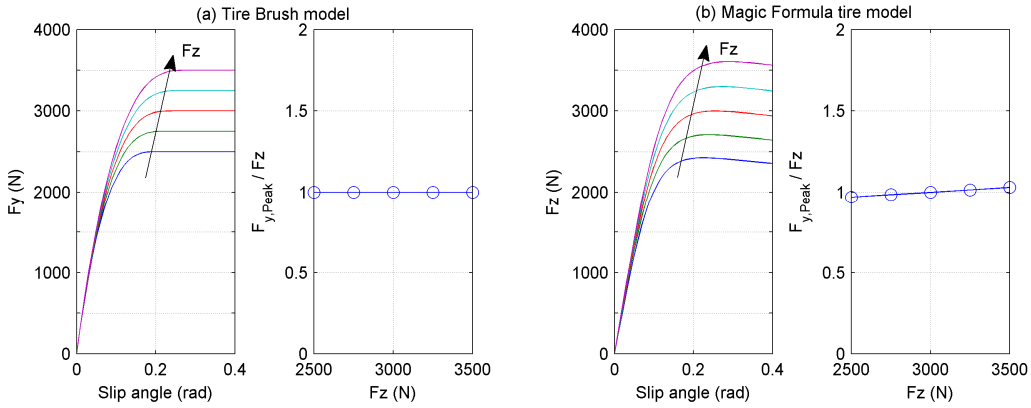

Figure 3.5 Lateral force characteristics of the Brush model and the Magic Formula model

The second simulation is designed to verify the performance of our algorithms at different vehicle speeds. All other simulation conditions remain the same. The actual friction coefficient is 0.5 and the steering inputs are 50 degree-magnitude-sinusoidal. The vehicle speeds are set to be constant, at 20 km/h, 40 km/h, 60 km/h, and 80 km/h. The four simulation results are shown in Figure 3.6. Estimation results with respect to speed, such as 20km/h and 40km/h, show large estimation errors or slow convergence because of low excitations. A necessary condition for good estimation results is large slip angle, as was explained in Chapter 2.2. The tire force and moment curves in Figure 2.9 show that differentiating the tire force and moment curves under different friction coefficients is difficult when the slip angle is small. Another reason for the poor

estimation in low speed cases is the small magnitudes of measurement signals. A small signal to noise ratio negatively affects the estimation accuracy which will be an important factor when the algorithm is implemented on a vehicle. Therefore, adequately large slip angles are required for stable and accurate estimation.

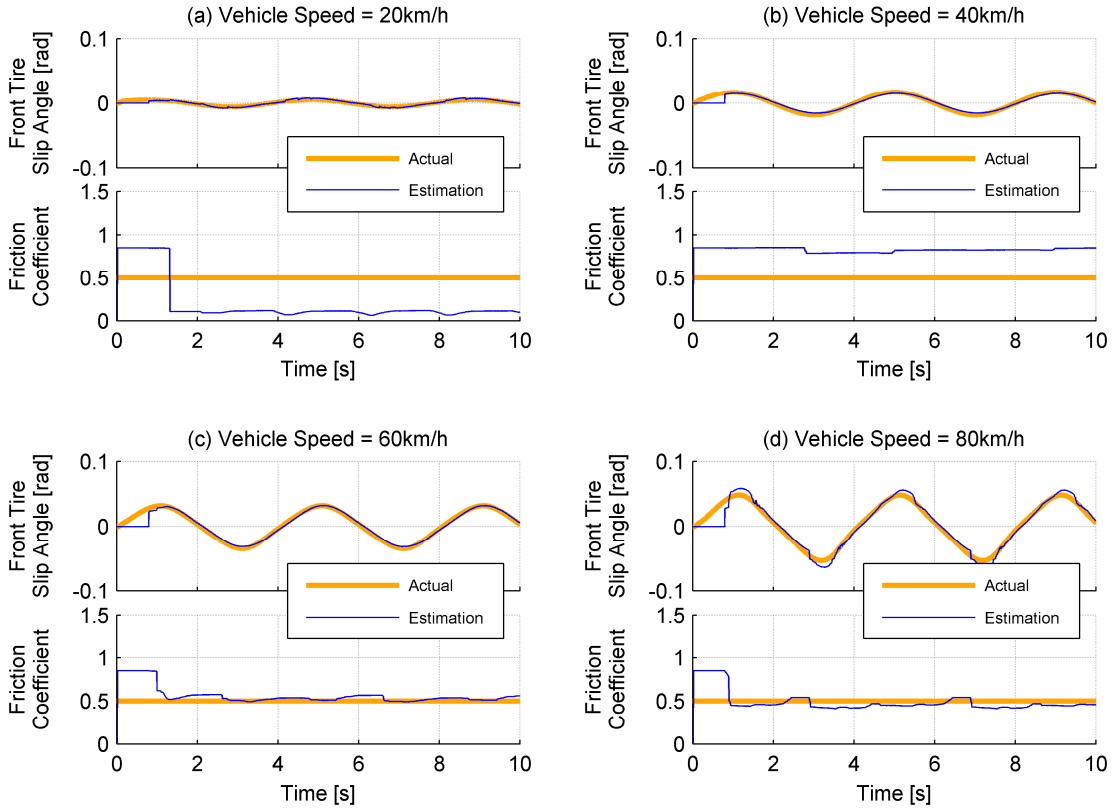

Figure 3.6 Simulation results of the nonlinear least squares method with different vehicle speeds and μ=0.5

The third simulation is designed to study the effects of different steering magnitudes. The vehicle speed is kept at a constant speed, 60 km/h, the friction coefficient is 0.5, and the steering inputs are sinusoidal inputs having the same frequency but four different magnitudes. The four simulation results are plotted in Figure 3.7, showing that small steering input does not guarantee the convergence. Of course, if the vehicle speed or road conditions are different, the required steering excitation for convergence may also be different. This discussion is related to the concept of persistent excitation and to the sensitivity of the tire force/moment with respect to the tire slip angle.

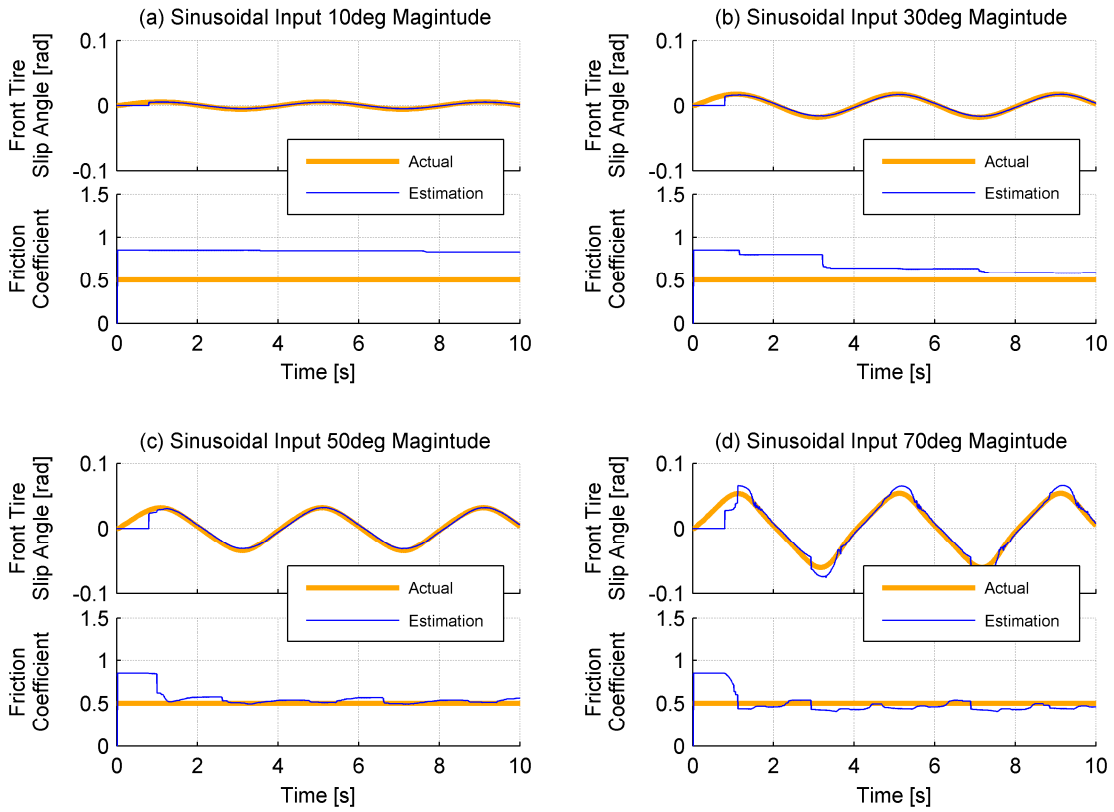

Figure 3.7 Simulation results of the nonlinear least squares method with various magnitudes of steering input, μ=0.5, and v_x=60km/h

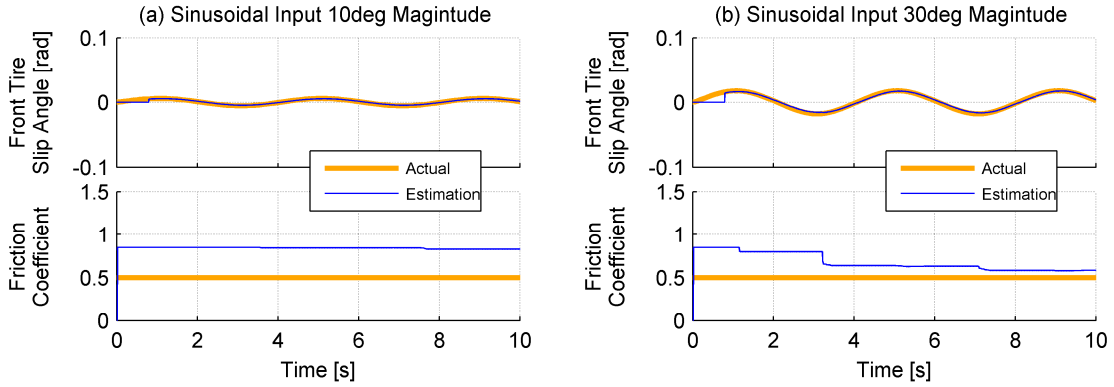

Figure 3.8 Simulation results of the nonlinear least squares method with step steering input and v_x=60km/h

The steering magnitude as well as the richness of the steering content will affect performance. Therefore, the fourth set of simulations is designed to verify the effect of steering "content". The vehicle speed is set to a constant speed, 60 km/h, and the friction coefficient is 0.5. The steering inputs are set, first as a step input and then, at a ramp

steering input up to roughly 100 degrees. Figure 3.8 shows the simulation results with the step inputs and Figure 3.9 shows the result with the ramp input. Before the steering inputs are adequately large, the estimated results have significant errors. Once the steering inputs become large enough, the estimated friction coefficient quickly converges to the true values. However, when the steering input is excessively large, the slip angle estimation starts to diverge. This phenomenon can be illustrated by using the Brush tire model behavior shown in Chapter 2.2. The observability for slip angle is lost after force saturation.

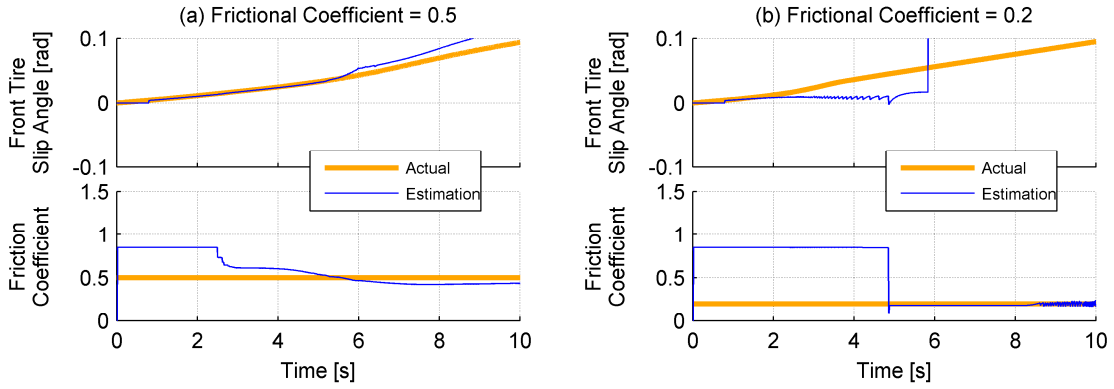

Figure 3.9 Simulation results of the nonlinear least squares method with ramp steering input and v_x=60km/h

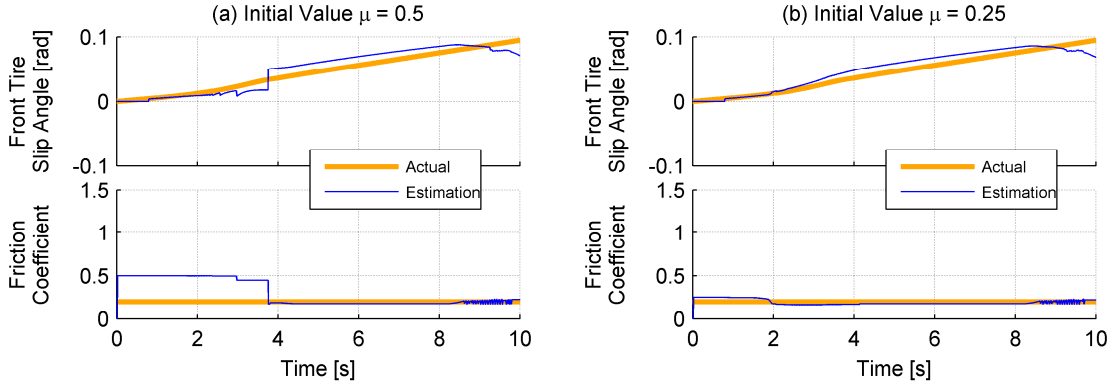

Figure 3.10 Simulation results of the nonlinear least squares method with different initial values

The last set of simulations is designed to study the effect of initial conditions. The best possible selection of the initial value is important in order to get the optimal solution in nonlinear optimization problems with multiple local minima. In the simulations, when

the initial friction coefficient estimation error is 0.3 (left plot of Figure 3.10) it takes 4 seconds to converge, and, only 2 seconds when the initial error is 0.05 (right plot of Figure 3.10). The combination of a large initial error and small excitation results in slow convergence.

From the simulation results above, we conclude that large slip angle is, in general, beneficial for friction estimation. However, when the slip angle is too large, we will have poor slip angle estimation, in which case the peak moment method should be used. In addition, a small initial error is required to achieve fast convergence and accurate estimation. The quantitative criteria for vehicle speed, steering input size, and steering input richness were not identified, but such effort may not be particularly useful because of the nonlinear and numerical nature of the algorithm. Nevertheless, these simulations provide useful qualitative guidelines for the performance of the proposed algorithm.

3.2.2 Dynamic Approach

The algebraic approach presented in the previous chapter is based on input/output signals. The algebraic approach used knowledge related to the tire force/moment generation mechanisms but did not use the dynamic model. Using a vehicle model is beneficial because the dynamics are slow such as few Hz and thus less vulnerable to measurement noises. Dakhlallah [34] and Baffet [35] used an extended Kalman filter based on a vehicle/tire model to estimate vehicle states and tire forces. Kalman filters generally perform well if a reasonably accurate model is available and the system can be approximated by a linear model. However, if the error dynamics are not well approximated by linearized transformations, the performance of an extended Kalman filter is degraded or, worse yet, the estimate may diverge. Hsu [26] proposed a nonlinear observer with a gain based on the Jacobian matrix of the system, but did not address the stability issue. In this chapter, we propose a nonlinear observer for a certain class of systems and a design methodology for the observer. The convergence and robustness of the observer will be analyzed using the Lyapunov theorem.

3.2.2.1 Design Synthesis of Nonlinear Observer

We first start with a general problem formulation. Consider the following nonlinear dynamic system and nonlinear measurement:

$$\begin{aligned} \dot{x} &= f(x,u,\theta), \\ y &= h(x,u,\theta), \end{aligned} \tag{3.12}$$

where x is the state of the system, y is the measurement, u is the control input, and θ is a vector of constant parameters to be estimated. When we assume that we have access to x, a possible parameter estimation algorithm is

$$\dot{\hat{\theta}} = \left(\frac{\partial h}{\partial \theta}(x,u,\hat{\theta}) \right)^T \left(h(x,u,\theta) - h(x,u,\hat{\theta}) \right). \tag{3.13}$$

If we assume that h is continuous, differentiable, and satisfies the following condition:

$$\theta \approx \hat{\theta} \Rightarrow \left. \frac{\partial h}{\partial \theta} \right|_{\theta} \approx \left. \frac{\partial h}{\partial \theta} \right|_{\hat{\theta}}, \ for\ \forall x, \forall u. \tag{3.14}$$

Then (3.13) becomes

$$\dot{\hat{\theta}} \approx \left(\frac{\partial h}{\partial \theta} \right)^T \frac{\partial h}{\partial \theta}(\theta - \hat{\theta}), \tag{3.15}$$

and the error dynamics of the parameter estimation are

$$\dot{\tilde{\theta}} \approx -K\tilde{\theta}, \quad K = \left(\frac{\partial h}{\partial \theta} \right)^T \frac{\partial h}{\partial \theta} \geq 0, \tag{3.16}$$

where $\tilde{\theta} = \theta - \hat{\theta}$. If the matrix K is strictly positive i.e., K is not singular at all times (persistent excitation) then, $\tilde{\theta} \to 0$ or $\hat{\theta} \to \theta$ as $t \to \infty$.

This result means that if we have access to system states, the measurement equations are continuous and differentiable, and excitation is persistent, then the parameter estimated by (3.13) converges to the actual value. This algorithm may be applied to the estimation of the friction coefficient using the measurement equations (3.5) and (3.6). However, the tire slip angle α_f, a state of the system, is not usually accessible, and we therefore need an algorithm to estimate parameters and states concurrently.

If the states of the system are not directly measureable, the algorithm proposed in the previous section is not applicable. In such situations, the following parameter and state estimation algorithm [36] for the system shown in (3.12) can be applied:

$$\begin{aligned} \dot{\hat{x}} &= f(\hat{x},u,\hat{\theta}) + L_1(\hat{x},u,\hat{\theta})\big(y-\hat{y}\big), \\ \dot{\hat{\theta}} &= L_2(\hat{x},u,\hat{\theta})\big(y-\hat{y}\big), \end{aligned} \tag{3.17}$$

where $\hat{y} = h(\hat{x},u,\hat{\theta})$. If both the state and parameter are scalar and the vector y consists of two measurements, the following augmented form of the system and estimator can be obtained

$$\begin{aligned} \dot{z} &= F(z,u), \\ \dot{\hat{z}} &= F(\hat{z},u) + L(\hat{z},u)\big(H(z,u) - H(\hat{z},u)\big), \end{aligned} \tag{3.18}$$

where

$$\hat{z} = [\hat{x},\ \hat{\theta}]^T,$$

$$F(\hat{z},u) = \begin{bmatrix} f(\hat{x},\ u,\hat{\theta}) \\ 0 \end{bmatrix},$$

$$L(\hat{z},\ u) = \begin{bmatrix} L_1(\hat{x},\ u,\hat{\theta}) \\ L_2(\hat{x},\ u,\hat{\theta}) \end{bmatrix},$$

$$H(z,\ u) = h(x,\ u,\theta) = \begin{bmatrix} h_1(x,\ u,\theta) \\ h_2(x,\ u,\theta) \end{bmatrix},$$

$$H(\hat{z},\ u) = h(\hat{x},u,\hat{\theta}) = \begin{bmatrix} h_1(\hat{x},\ u,\hat{\theta}) \\ h_2(\hat{x},\ u,\hat{\theta}) \end{bmatrix}.$$

This estimator has the structure of a general Luenberger observer with a state dependent observer gain matrix. Raghavan [37] suggested design methodologies for this type of observers for certain classes of nonlinear systems. However, the condition he suggested is very conservative, and requires the output function h to be linear and the nonlinearity of the system is globally Lipschitz, which are not the case in our system.

Therefore, the methods in [37] cannot be used. We will present a design methodology that is less restrictive in the following.

For the observer (3.18), the choice of the gain matrix affects stability and robustness of the observer. The error dynamics of the observer are shown in (3.19) and reorganized into two parts, a linearized term and a residual term.

$$\begin{aligned}\dot{e} &= F(z,u) - F(\hat{z},u) - L(\hat{z},u)\big(H(z,u) - H(\hat{z},u)\big) \\ &= A(z,u)e + r_1(z,e,u) - L(\hat{z},u)\big(C(z,u)e + r_2(z,e,u)\big) \\ &= \underbrace{\big(A(z,u) - L(\hat{z},u)C(z,u)\big)e}_{\textit{linear term}} + \underbrace{r_1(z,e,u) - L(\hat{z},u)r_2(z,e,u)}_{\textit{residual term}},\end{aligned} \tag{3.19}$$

where

$$\begin{aligned}&e = z - \hat{z}, \\ &A(z,u) = \frac{\partial F(z,u)}{\partial z}, \\ &C(z,u) = \frac{\partial H(z,u)}{\partial z}, \\ &r_1(z,e,u) = F(z,u) - F(\hat{z},u) - A(z,u)e, \\ &r_2(z,e,u) = H(z,u) - H(\hat{z},u) - C(z,u)e.\end{aligned}$$

Now, consider a Lyapunov candidate function, $V(z,e,u) = e^T P e$, where $P = P^T$ is a positive definite matrix. Then, we obtain $\dot{V}(z,e,u) = -e^T Q e + (r_1 - Lr_2)^T P e + e^T P (r_1 - Lr_2)$, where $Q = -[(A-LC)^T P + P(A-LC)]$. The sufficient condition for asymptotic stability of the observer is then

$$\dot{V}(z,e,u) = -e^T Q e + (r_1 - Lr_2)^T P e + e^T P (r_1 - Lr_2) < 0, \ \textit{for} \ \forall e \neq 0. \tag{3.20}$$

The local stability of the observer can be determined as follows. If $F(z, u)$ and $H(x, u)$ are continuous and differentiable in z, the lowest order of the polynomial terms containing the error e in $r_1(z, e, u) - Lr_2(z, e, u)$ is two because it is the residual part of the error dynamics (3.19), represented by a first order Taylor's series expansion. Therefore, the following holds:

(3.21)

$$\lim_{\|e\|\to 0}\frac{\|r_1(z,u,e)-Lr_2(z,u,e)\|}{\|e\|}=0.$$

Consequently,

$$\begin{aligned}\lim_{\|e\|\to 0}\dot{V}(z,e,u) &\le \lim_{\|e\|\to 0}\left(-\lambda_{\min}(Q)+2\frac{\|(r_1-Lr_2)\|}{\|e\|}\|P\|\right)\|e\|^2 \\ &= \lim_{\|e\|\to 0}\left(-\lambda_{\min}(Q)\right)\|e\|^2.\end{aligned} \tag{3.22}$$

In other words, if $F(z, u)$ and $H(z, u)$ are continuous and differentiable in z, and if L and P exist such that $Q=-[(A-LC)^TP+P(A-LC)]$ is positive definite for all z and u, then the observer with the selected observer gain L is locally stable at the equilibrium point $e=0$ for all z and u.

A sufficient condition that guarantees global stability of the error dynamics for any z and u is

$$\begin{aligned}&\exists L \ \ such\ that\ Q\ge 0,\ \lambda_{\min}(Q)\ge 2\gamma\|P\|\ for\ \forall z\ and\ \forall u,\ and\\ &W(e)=\inf_{z,u}V(z,e,u)\ is\ \ positive,\end{aligned} \tag{3.23}$$

where $\lambda_{min}(Q)$ is the minimum eigen-value of Q and γ is the Lipschitz constant of r_1-Lr_2 with respect to e. The second condition, $W(e)>0$, is for the stability of the time varying nonlinear system, because this observer is non-autonomous and depends on z and u. The proof of the first condition is

$$\begin{aligned}\dot{V}(z,e,u) &= -e^TQe+(r_1-Lr_2)^TPe+e^TP(r_1-Lr_2)\\ &\le -\lambda_{\min}(Q)\|e\|^2+2\|(r_1-Lr_2)\|\|P\|\|e\|\\ &\le -\lambda_{\min}(Q)\|e\|^2+2\gamma\|P\|\|e\|^2\\ &\le -\left(\lambda_{\min}(Q)-2\gamma\|P\|\right)\|e\|^2.\end{aligned} \tag{3.24}$$

If this condition is satisfied for all e, independent of z and u, the observer is globally (with respect to e) stable for any z and u. In other words, if satisfaction of the stability condition depends on z and u, then a stable observer is available only for a certain range of z and u. The stability condition (3.23) is very conservative and only

applies to a small set of nonlinear systems. Furthermore, this analysis does not provide any synthesis method in the selection of P and L.

There may or may not exist P and L that satisfy the stability conditions for all z and u, as illustrated in (3.23). An important requirement for such P and L is that they must result in a positive definite Q, which is a necessary condition for local stability. Therefore, choosing P and L that satisfy $Q>0$ provides a good starting point for the gain selection.

In the following, we suggest one pair of P and L, albeit clearly not the only possible choice that satisfies the required condition for local stability. If we choose P and L as follows:

$$
\begin{aligned}
&P = I = \begin{bmatrix} 1 & 0 \\ 0 & 1 \end{bmatrix}, \\
&L = \begin{bmatrix} l_1 & l_2 \\ l_3 & l_4 \end{bmatrix}, \\
&l_1 = \left(k\frac{\partial h_1}{\partial x} + \frac{\partial f}{\partial x} \Big/ \frac{\partial h_1}{\partial x} \right)_{x=\hat{x},\theta=\hat{\theta}}, \; l_2 = k\left(\frac{\partial h_2}{\partial x} \right)_{x=\hat{x},\theta=\hat{\theta}}, \\
&l_3 = k\left(\frac{\partial h_1}{\partial \theta} \right)_{x=\hat{x},\theta=\hat{\theta}}, \quad l_4 = k\left(\frac{\partial h_2}{\partial \theta} \right)_{x=\hat{x},\theta=\hat{\theta}},
\end{aligned}
\tag{3.25}
$$

and if k is positive, then Q is positive definite. This proof is shown in Appendix A.

By applying (3.25) to the system expressed in (3.12), we can build a locally stable observer that estimates state and parameter concurrently. The size of the region of attraction in e-domain depends on z and u. The observer with the gain (3.25) may not guarantee global stability. Global stability depends on the nature of the system nonlinearity. As a simple example, if the system has $r_1 - Lr_2 \neq 0$ meaning $\gamma>0$, and the output functions behave such that $l_3=0$ and $l_4=0$ at some states, then $\lambda_{min}(Q) = 0$ at those states because the last row of matrix A is 0 and thus the last row of $Q=-[(A-LC)^T P+P(A-LC)]$ is also 0. Therefore, the condition $\lambda_{min}(Q)\geq \gamma\|P\|$ is violated and we cannot use the sufficient condition to judge the global stability of this example system. However, the condition $l_3=0$ and $l_4=0$ at some states means that the

measurements have zero sensitivity to parameter changes at those states, and thus estimation of the parameter using the measurement is not possible.

We have assumed that the plant has no uncertainties and the observer has the same dynamics as the real plant. However, in fact plant uncertainties cannot be completely avoided and frequently cannot be parameterized. For example, vehicle mass and mass center position could change. Furthermore, tire characteristics are affected by the environment, which cannot be easily parameterized.

In this chapter, the robustness property that we focus on is the robust stability against plant uncertainties. The system is assumed to have uncertainties, ΔF and ΔH, as shown in (3.26). If the observer (3.18) is stable for the family of uncertainties under consideration, then it is said to be robust-stable.

$$\begin{aligned} \dot{z} &= F_0(z,u) + \Delta F(z,u), \\ y &= H_0(z,u) + \Delta H(z,u). \end{aligned} \tag{3.26}$$

Let us consider the following nominal representation of the true system (3.12):

$$\begin{aligned} \dot{z} &= F_0(z,u), \\ y &= H_0(z,u). \end{aligned} \tag{3.27}$$

Then, after the same "state augmentation" process shown in Section **Error! Reference source not found.**, the observer is

$$\dot{\hat{z}} = F_0(\hat{z},u) + L(\hat{z},u)\big(H(z,u) - H_0(\hat{z},u)\big), \tag{3.28}$$

and the error dynamics are

$$\begin{aligned} \dot{e} &= F(z,u) - F_0(\hat{z},u) - L(\hat{z},u)\big(H(z,u) - H_0(\hat{z},u)\big) \\ &= \big(A_0 - LC_0\big)e + (r_1 - Lr_2) + (\Delta F - L\Delta H), \end{aligned} \tag{3.29}$$

where

$$
\begin{aligned}
&e = z - \hat{z},\\
&A_0 = A_0(z,u) = \frac{\partial F_0(z,u)}{\partial z},\\
&C_0 = C_0(z,u) = \frac{\partial H_0(z,u)}{\partial z},\\
&r_1 = r_1(z,e,u) = F_0(z,u) - F_0(\hat{z},u) - A_0(z,u)e,\\
&r_2 = r_2(z,e,u) = H_0(z,u) - H_0(\hat{z},u) - C_0(z,u)e.
\end{aligned}
$$

The error dynamics of the observer having uncertainties consist of an error term of a nominal part, $(A_0 - LC_0)e + (r_1 - Lr_2)$ and an uncertainty part, $\Delta F - L\Delta H$.

Sufficient conditions for robust stability are well studied. For example, Khalil [38] has a comprehensive treatment of the conditions for stability of perturbed systems. To check robust stability of our observer, we follow Khalil's treatment. If we assume that the uncertain part in the error dynamics (3.29) vanishes when $x=0$, i.e. $\Delta F(0,0) - L(0,0)\Delta H(0,0)=0$, then there should be some positive constants c_1, c_2, c_3, and c_4 and a Lyapunov function $V(z, e, u)$ that satisfy the following:

$$
\begin{aligned}
&c_1 \|e\|^2 \le V(z,e,u) \le c_2 \|e\|^2,\\
&\frac{\partial V}{\partial t} + \frac{\partial V}{\partial z}\left\{ \left(A_0 - LC_0\right)e + (r_1 - Lr_2) \right\} \le -c_3 \|e\|^2,\\
&\left\| \frac{\partial V}{\partial z} \right\| \le c_4 \|e\|^2,
\end{aligned}
\tag{3.30}
$$

for all $(z,u) \in D \times U$, where $D \subset R^n$ and $U \subset R^m$ are domains that contain the origin $(z, u)=(0, 0)$, and the perturbation term must satisfy the linear growth bound,

$$
\left\| (\Delta F(z,e,u) - L(\hat{z},u)\Delta H(z,e,u)) \right\| \le \gamma \|e\|, \ \forall z \in D, \ \forall u \in U, \forall e, \tag{3.31}
$$

where $\gamma < c_3/c_4$ is a nonnegative constant. If (3.30) and (3.31) are satisfied then $e=0$ is an exponentially stable equilibrium point of the error dynamics having uncertainties (3.29).

This stability condition is found to be quite conservative and it may not be easy to find P and L satisfying the conditions because the uncertainty term in (3.31) is close to singular when (z, u) is close to the origin, which results in infinite γ. Therefore, it can be said that robust stability depends on observer states and inputs, which means we need to

determine when the observer is robust-stable in the (z, u) domain. One example where Khalil's results cannot be applied due to its conservativeness is shown in Chapter 3.2.2.2.

Let us define state dependent robust stability, which is less conservative than Khalil's conditions. In the following, we provide two definitions related to robustness: the stability region domain and the robust stability region in the state-input domain.

Stability region in the state-input domain, $S(\varepsilon)$, is defined as follow:

$$S(\varepsilon) = \{(z,u) \mid \dot{V}(z,e,u) < 0, \ for \ \forall e \in B(\varepsilon)\}, \tag{3.32}$$

where $B(\varepsilon) = \{e \mid e^T P e \le \varepsilon^2\}$ is a region of attraction whose upper bound is determined by ε. $S(\varepsilon)$ quantifies the stability of the observer under a given region of attraction when the plant is perfect.

Robust stable region in the state-input domain, $RS(d, \varepsilon_1, \varepsilon_2)$, is defined as follows:

$$\begin{aligned} RS(d,\varepsilon_1,\varepsilon_2) = \{(z,u) \mid \dot{V}(z,e,u) < -d, \\ for \ \forall e \in D(\varepsilon_1,\varepsilon_2), \forall \Delta F \in \Psi, \forall \Delta H \in \Theta\}, \end{aligned} \tag{3.33}$$

where d is a design parameter for fast convergence, Ψ is the union of all possible uncertainties in F, Θ is the union of all possible uncertainties in H, and $D(\varepsilon_1,\varepsilon_2) = \{e \mid \varepsilon_1^2 \le e^T P e \le \varepsilon_2^2\}$. $D(\varepsilon_1, \varepsilon_2)$ is the region of attraction allowing a steady state error referred by ε_1 (more details about $D(\varepsilon_1, \varepsilon_2)$ can be found in Figure 3.16). $RS(d, \varepsilon_1, \varepsilon_2)$ quantifies the stability of the observer under a given region of attraction and a bound of steady state error when the plant has uncertainties. $S(\varepsilon)$ and $RS(d, \varepsilon_1, \varepsilon_2)$ can be determined numerically by computing $\dot{V}(z,e,u)$ for all $\forall e \in B(\varepsilon)$ or $D(\varepsilon_1, \varepsilon_2)$, $\forall \Delta F \in \Psi$, and for $\forall \Delta H \in \Theta$, where $B(\varepsilon)$, $D(\varepsilon_1, \varepsilon_2)$, Ψ, and Θ are numerically given. For many nonlinear systems, numerical assessment of robust stability is the only viable method because no analytical solutions exist, and, in the rare cases where they do, the analytical solutions are typically too conservative to be useful for real applications. The one example that the analytical approach cannot handle is described in Chapter 3.2.2.2.

The size of region $RS(d, \varepsilon_1, \varepsilon_2)$ is dependent on P and L when d, ε_1, ε_2, $\mathcal{F}$, and $\mathcal{H}$ are given. Therefore, the observer design problem can be viewed as a robust stability design problem. The goal is to obtain optimal P^* and L^*:

$$(P^*, L^*) = \arg\max_{P,L} \{size\ of\ \ RS(d, \varepsilon_1, \varepsilon_2)\},$$
$$\{size\ of\ \ RS(d, \varepsilon_1, \varepsilon_2)\} = \iint_{RS(d,\varepsilon_1,\varepsilon_2)} 1\ dzdu, \tag{3.34}$$

where d, ε_1, and ε_2 is given as an observer requirement and the design for P and L shown in (3.25) can be relaxed to allow "observer gain selections" as follows:

$$P = \begin{bmatrix} p_1 & 0 \\ 0 & 1 \end{bmatrix},\ L = \begin{bmatrix} l_1 & l_2 \\ l_3 & l_4 \end{bmatrix}$$
$$l_1 = \left(k_1 \frac{\partial h_1}{\partial x} + \frac{\partial f_0}{\partial x} \Big/ \frac{\partial h_1}{\partial x} \right)_{x=\hat{x},\theta=\hat{\theta}},\ l_2 = k_2 \left(\frac{\partial h_2}{\partial x} \right)_{x=\hat{x},\theta=\hat{\theta}}, \tag{3.35}$$
$$l_3 = k_3 \left(\frac{\partial h_1}{\partial \theta} \right)_{x=\hat{x},\theta=\hat{\theta}},\ l_4 = k_4 \left(\frac{\partial h_2}{\partial \theta} \right)_{x=\hat{x},\theta=\hat{\theta}},$$

where p_1, k_1, k_2, k_3, and k_4 are positive real numbers. This relaxed P and L may lose local stability for some z and u because the local stability of the observer is demonstrated with the gain (3.25) where k_1=k_2=k_3=k_4=1 and p_1=1. However, the optimized P and L may increase the size of $RS(d, \varepsilon_1, \varepsilon_2)$.

To summarize, the numerical design process of the robust state and parameter observer is:

1) Construct the augmented form of observer, Eq.(3.28).
2) Derive partial derivatives of the nonlinear system equations to build P and L as shown in (3.35).
3) Determine d, ε_1 and ε_2 considering observer requirement, where d determines convergence rate, ε_1 is related to a steady state error and ε_2 is related to the maximum allowable initial estimation error.
4) Determine the range of possible plant uncertainties, Ψ, and Θ.
5) Perform the optimization problem by numerically computing the size of $RS(d, \varepsilon_1, \varepsilon_2)$ in the state space and determine p_1, k_1, k_2, k_3, and k_4.

3.2.2.2 Application: Slip Angle and Friction Coefficient Observer

Applying the developed design methodology for our friction estimation problem, the dynamics of front tire slip angle are derived from (2.1) and (2.2) as follows:

$$\dot{\alpha}_f = \left(\frac{1}{mv_x} + \frac{a^2}{I_z v_x}\right) F_{yf} + \left(\frac{1}{mv_x} - \frac{ab}{I_z v_x}\right) F_{yr} - r - \dot{\delta}, \tag{3.36}$$

where $F_{yf} = 2f_y(\alpha_f, \mu)\cos\delta$, $F_{yf} = 2f_y(\alpha_r, \mu)$, and $\alpha_r = \alpha_f - L/v_x + \delta$. The system state and parameter to be estimated are α_f and μ. The augmented system matrices for the nominal system are:

$$\begin{aligned} F_0(z,u) &= \begin{bmatrix} \left(\frac{1}{mv} + \frac{a^2}{I_z v_x}\right) F_{yf} + \left(\frac{1}{mv} - \frac{ab}{I_z v_x}\right) F_{yr} - r - \dot{\delta} \\ 0 \end{bmatrix} := \begin{bmatrix} f \\ 0 \end{bmatrix}, \\ H_0(z,u) &= \begin{bmatrix} F_{yf} + F_{yr} \\ 2\tau_a \end{bmatrix} = \begin{bmatrix} ma_y \\ 2\tau_a \end{bmatrix} := \begin{bmatrix} h_1 \\ h_2 \end{bmatrix}, \end{aligned} \tag{3.37}$$

where $\tau_a = \tau_a(\alpha_f, \mu)$ is the aligning moment presented in (2.13). Then, the observer model is as follows:

$$\begin{aligned} \dot{\hat{\alpha}}_f &= \left(\frac{1}{mv_x} + \frac{a^2}{I_z v_x}\right) \hat{F}_{yf} + \left(\frac{1}{mv_x} - \frac{ab}{I_z v_x}\right) \hat{F}_{yr} - r - \dot{\delta} \\ &\quad + l_1\left(ma_y - \left(\hat{F}_{yf} + \hat{F}_{yr}\right)\right) + l_2\left(\tau_a - \hat{\tau}_a\right), \\ \dot{\hat{\mu}} &= l_3\left(ma_y - \left(\hat{F}_{yf} + \hat{F}_{yr}\right)\right) + l_4\left(\tau_a - \hat{\tau}_a\right). \end{aligned} \tag{3.38}$$

Therefore, the augmented matrices of the actual system with plant uncertainties are

$$\begin{aligned} F(z,u) &= F_0(z,u) + \Delta F(z,u) \\ &= \begin{bmatrix} \left(\frac{1}{mv_x} + \frac{a^2}{I_z v_x}\right) F_{yf} + \left(\frac{1}{mV} - \frac{ab}{I_z v_x}\right) F_{yr} - r - \dot{\delta} \\ 0 \end{bmatrix} + \Delta F(z,u), \\ H(z,u) &= H_0(z,u) + \Delta H(z,u) \\ &= \begin{bmatrix} F_{yf} + F_{yr} \\ 2\tau_a \end{bmatrix} + \Delta H(z,u) \\ &= \begin{bmatrix} ma_y \\ 2\tau_a \end{bmatrix} + \Delta H(z,u), \end{aligned} \tag{3.39}$$

and the error dynamics of the observer are then

$$\begin{aligned}\dot{e} &= F(z,u) - F_0(\hat{z},u) - L(\hat{z},u)\big(H(z,u) - H_0(\hat{z},u)\big) \\ &= \begin{bmatrix} \left(\frac{1}{mv_x} + \frac{a^2}{I_z v_x}\right)\left(F_{yf} - \hat{F}_{yf}\right) + \left(\frac{1}{mv_x} - \frac{ab}{I_z v_x}\right)\left(F_{yr} - \hat{F}_{yr}\right) \\ 0 \end{bmatrix} \\ &\quad - L(\hat{z},u)\left(\begin{bmatrix} ma_y \\ 2\tau_a \end{bmatrix} - \begin{bmatrix} \hat{F}_{yf} + \hat{F}_{yr} \\ 2\hat{\tau}_a \end{bmatrix}\right) + \Delta F(z,u) - L(\hat{z},u)\Delta H(z,u).\end{aligned} \tag{3.40}$$

An exemplary stability region of the observer is shown in Figure 3.11. The stability region is evaluated in the reduced state space and the observer gain is determined by (3.25) where k=1. This observer gain is selected for local stability assuming no plant uncertainties.

$$\begin{aligned} l_1 &= \left(\frac{\partial h_1}{\partial x} + \frac{\partial f_0}{\partial x} \Big/ \frac{\partial h_1}{\partial x}\right)_{x=\hat{x},\theta=\hat{\theta}}, \; l_2 = \left(\frac{\partial h_2}{\partial x}\right)_{x=\hat{x},\theta=\hat{\theta}}, \\ l_3 &= \left(\frac{\partial h_1}{\partial \theta}\right)_{x=\hat{x},\theta=\hat{\theta}}, \; l_4 = \left(\frac{\partial h_2}{\partial \theta}\right)_{x=\hat{x},\theta=\hat{\theta}}. \end{aligned} \tag{3.41}$$

The dimension of the state space is reduced for efficient gain selection. In the error dynamics (3.40), it can be seen that (z, u) is characterized by α_f, r, δ, v_x, and μ. Assuming constant v_x and small change of cos(δ), limited by geometric constraints of the steering system, the major variables affecting the status of error dynamics (3.40) are reduced to [α_f, r, μ]. Furthermore, using the relationship of α_f and α_r, (2.2), and normalization to α_{fsl} or α_{rsl}, the variables that affect the dynamics, [α_f, r, μ] are transformed into [α_f /α_{fsl}, α_r /α_{rsl}], where α_{fsl} and α_{rsl} are the front and rear tire slip angle when the tire saturates. Therefore, we only consider the range, $|\alpha_f| \le \alpha_{fsl}$ and $0 < \mu \le \mu_{\max}$ =1, as the range of the states and for the same reason, we restrict the range of error to $|e_1| \le \alpha_{fsl}$ and $|e_2| \le \mu_{\max}$. We also define $e_{\max}=[\alpha_{fsl}, \mu_{\max}]^T$ and $\varepsilon_{\max}=(e_{\max}{}^T P e_{\max})^{1/2}$.

In the stability region plot, Figure 3.11, the area in red indicate regions where the observer is unstable with some initial errors contained in $B(0.1e_{\max})$. In these areas, the system nonlinearity has convex or concave points resulting in opposite dynamic trends around the points. As this observer is designed considering a perfect plant model and small region of attraction, stability may not be preserved when there are plant uncertainties.

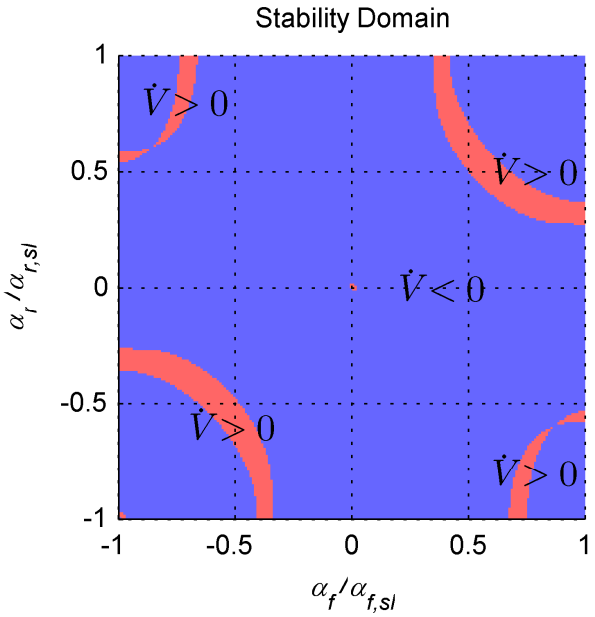

Figure 3.11 Stability region, $S(0.1\varepsilon_{\max})$, without plant uncertainties

To design an observer that is robust against plant uncertainties, we need to optimize the observer gain through the process suggested in Chapter 3.2.2.1. In order to follow the optimization process, we need to first define the set of plant uncertainties, Ψ and Θ. These plant uncertainties are defined using the following assumptions: the most important and common plant uncertainties originate from variations in vehicle mass and tire characteristics. While a vehicle is being driven, the vehicle mass changes slowly, the effect of which can be estimated using vehicle longitudinal dynamics. There are many vehicle mass estimation algorithms reported in the literature [39-42]. We can also lump the effect of mass uncertainty into the tire uncertainties, in which case, tire uncertainty becomes the single most important plant uncertainty. The tire uncertainties used in this evaluation are defined by the upper and lower bound curves, as shown in Figure 3.12.

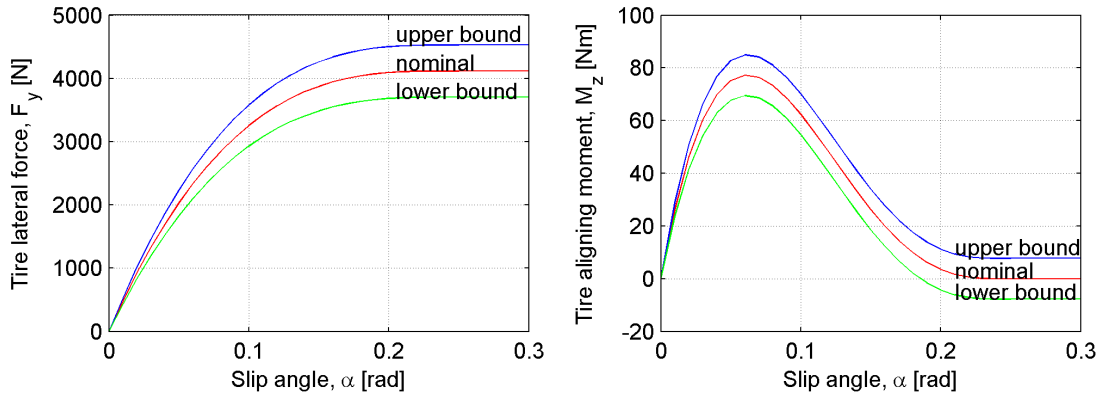

Figure 3.12 Tire uncertainties expressed in tire force curves

In the optimization search, the range of ε_1 and ε_2 are set at the level of $0.15\varepsilon_{\max}$ and $0.5\varepsilon_{\max}$, and d is set at $0.01\|P\|$. Using these conditions along with the initial estimate (3.42) obtained by trial and error, we obtained the optimal parameters for P and L as (3.43).

$$\begin{aligned} &p_1 = 1, \\ &k_1 = 4\times10^{-9},\ k_2 = 6.7\times10^{-6},\ k_3 = 2.4\times10^{-6},\ k_4 = 7.1\times10^{-3}. \end{aligned} \tag{3.42}$$

$$\begin{aligned} &p_1 = 52.4, \\ &k_1 = 2.5\times10^{-9},\ k_2 = 2.8\times10^{-6},\ k_3 = 1.8\times10^{-8},\ k_4 = 1.9\times10^{-4}. \end{aligned} \tag{3.43}$$

Two robust stable regions, $RS(d, \varepsilon_1, \varepsilon_2)$, with the un-optimized gains and with the optimized gains, are shown in Figure 3.13. The robust stability region of the observer using the optimized gains is much wider than that with the un-optimized gains. Even though the gains are optimized, the observer is still unstable when the front tire slip angle is small; in other words, if vehicle lateral excitation is small, then the estimation result is not reliable. This is understandable given the significant plant uncertainties. Furthermore, excessive front tire slip angle also induces an unstable estimation. A medium-sized excitation is thus preferable for the operation of the observer. This observation can be explained using tire force curves. In Figure 2.9, tire curves with different μ are not differentiable as the tire slip angle goes to zero. When the slip angle is large, lateral tire force curves with different μ are differentiable while aligning moment curves are not.

Large slip angles with tire uncertainties thus deteriorate the observability of the system. The latter problem is not an issue, however, because the robust observer developed in this chapter is only meant for medium excitation conditions. When the slip angle is high, we can use the maximum aligning moment method described in Chapter 3.1.1 for friction estimation.

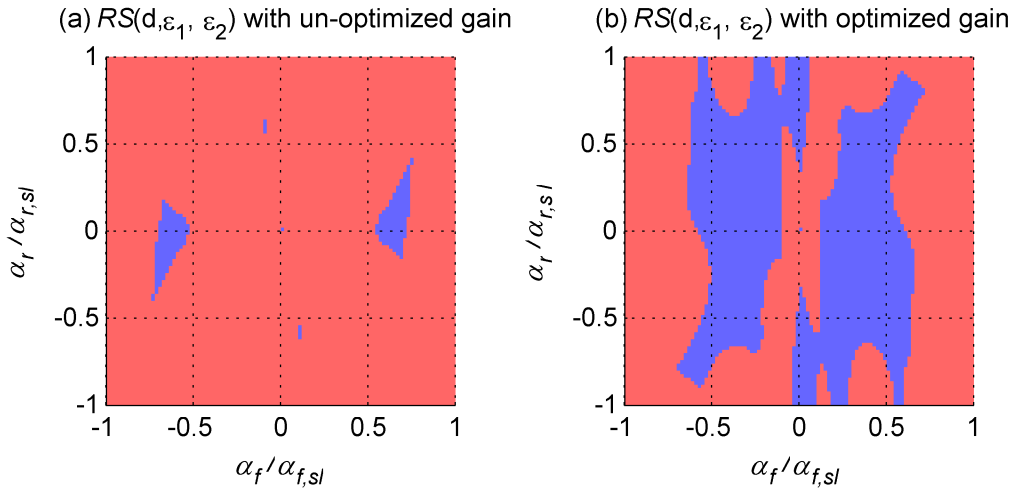

Figure 3.13 Robust stability region with the un-optimized gains and the optimized gains, when $\varepsilon_1=0.15\varepsilon_{max}$ and $\varepsilon_2=0.5\varepsilon_{max}$

We noted earlier that Khalil's robust stability theory can be applied only to a restrictive set of systems and the results could be quite conservative. In this chapter, we will apply Khalil's method to our observer. According to his theorem, to ensure robust stability, there needs to exist positive constants c_1, c_2, c_3, and c_4 and a Lyapunov function $V(z, e, u) = e^T P e$ must satisfy the following [38]:

$$c_1\|e\|^2 \le V(z,e,u) \le c_2\|e\|^2,$$

$$\frac{\partial V}{\partial t} + \frac{\partial V}{\partial z}\left\{\left(A_0 - LC_0\right)e + \left(r_1 - Lr_2\right)\right\} \le -c_3\|e\|^2,$$

$$\left\|\frac{\partial V}{\partial z}\right\| \le c_4\|e\|^2,$$

$$\left\|\left(\Delta F(\hat{z},e,u) - L(\hat{z},e,u)\Delta H(\hat{z},e,u)\right)\right\| \le \gamma\|e\|, \quad \forall \hat{z} \in D, \quad \forall u \in U, \forall e$$

$$\gamma < \frac{c_3}{c_4}$$

The constants c_1, c_1, and c_4 are easily determined using the following inequalities:

$$\sigma_{\min}(P)\|e\|^2 \le e^T Pe \le \sigma_{\max}(P)\|e\|^2,$$
$$\left\|\frac{\partial V}{\partial e}\right\| = \left\|e^T P + Pe\right\| \le 2\|Pe\| \le 2\|P\|_2 \|e\|.$$

Next, the following inequalities are deduced:

$$0 < c_1 \le \sigma_{\min}(P) = 1,$$
$$c_2 \ge \sigma_{\max}(P) = 52.4,$$
$$c_4 \ge 2\|P\|_2 = 104.8,$$

where P is selected to be the same as the optimized value identified in the previous chapter.

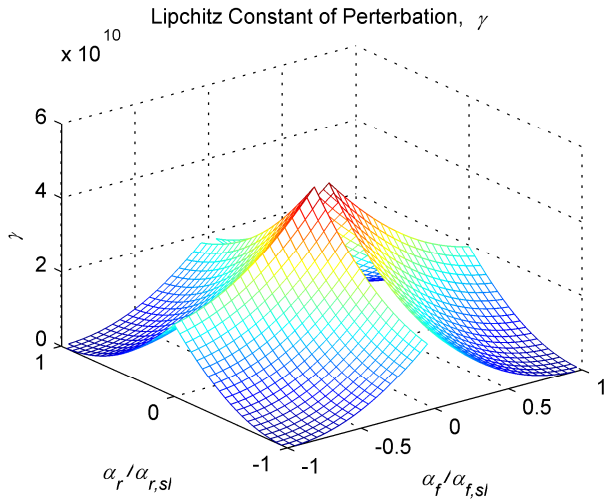

Figure 3.14 Calculation of Lipchitz constant of the perturbation part. The Lipchitz constant is achieved near the origin.

If there exists c_3 that satisfies $c_3 > \gamma c_4$, then the robust stability is guaranteed according to Khalil's theorem. If we consider the predefined bounded e, $\left\{e \,|\, \left|e^T Pe\right| \le 0.01 \cdot \left|e^T Pe\right|_{\max}\right\}$, then the Lipchitz constant γ can be plotted as shown in Figure 3.14. If we ignore the small slip angle region, $|\alpha_f| < 0.1\alpha_{fsl}$, then $\gamma \ge 4\times10^{10}$, which results in $c_3 \ge \gamma c_4 = 4.2\times10^{12}$. Therefore, robust stability is guaranteed if the following is satisfied for all e.

$$\left.\frac{dV}{dt}\right|_{norminal\ system} = \frac{\partial V}{\partial t} + \frac{\partial V}{\partial z}\left\{\left(A_0 - LC_0\right)e + \left(r_1 - Lr_2\right)\right\} \le -4.2\times 10^{12}\left\|e\right\|^2 . \qquad (3.44)$$

This inequality is not satisfied for almost all *e*. For example, the left part of the above inequality is evaluated with the error bounds $\left\{e \,|\, \left|e^T Pe\right| \le 0.01\cdot\left|e^T Pe\right|_{\max}\right\}$ and plotted in Figure 3.15, where the smallest value is -5×10^5, which means that the inequality (3.44) is satisfied only with $|e|<1\cdot 10^{-3}$, meaning that local stability is guaranteed in a very small region. This example confirms that Khalil's theorem, while theoretically rigorous, cannot be applied to prove robust stability for our estimation problem and it provides no guidance in the selection of observer gains. Therefore, the numerical method proposed in the previous chapter is utilized for our problem.

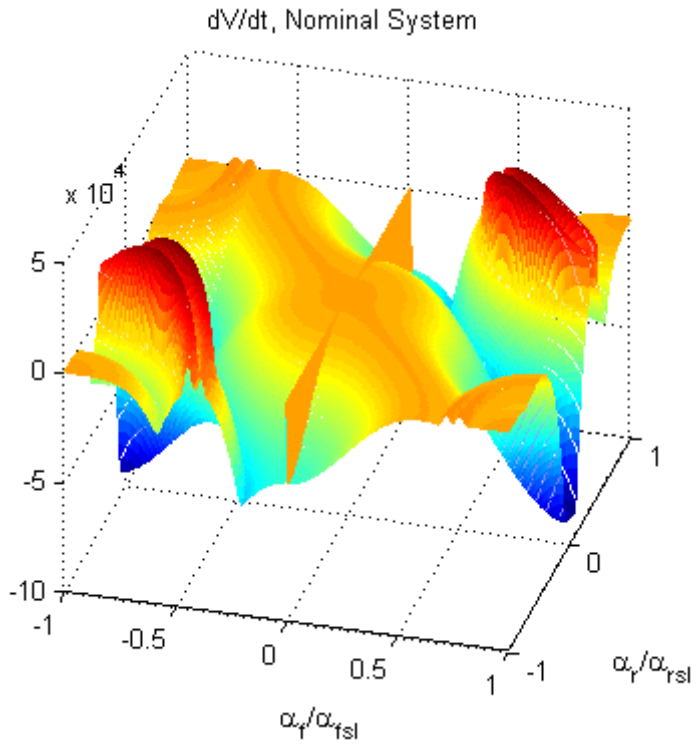

Figure 3.15 The time derivative of the Lyapunov function of the nominal system

In this chapter, robust gains were found through numerical optimizations. However, we used the region of attraction $D(\varepsilon_1, \varepsilon_2)$ with fixed ε_1 and ε_2 as one of the optimization conditions. Therefore, we can interpret the results shown in Figure 3.13 as

follows: first, the observer may not provide a good estimation if the vehicle states are in the unstable (red-colored) region, even if the initial estimation error is small. Second, the observer will provide good estimation if the initial estimation error is small and if the vehicle states are in the stable (blue-colored) region.

The size of the region of attraction depends on the vehicle states. For example, evaluation of $\dot{V}$ at $(\alpha_f, \alpha_r) = (0.4\,\alpha_{fsl}, 0.3\,\alpha_{rsl})$ for all possible $e = \{(e_1, e_2) \mid -\alpha_{fsl} \leq e_1 \leq \alpha_{fsl},\ -\mu_{max} \leq e_2 \leq \mu_{max}\}$ is shown in Figure 3.16. Two concentric circles show the trajectories of constant V. We can interpret the evaluation results as follows: if the initial error is inside the outer circle, the estimation error will decrease as long as it remains outside of the inner circle, where $\dot{V}$ become positive, as shown in the red-colored area in Figure 3.16. In other words, the observer of the plant that has uncertainties provides a stable estimation within a permissible initial error range, and the estimation will converge to the neighborhood of the true value, but may not reach the true value. The radius of the inner circle indicates the expected value of the "steady-state" estimation error. Furthermore, the radii of the two circles at every vehicle state are different, meaning that permissible initial error and the steady-state estimation errors are dependent on vehicle states. The two radii, ε_1 and ε_2, can be obtained for all vehicle states. Selected cases are illustrated in Figure 3.17.

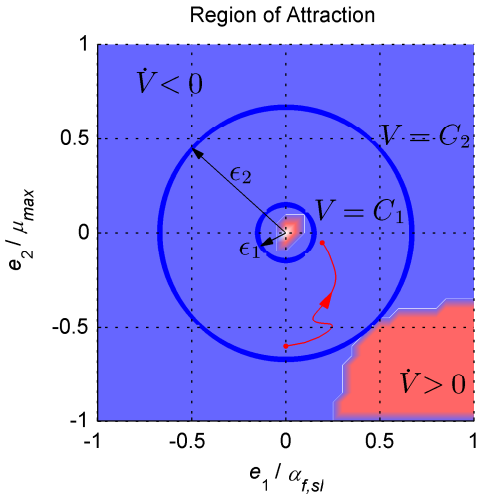

Figure 3.16 Region of attraction under the plant uncertainties depicted in Figure 3.12

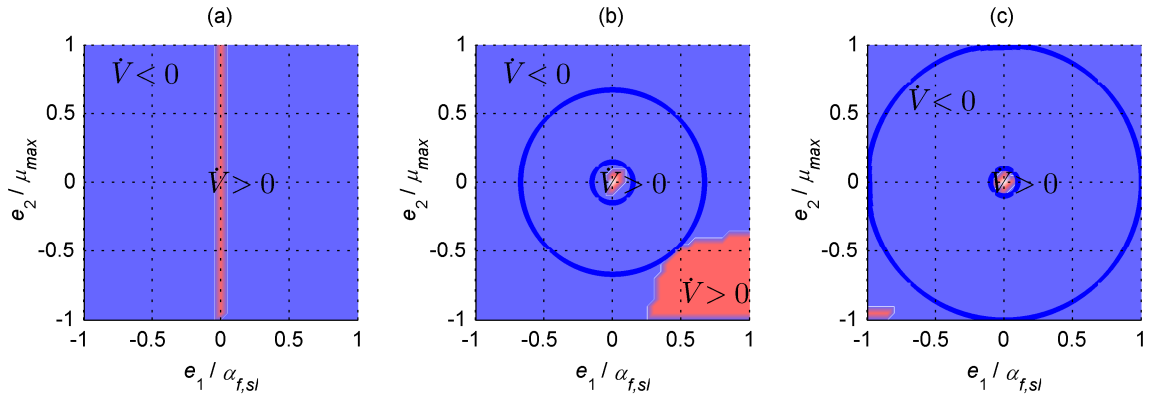

Figure 3.17 Selected cases of region of attraction; estimated vehicle state (α_f , α_r) is (0, 0) in plot (a) , ($0.4\,\alpha_{fsl}$, $0.3\,\alpha_{rsl}$) in plot (b) , and ($-0.4\,\alpha_{fsl}$, $0.3\,\alpha_{rsl}$) in plot (c).

No region of attraction in the strict sense of the term exists in case (a), and the observer might be unstable for some initial errors. There is a sizable region of attraction with locally unstable origin in case (b). There is a very small unstable region in case (c) where the observer is almost always stable for any initial error except when the error is close to the origin. These three cases illustrate the definitions of ε_1 and ε_2, which represent the stability and estimation accuracy of the observer at selected estimated vehicle states. The two values ε_1 and ε_2 for all vehicle states are shown in Figure 3.18.

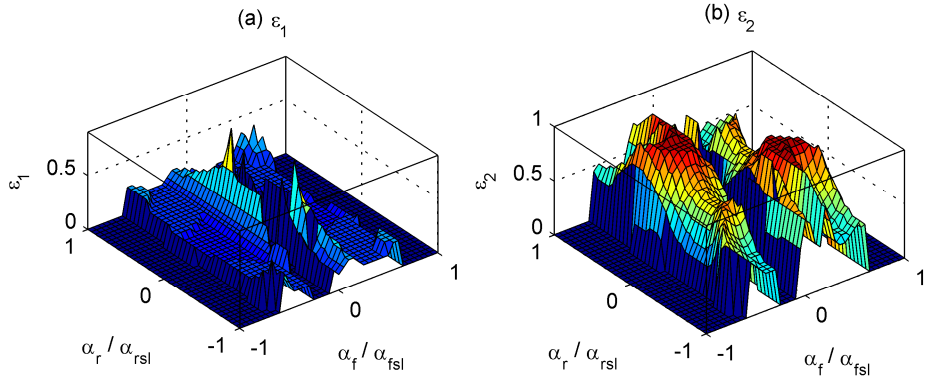

Figure 3.18 Steady state error ε_1 and radius of region of attraction ε_2

From these two plots, we can conclude the following: first, the observer stability is largely dependent on α_f and has a much weaker relationship with α_r; second, when excitation is medium (α_f is not too large and not too small), the observer is very stable

(large ε_2) and accurate (small ε_1); and third, when the excitation is very small or very large (vehicle is moving straight or vehicle has a large tire slip), the observer is unstable.

We verified the performance of the estimator (3.38) with the gains (3.43) using the Carsim simulation software. The vehicle speed is 60 km/h and the steering input is a 0.25Hz sinusoidal signal with a magnitude of 0.04 rad. The simulation results are shown in Figure 3.19. The observer is stable for all four friction levels. On a low friction road, the observer fluctuates when α_f is around zero. This result is consistent with the stability analysis performed in the previous section, i.e., the observer might be unstable when α_f is very small or very large. The biased estimation error when μ=1.0 is due to the tire model error, as explained in Chapter 3.2.1.4. The model errors results in an unstable region inside the region of attraction, which causes a "steady-state" estimation error.

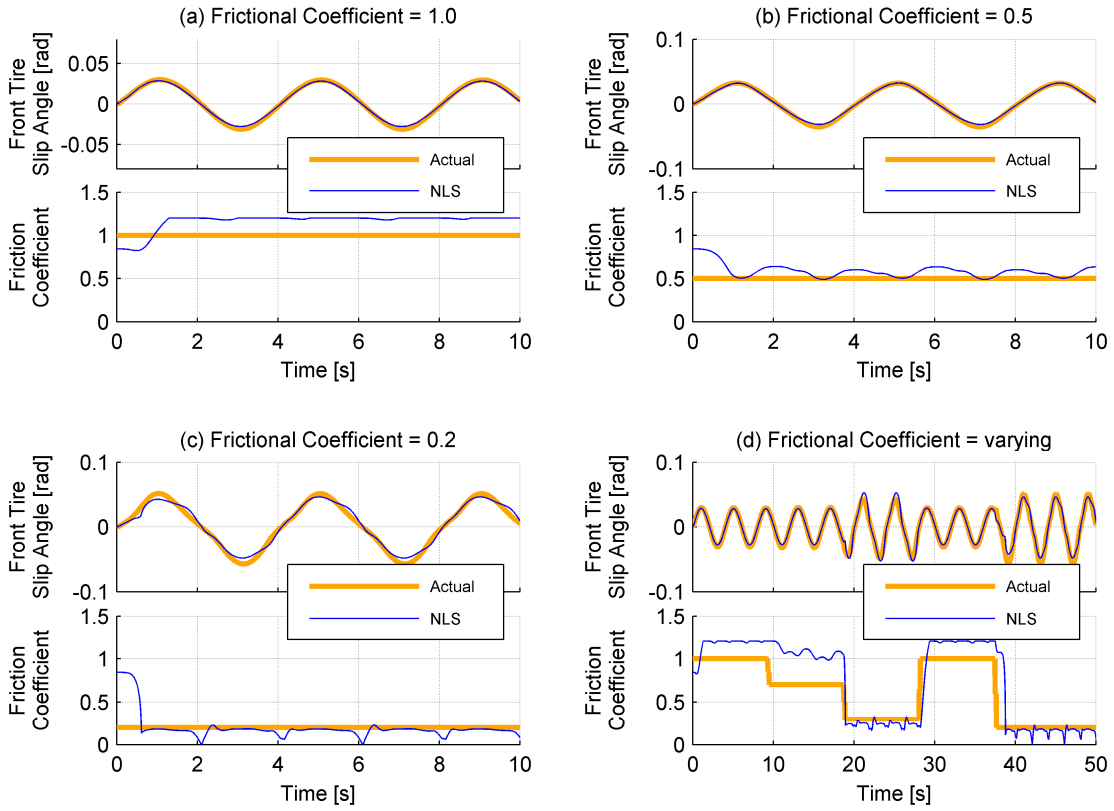

Figure 3.19 Simulation results of the nonlinear observer

On a high friction surface, the estimate of α_f is quite accurate, whereas μ is overestimated. However, on a low friction road, such as when the friction coefficient is 0.5 or 0.2, estimation of μ is more accurate while the estimate of α_f becomes poor. One of

the reasons for this difference in estimation accuracy is the loss of observability of the tire slip angle when slip angle is large. In Figure 1.2, if the tire slip angle is larger than 0.05 radian and if the friction coefficient is 0.2, it becomes very difficult to differentiate different tire slip angles. A vehicle has a larger slip angle on a low friction road than on a high friction road with the same steering input, and, therefore, the slip angle estimate on a slippery road is not as accurate as the estimate of the friction coefficient. More specifically, the tire characteristic curves diverge more when the friction coefficient is small, whereas, the curves aggregate densely if the friction coefficient is large, as shown in Figure 3.20. In other words, tire characteristic curves are insensitive to slip angle changes, but are sensitive to friction coefficient changes as the friction coefficient becomes smaller.

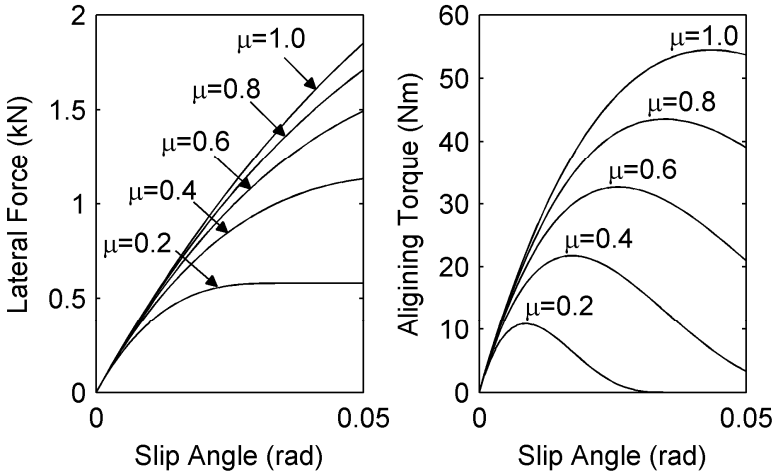

Figure 3.20 Effect of friction coefficient on tire characteristics

3.2.2.3 Extended Nonlinear Observers

3.2.2.3.1 Estimator Using Combined Algebraic and Dynamic Approaches

We previously discussed two different state and parameter estimators: the first is a nonlinear least squares estimator and the second is an adaptive nonlinear observer. The first estimator has the advantage of an estimated friction coefficient that is robust to noisy measurements because the estimator uses past data to estimate the friction coefficient. Because of this, however, the estimation response is slow, and in addition, getting the

best estimate of friction coefficient and slip angle is not guaranteed due to singularities in the relationship between measurement and the unknown parameters. The second estimator has the advantages of more accurate slip angle estimation and faster response to road surface change compared to the first estimator, yet is disadvantageous because it shows unstable estimation when α_f or a_y are small and convergence of estimation is not guaranteed when the excitation is not rich enough. In contrast, the least squares estimator based on a moving data window may avoid the divergence of parameter estimation if excitation is rich within the moving data window. These conclusions are supported by the simulation results shown in Figure 3.21. We, therefore, suggest a combined estimator that integrates the observer and the nonlinear least squares to mitigate the disadvantages of both.

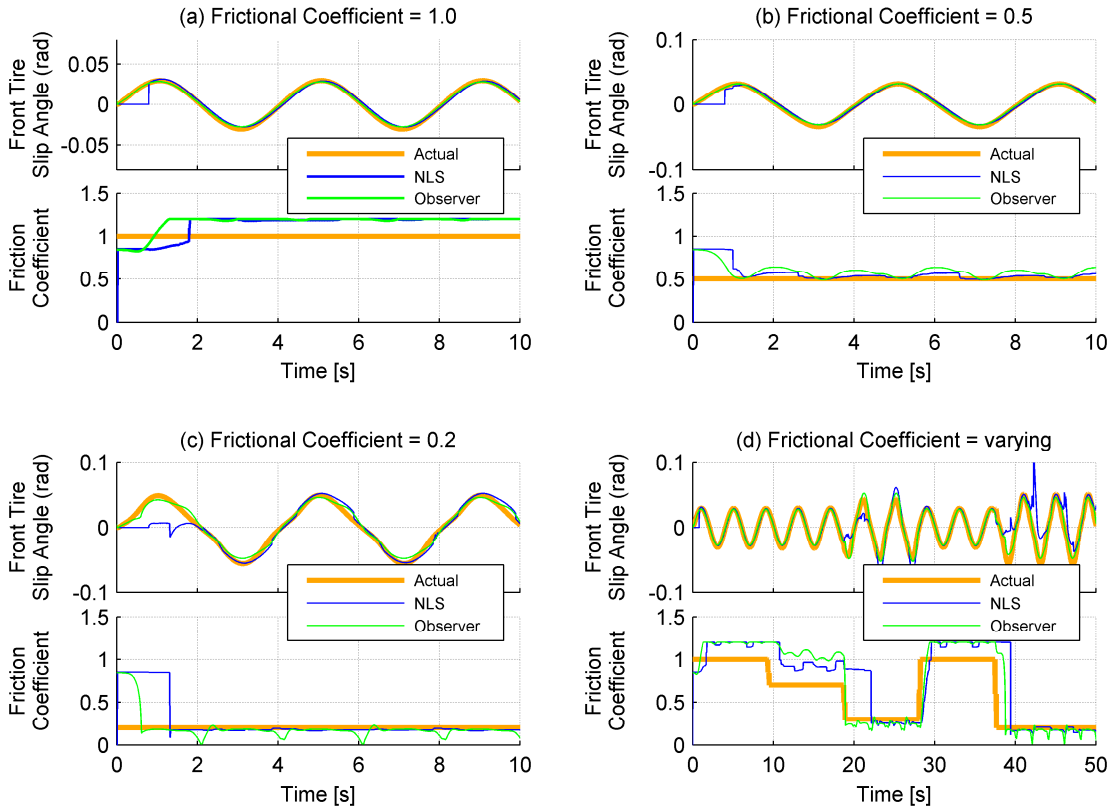

Figure 3.21 Comparison of the algebraic approach and the dynamic approach

The basic idea of the combined estimator is that the nonlinear observer estimates the front tire slip angle and the nonlinear least squares estimator identifies the friction coefficient. The overall structure of the combined estimator is shown in Figure 3.22.

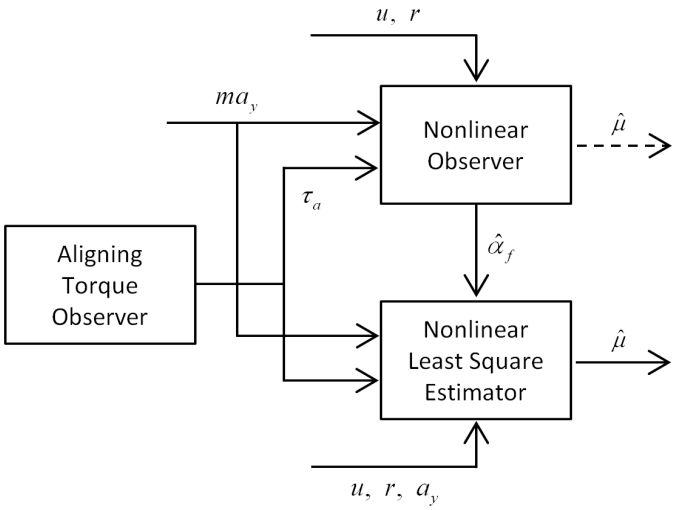

Figure 3.22 Structure of the combined estimator

The nonlinear observer is shown in (3.45), which is the same as (3.38), but we do not take the friction coefficient estimated by the observer as the final output of the combined estimator. The nonlinear observer only provides the estimated front tire slip angle to the nonlinear least squares estimator.

$$\begin{aligned}\dot{\hat{\alpha}}_f = &\left(\frac{1}{mv_x}+\frac{a^2}{I_z v_x}\right)\hat{F}_{yf}+\left(\frac{1}{mv_x}-\frac{ab}{I_z v_x}\right)\hat{F}_{yr}-r-\dot{\delta}\\ &+l_1\left(ma_y-\left(\hat{F}_{yf}+\hat{F}_{yr}\right)\right)+l_2\left(\tau_a-\hat{\tau}_a\right),\end{aligned} \tag{3.45}$$

The nonlinear least squares estimator shown in Figure 3.22 is different from the nonlinear least squares estimator described in Chapter 3.2.1 because we no longer need to estimate the tire slip angle. The slip angles are estimated by the nonlinear observer embedded in the combined estimator. Therefore, a nonlinear least squares problem for this case is

$$\mu_k = \arg\min_{\mu_k} J(k,\mu_k), \tag{3.46}$$

where

k=1, 2, 3, …,

$$J(k,\mu_k) = \left|\vec{F}_y(k)-\hat{\vec{F}}_y(k,\mu_k)\right|^2+\gamma\left|\vec{\tau}_a(k)-\hat{\vec{\tau}}_a(k,\mu_k)\right|^2,$$

γ : *weighting factor*,

$$\vec{F}_y(k) = \left[ma_{y,k-n+1},\ ma_{y,k-n+2}, \cdots, ma_{y,k} \right]^T,$$

$$\hat{\vec{F}}_y(k,\mu_k) = \left[\hat{F}_y(k-n+1,\mu_k), \cdots, \hat{F}_y(k,\mu_k) \right]^T,$$

$$\hat{F}_y(j,\mu_k) = f_{yf}(\alpha_{f,j},\ \mu_k)\cos\delta_j + f_{yr}(\alpha_{r,j},\ \mu_k),$$

$$\hat{\vec{\tau}}_a(k) = \left[\tau_{a,k-n+1},\ \tau_{a,k-n+2}, \cdots, \tau_{a,k} \right]^T,$$

$$\hat{\vec{\tau}}_a(k,\mu_k) = \left[\hat{\tau}_a(\alpha_{f,k-n+1},\ \mu_k), \cdots, \hat{\tau}_a(\alpha_{f,k},\ \mu_k) \right]^T,$$

$$\alpha_{r,j} = \alpha_{f,j} - \frac{Lr_j}{v_{xj}} + \delta_j,$$

$(\ )_j$: an estimated or measured property of at time step j.

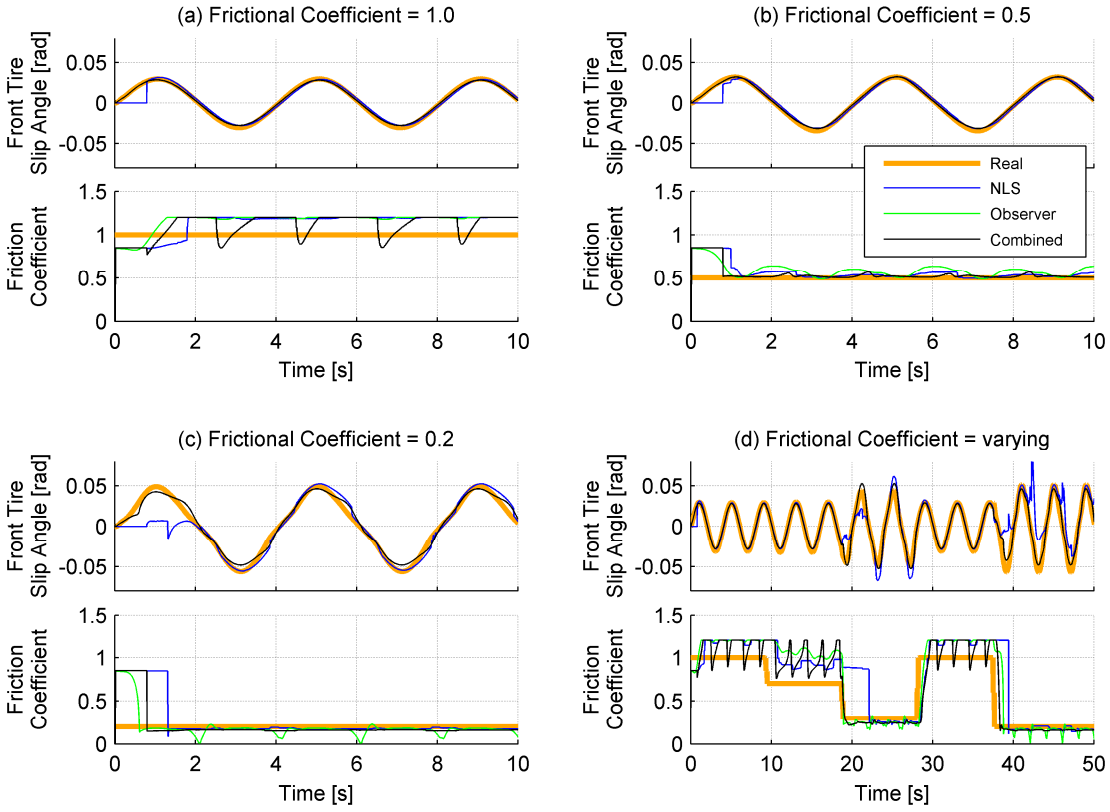

Figure 3.23 Comparison of the three estimators

This nonlinear least squares problem has fewer parameters to estimate than those discussed in Chapter 3.1 so the computational load decreases. We verify the performance of the estimator using the Carsim simulation software. The vehicle speed is 60 km/h and the steering input is 0.25Hz sinusoidal signal with a magnitude of 0.04 rad. The results

are shown in Figure 3.23. The slip angle estimated by the nonlinear observer and the slip angle estimated by the combined estimator are the same so that the two lines are overlap. In plots (c) and (d), the combined estimator shows more accurate slip angle estimation than the nonlinear least squares estimator and also has faster responses to surface changes than the nonlinear least squares estimator. Furthermore, the simulation results on the low-μ-surfaces have less fluctuation than the nonlinear observer when the slip angle is small. In summary, the combined estimator has the following advantages: i) it is less computationally intensive; ii) it has faster responses; iii) it provides a more accurate slip angle estimation than the nonlinear least square estimator; and iv) it is more stable in friction estimation than the nonlinear observer when the slip angle is small.

3.2.2.3.2 Observer with Switching-Gains

Friction levels of a road can change abruptly, whereas vehicle lateral dynamics states, such as yaw rate or body slip angle, usually continuously vary. For example, a car being driven in winter can experience abrupt surface change from asphalt to ice. In this case, the estimator must detect the surface change quickly and estimate the friction coefficient accurately. However, it did not track the surface change fast enough in Figure 3.19 (d) and Figure 3.24. This slow tracking is due to the fact that the difference between the true friction coefficient and estimated friction coefficient is large and it, therefore, takes time to converge to the true value even when the excitation is rich.

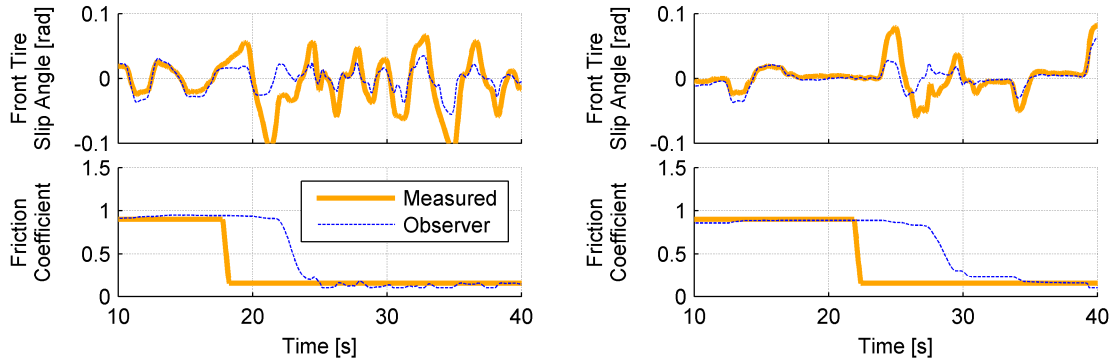

Figure 3.24 Estimation results of the nonlinear observer on surfaces with step change in road friction

Driving on the so-called μ-jump surface can be approximated as a hybrid dynamic system with discrete parameters. The observers for this hybrid system can be modeled as a continuous observer with an event detector [43]. The concept is simple: there is an estimation supervisor that detects a parameter change and controls the flow of estimation, as shown in Figure 3.25. If the estimation supervisor detects a parameter change, then the supervisor switches to one of the continuous observers corresponding to the current parameter. This type of observer is referred to a switching observer for a switching system.

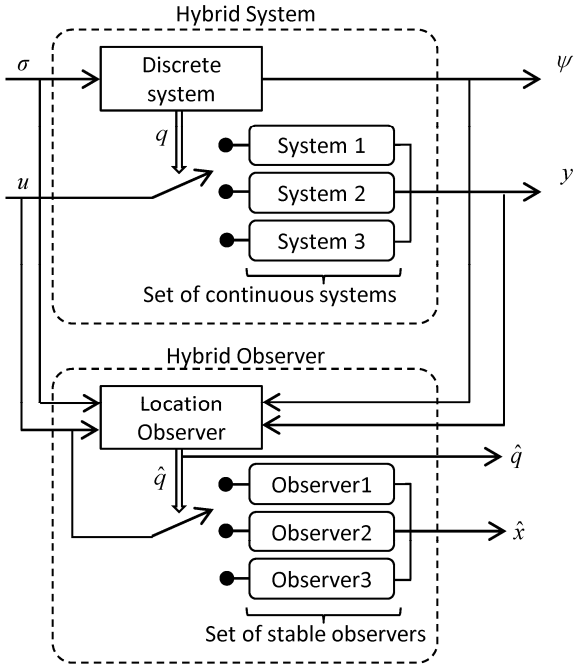

Figure 3.25 Conceptual plot of the estimation process of a switching-gain observer

Unfortunately, we cannot directly apply this approach to our case, because we do not know the exact value of the friction coefficient, and the friction coefficient is not a discrete parameter. It is hard to detect the current parameter right after a discrete change happens, but it is possible to detect whether a change has occurred from the abrupt change of vehicle dynamic states. Therefore, we only switch the observer gains and not the observer itself when a change occurs. This switching gain method does not detect the current parameter like a switching system, but it can reduce the convergence time by

using proper gains. The structure of the hybrid observer and the estimation process concept are shown in Figure 3.26 and Figure 3.27, respectively.

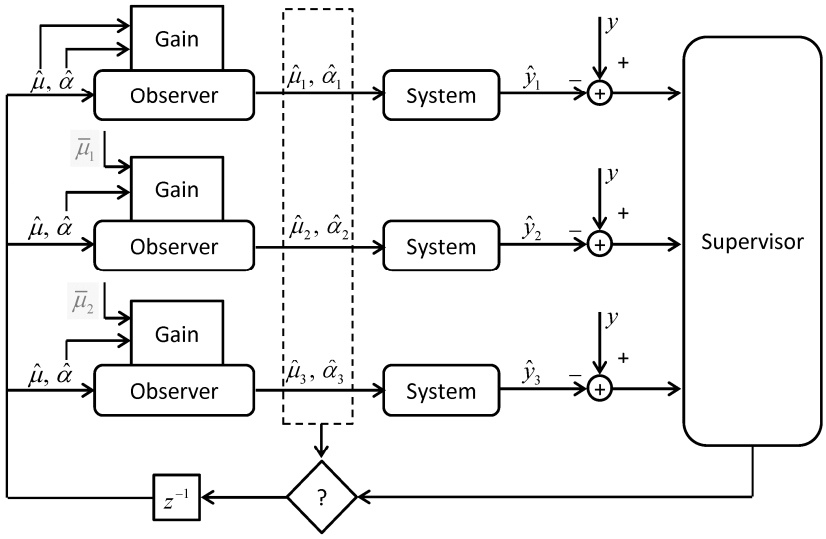

Figure 3.26 Switching-gain observer

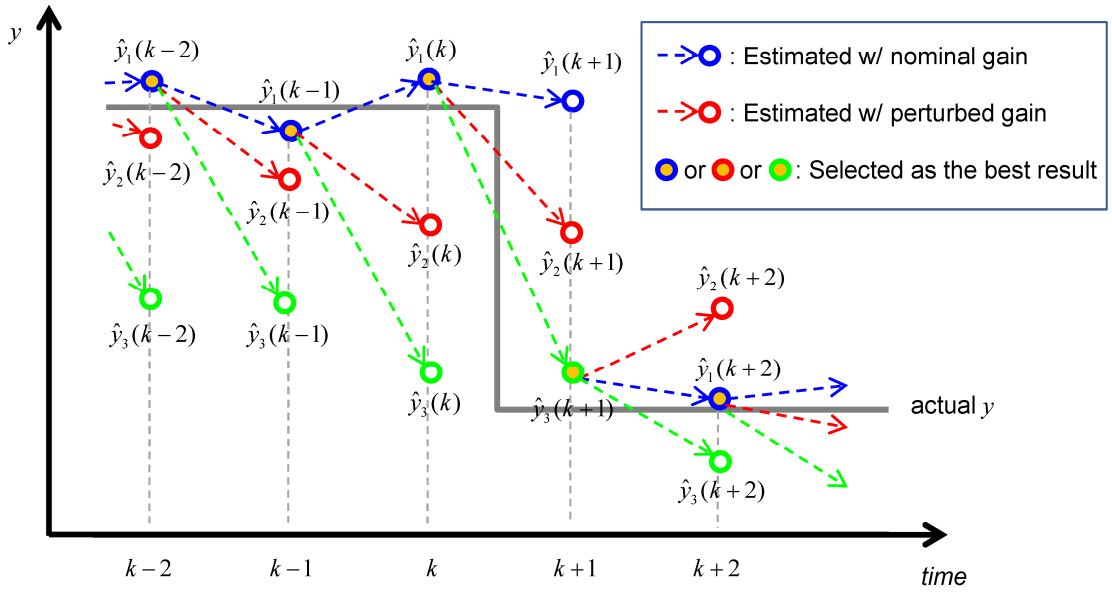

Figure 3.27 Estimation process of switching-gain observer

The detection on abrupt parameter and which set of gains to use is made by comparing the error between the measurement and observer outputs as follows:

(3.47)

$$\varepsilon_k = \sqrt{(y-\hat{y}_k)\begin{bmatrix}1 & 0\\ 0 & \sigma\end{bmatrix}(y-\hat{y}_k)^T}, \quad for \quad k=1,\,2,\,3,$$

where σ is a weighting factor. By comparing the errors, we can choose the estimated states from the observer with a set of gains that result in the smallest error. Furthermore, we introduce accumulated errors with a forgetting factor for decision-making to avoid frequent switching. The accumulated error with a forgetting factor λ is as follows:

$$acc\_\varepsilon(k) = \varepsilon(k) + \lambda \cdot acc\_\varepsilon(k-1). \tag{3.48}$$

The evaluation of this observer is shown with experimental data on μ-jump surfaces in Figure 3.28. The switching gain observer shows faster tracking in the case of an abrupt surface change.

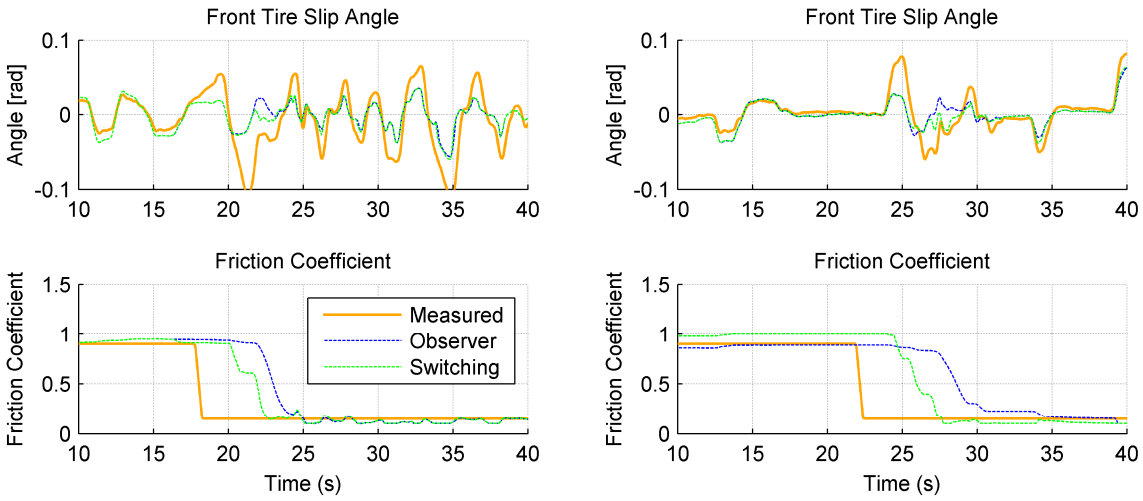

Figure 3.28 Comparison between the nominal observer and switching-gain observer

3.3 Summary

Two estimators based on lateral dynamics were developed. The nonlinear least squares estimator recursively solves a nonlinear optimization problem to estimate the friction coefficient and slip angles. The nonlinear observer uses vehicle lateral dynamics as the basis for the input/output relationships. Because the two approaches share the same estimation basis, the characteristics of estimation, such as the required excitation levels

and estimation limitations, are similar. However, the computational requirements, which are important for real time implementation, are quite different. The estimator based on nonlinear least squares shows generally stable estimation results, but does not always guarantee stability and it is difficult to quantify the stability and convergence. Furthermore, a critical drawback of the least squares method is large computation load. If we use a low-speed microprocessor, such as one that is commonly used for automotive applications, it may not sustain the same level of performance. Therefore, the nonlinear observer is appropriate for implementation. To take advantage of the benefits of both approaches, the two methods are combined to have smaller fluctuations in the friction coefficient estimation with smooth slip angle estimation. Also, to cope with abrupt surface changes, a switching gain method is adopted for the nonlinear observer. The nonlinear observer with a switching gain will be used as friction estimator for medium excitations because it is less computationally demanding and is responsive to surface changes.

CHAPTER 4
LONGITUDINAL DYNAMICS BASED ESTIMATION

The relationship between longitudinal slip and longitudinal tire force is frequently used as a basis of friction estimation because the related signals are easily available from wheel speed sensors. The relationship involves the traction force generation characteristic of the tire and many tire model models have been developed to describe these characteristics. With respect to the small slip range, linear models [44-46] can be used because one can observe the proportional relationship between the longitudinal tire forces and slip ratio from experiments, but the linear relationship is valid only in the small slip range (0~2%) because the tire force generation becomes nonlinear as the slip ratio increases. For the larger slip range, extensive nonlinear longitudinal force models [29, 31] are used but they have more parameters than the linear models. These multiple parameters may cause a convergence issue and sometimes the parameters do not have physical meaning. Some studies used a nonlinear model that has fewer numbers of parameters or they reduced the number of parameters to estimate by using additional assumptions. For example, Liu [14] used the Brush tire model with an adaptive estimator to estimate the friction coefficient. Once the tire properties are given, the longitudinal force curves are determined only by a parameter, μ. Canudas-de-Wit [47] used the LuGre model [48] that has two parameters, μ_S and μ_C, which can be used to adjust the force curve shape, once tire properties are given. In order to avoid multiple parameter estimation, he assumed that the two parameters are proportional to each other and introduced a scaling parameter θ to set the two parameters μ_S and μ_C as constants.

By using a force generation model that has a single parameter, estimation of the friction coefficient can be handled over a large range of slip ratio with less concern of convergence issues until the model is valid. However, the model uncertainties caused by the factors not being considered, such as the vehicle dynamic states, tire wear of the tire, temperature, and the inflation pressure, cannot be represented by the single parameter.

Also, the simple nonlinear models do not have differentiability between force curves with different friction coefficients at a small slip range (0-2%), as shown in Figure 4.1. Test results [20, 45, 49, 50], though, shows that the differentiation at the small slip range is possible and many papers on friction estimation [44-46] have used this property.

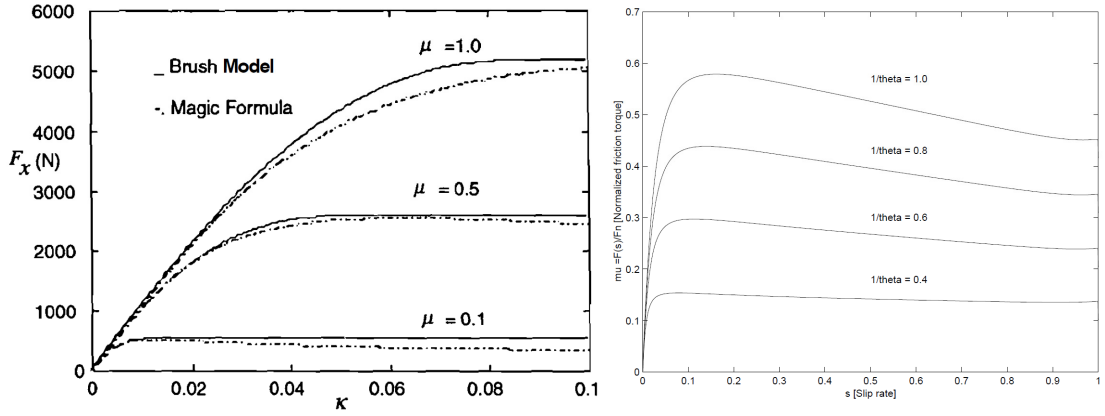

Figure 4.1 Longitudinal tire force curves used for friction coefficient estimation by Liu (left) and by Canuda de Wit (right)

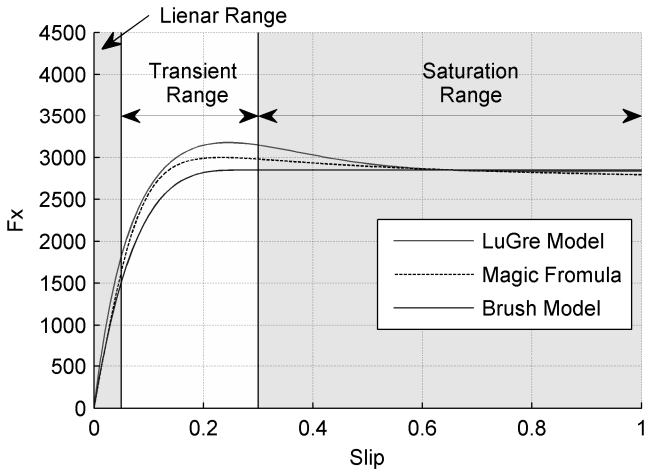

Figure 4.2 Longitudinal tire force generation in three ranges

As shown in Figure 4.2, there are three distinct ranges of force generation: linear, transient and saturation ranges. In the linear range, the force generation curves can be modeled as a linear function and the gradient of the linear function is believed to be dependent on the friction coefficient, which is shown in Figure 4.6 and Figure 4.22. In the saturation range, the force generation becomes insensitive to the slip ratio and is

mostly dependent on the friction coefficient and the tire normal force, which is shown in Figure 4.3 and Figure 4.4. In the transient range, the force curves are affected by not only the friction coefficient but also vehicle dynamic states and road surface materials which are not represented only by the friction coefficient.

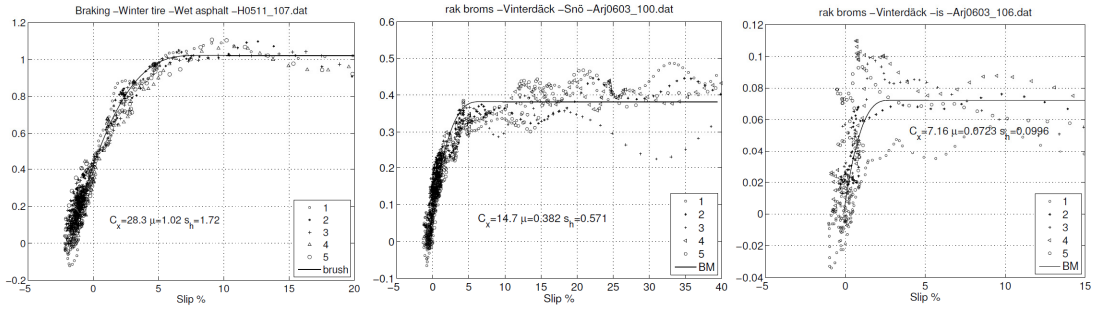

Figure 4.3 Tire longitudinal force versus wheel slip ratio for three surfaces [51]; the left plot is on concrete, the middle plot is on snow, and the right plot is on ice. The longitudinal tire force at large slip ratio is insensitive to slip ratio and dependent on surface conditions.

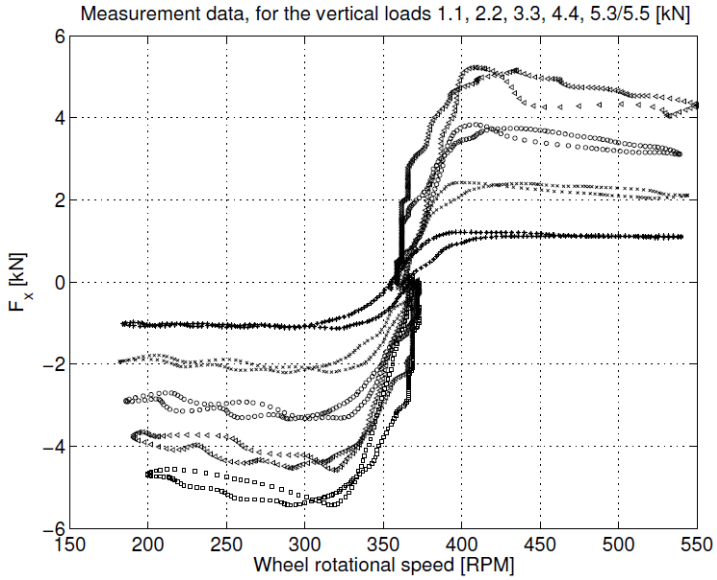

Figure 4.4 Tire longitudinal force versus wheel rotational speeds for several vertical loads plotted using tire test data [51]; The tire longitudinal force becomes insensitive to wheel speed as the tire force saturates.

Therefore, it is not effective to use a single nonlinear model having a parameter to represent the tire behaviors in the three ranges. With respect to representing the force generation at the transient range in particular, we may need a multiple parameter model,

which causes a multiple parameter estimation problem. Furthermore, in the transient range, electric slip control systems, such as ABS and TCS, will be activated and, therefore, the force/slip relationship is affected by the operation of the control system. In this range, other approaches using the internal information of the electric slip control systems can be used to estimate the friction coefficient. For example, Capra [52] utilized a look-up table to relate the kind of braking, wheel deceleration, and brake pressure to estimate the friction coefficient. The estimation algorithm is activated only during a short period from when the brake pedal is pressed until the ABS intervention starts. Sui [53] modeled wheel force and torque models for ABS operation and designed an estimator for the friction coefficient. In the algorithm, the excitation for the estimation is pulsed braking torque generated by the ABS operation, with the braking torque computed from the pressure signals of the ABS unit. Estimation of the friction coefficient during ABS operation requires the internal signals of ABS and modification of the ABS control algorithm. The following sections will focus on only the linear region (0~2%) and the saturation region (30~100%).

4.1 Phenomena in the Tire Contact Patch

4.1.1 Tire Longitudinal Force in the Linear Range

In daily driving, passenger cars usually undergo small lateral acceleration most of the time. Thus, friction estimation algorithms requiring medium lateral excitations may not be effective. In addition, when the cars are being driven on straight roads, most of the time the longitudinal acceleration level is also low. The only available excitation is the traction torque, which is at low levels maintaining vehicle speed.

Small longitudinal excitation, i.e. near-constant torque and small longitudinal slip is challenging for detecting the friction coefficient of a road surface. In traditional tire models, tire longitudinal force curves under different friction levels overlap with each other in the linear range, which implies that it is difficult to differentiate the force-slip curves at different friction levels. For example, longitudinal force curves of the Brush tire model shown in Figure 4.5 are very close to each other in the low slip ratio range of 0~0.02. This is because when tire slip is low, the tire force generation depends more on

the tread stiffness, than on the friction coefficient. However, some of the experimental data in the literature [20, 45, 54, 55] have shown that the friction coefficient greatly affects force generation even in the small slip range. Test data from one such study is plotted in Figure 4.6. Furthermore, several papers [20, 45, 54, 55] have been published using small longitudinal excitations to estimate road surface friction levels. Most of them rely on the hypothesis that tire longitudinal force increases as the road friction coefficient increases at the same slip ratio, which is not explained by physical tire models such as the Brush model. While some papers [49, 54] explain the discrepancy between observed phenomenon and the physical models, the reason for friction dependent force generation in the linear range is not well explained in them.

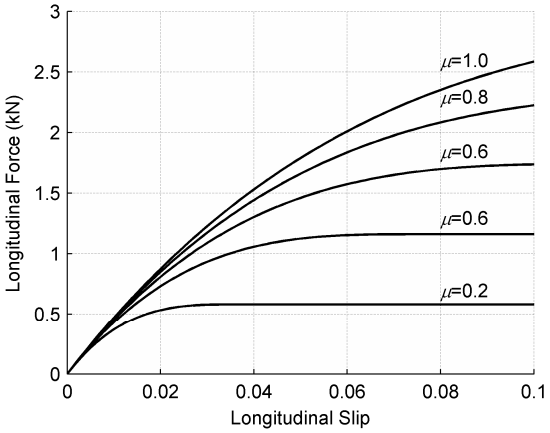

Figure 4.5 Tire longitudinal force curves of the Brush tire model

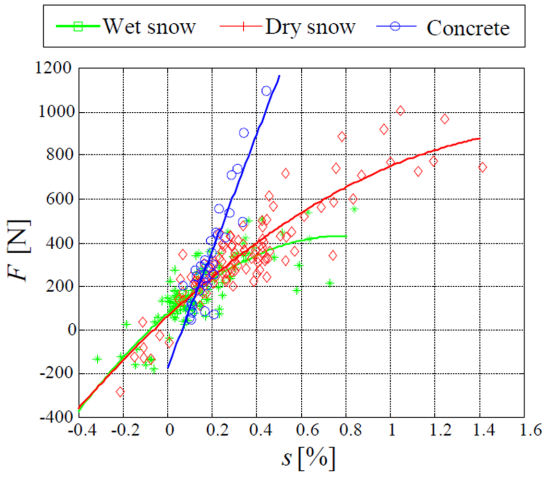

Figure 4.6 Tire longitudinal force curves from experiment [49]

In this section, we will investigate several phenomena in the tire contact patch that affect the tire force generation mechanism. Subsequently, a longitudinal tire force model is proposed that is consistent with experimental results. Finally, a friction estimation algorithm based on the longitudinal tire force model will be introduced.

4.1.2 Phenomena in the Tire Contact Patch

Tire forces in three directions, i.e. longitudinal, lateral, and vertical, are generated through the contact surface between the tire and the road – the so-called contact patch. The stresses due to the tire tread deformation in the contact patch determine the overall tire forces. The tire tread deformation in the horizontal direction is determined mainly by tire slip and the position of the tread in the contact patch. Three-dimensional stress distributions will be investigated in the following sections to understand and to model the longitudinal tire force generation phenomenon.

4.1.2.1 Vertical Stress Distribution

Clark [56] measured the distribution of tire vertical stresses, as shown in Figure 4.7, which shows a convex pressure distribution along the motion direction. This convex distribution is formed mainly by tire vertical deformation determined by the shapes of the tire and the contact surfaces. When the tire accelerates or decelerates, tire treads at the leading edge or the trailing edge deform more than the free rolling cases because of the longitudinal forces exerted on the contact patch. The changes of stress distribution due to acceleration and deceleration are quite small compared to the magnitude of stress distribution, thus, they can be ignored.

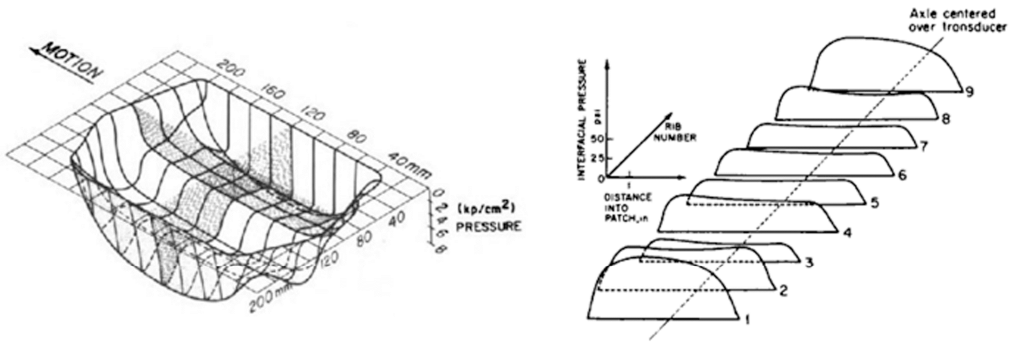

Figure 4.7 Vertical stress distribution across the length of the tire contact patch [56]

Figure 4.8 shows vertical stress distribution along the width of the contact patch. The vertical stress is not evenly distributed along the width because of the tire structure: pressure at the ends of the contact patch is higher than the pressure in the middle. Clark [56] mentioned that higher pressure at the two ends is due to the bending stiffness of the tire carcass.

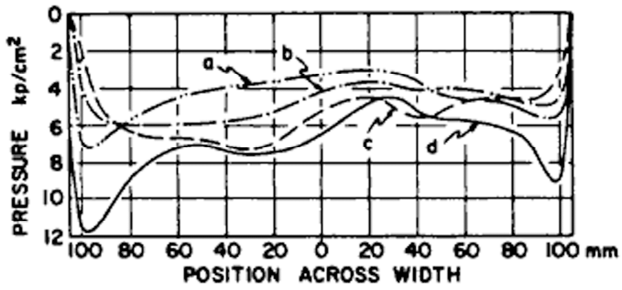

Figure 4.8 Vertical stress distribution across the width of the tire contact patch [56]

4.1.2.2 Horizontal Stress Distribution

Longitudinal stress distribution is significantly affected by acceleration and deceleration. Figure 4.9 shows longitudinal stress distribution of a free rolling tire. Longitudinal stresses exist in the contact patch of a free rolling tire even though no longitudinal force is exerted. Typically, positive stress is generated in the front half of the contact patch and negative stress in the rear half. A diagram explaining this process is shown later in this chapter in Figure 4.13.

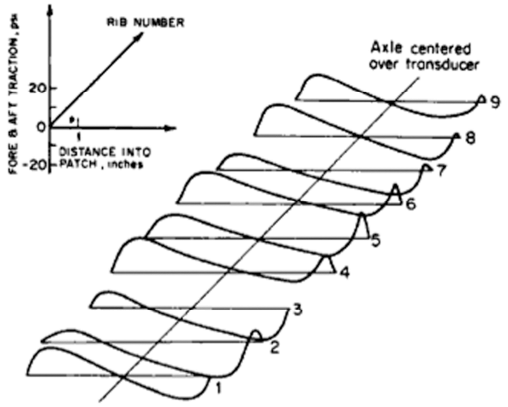

Figure 4.9 Longitudinal stress distribution in the contact patch of a free rolling tire [56]

Figure 4.10 shows the longitudinal stress distribution of a tire when it is under acceleration or deceleration. The magnitude of the stress depends on the position of the tread and the magnitude of the acceleration or deceleration. Generally, in the case of acceleration, the stress increases at locations far away from the leading edge and also as the acceleration increases, whereas, in the case of deceleration, overall behavior is opposite to that of the case of acceleration. Usually the magnitude of stress is believed to linearly increase with the position and acceleration or deceleration until it reaches the friction limit. However, the tire test results in Figure 4.10 show that the longitudinal stress distributions are not linear to the position, which is because the stress existing in a free rolling tire, as shown in Figure 4.9, and the stress due to acceleration or deceleration are combined.

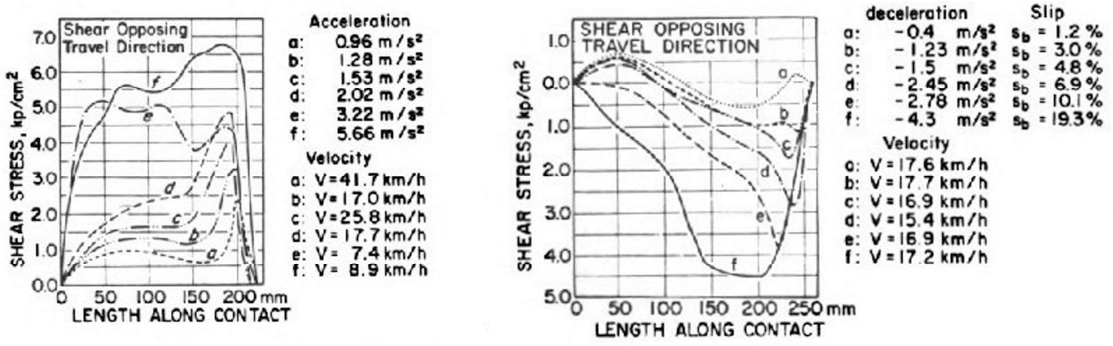

Figure 4.10 Longitudinal stress distribution in the contact patch under acceleration or deceleration [56]

The lateral stress component in the contact patch is very similar to that of the longitudinal case. When a tire rolls freely, the lateral stress distribution due to the lateral geometric deformations is similar to the longitudinal stress distribution caused by longitudinal geometric deformation. But the curvature of the tire along the lateral direction is very small except at the tire shoulders and thus, the lateral stress due to the lateral geometric deformation can be ignored. When lateral slip exists, the stress of a tread depends on the location of the tire tread and the magnitude of the lateral force.

4.1.2.3 Rolling Resistance

Another interesting and important phenomenon is rolling resistance. Rolling resistance of tires on hard surfaces is primarily caused by the hysteresis in tire materials

due to the deflection of the carcass while rolling [57]. Figure 4.11 shows a variation of the rolling resistance coefficient of radial-ply and bias-ply car tires with vehicle forward speed on a smooth and flat road surface. The coefficient of rolling resistance of radial tires is approximately 0.015. This rolling resistance slows down tire rolling or vehicle forward speed if there are no other forces.

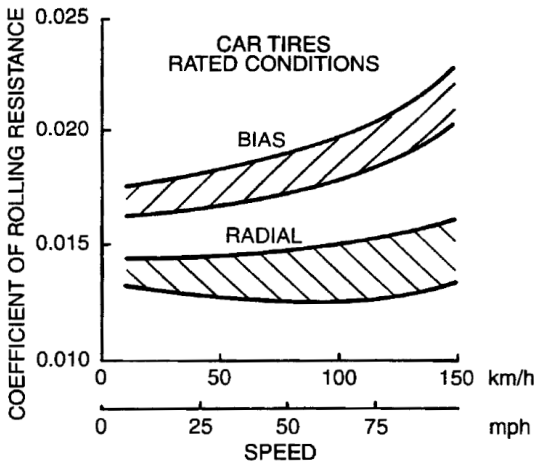

Figure 4.11 Variation of rolling resistance coefficient [57]

4.1.3 Modeling of Stress/Deformation Distribution in the Contact Patch

4.1.3.1 Model of Parabolic Vertical Stress Distribution along the Length

If a tire is modeled as a thin disk with elastic treads, then vertical deformation of tire treads caused by force F_z can be approximated by a parabolic distribution, as shown in Figure 2.6. The vertical stress induced by the vertical deformation is also parabolic for linear stress-strain relations. Since the integration of the vertical stresses along the longitudinal direction should be equal to the vertical force F_z, based on the parabolic stress distribution assumption, the following equation is obtained:

$$\sigma_z(x) = \frac{3F_z}{2l}\frac{x}{l}\left(1-\frac{x}{2l}\right). \tag{4.1}$$

The vertical stress is zero at the leading edge and the trailing edge; it reaches its maximum at the center of the contact patch. Therefore, properties that linearly depend on

vertical forces, such as the friction force limit of the tire tread, will have parabolic distribution.

4.1.3.2 Rolling Resistance Model

Rolling resistance affects vertical stress. The vertical stress distribution caused by the rolling resistance creates a resisting moment against tire rolling. The energy loss due to the deflection of the tire carcass can be modeled as a damping loss due to the tire carcass vertical deformation. If we assume the energy loss is only due to the damping loss and the coefficient of rolling resistance is constant at 0.015, then the following equation for vertical stress can be derived:

$$\begin{aligned}\sigma_{z,damp} &= -c_d \frac{d\delta_z(x)}{dt} \\ &= -c_d \frac{d\delta_z(x)}{dx}\frac{dx}{dt} \\ &= -c_d \frac{d\delta_z(x)}{dx} v \\ &= -c_d v \frac{1}{c_{stiff}} \frac{3F_z}{2l^2}\left(1-\frac{x}{l}\right).\end{aligned} \tag{4.2}$$

where $\delta_z(x)=\sigma_z(x)/ c_{stiff}$, c_{stiff} is the stiffness coefficient, c_d is the damping coefficient, and v is the tire translational speed. To determine the value of c_d, we use the fact that this vertical stress contributes to all the effects of rolling resistance as follows:

$$\begin{aligned}c_{roll} \cdot r \cdot F_z &= \int_0^{2l} \sigma_{z,damp}(x) \cdot (l-x)\, dx \\ &= c_d \int_0^{2l} v \frac{1}{c_{stiff}} \frac{3F_z}{2l^2}\left(1-\frac{x}{l}\right) \cdot (l-x)\, dx,\end{aligned} \tag{4.3}$$

where c_{roll} is the coefficient of rolling resistance.

Figure 4.12 shows vertical stress distributions. The vertical stress due to damping occurs when the tire rolls and the distribution is asymmetric. Therefore, the center of overall vertical force moves forward and creates a resistance moment against the rolling motion.

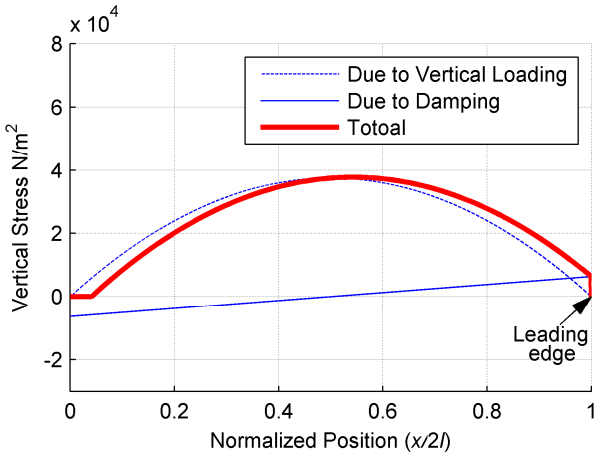

Figure 4.12 Vertical stress distribution due to rolling resistance for a free rolling Brush model

4.1.3.3 Longitudinal Stress Distribution Model

The longitudinal stress of a free rolling tire can be modeled by the Brush model, which is a thin disk with several brushes along the circumference of the disk where the brushes approximates the tire treads. The source of longitudinal stress in a free rolling tire is the velocity difference in the contact patch. Given that assumption that a tire rolls freely on a frictionless surface without slipping, which means that the translational velocity of the tire v is the same as $r_e\omega$, where r_e is the equivalent rolling radius of the tire and ω is the rotational velocity of the tire, then, the treads contacting the road surface have vertical deformation only and no restriction in horizontal movement. Therefore, the relative travel-distance of a tread to the wheel center is determined by the elapsed time t after the tread passes through the leading edge and the rotational velocity of the wheel ω. The contacting points in this case are marked with inverted triangles in Figure 4.13. When there is friction between the tire and the surface, the relative travel-distance is determined by the elapsed time t and the translational velocity of the tire v, because the tread sticks to the road surface due to friction. In this case, the contacting points are marked with small solid circles in Figure 4.13. The inverted triangles and solid circles are not collocated, which means the treads have longitudinal deformations and stresses.

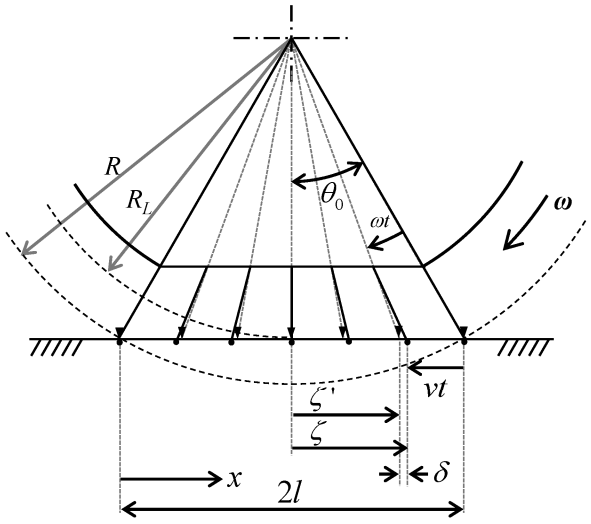

Figure 4.13 Longitudinal tread deformation of a free rolling Brush model

Before moving on to the derivation of the deformation, we will explore how to calculate the equivalent rolling radius of a tire, R_e. The time intervals from the leading edge to the trailing edge along the line of the contact patch and along the wheel circumference should be the same. Thus, the following equations hold:

$$\frac{2l}{v} = \frac{2\theta_0}{\omega} \Leftrightarrow v = \frac{l}{\theta_0}\omega, \qquad \therefore R_e = \frac{l}{\theta_0}, \tag{4.4}$$

where, the equivalent rolling radius r_e is always larger than the loaded tire radius R_L and smaller than the unloaded tire radius R.

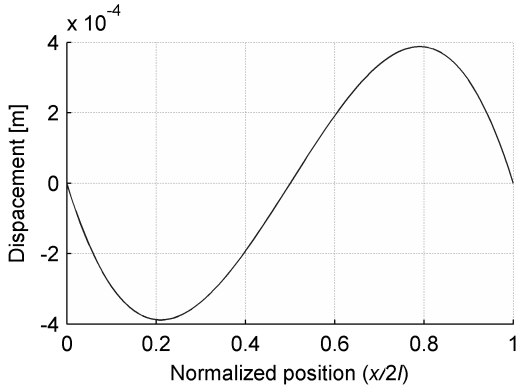

Figure 4.14 Longitudinal tread deformation of a free rolling Brush model tire

The longitudinal deformation due to the velocity difference can be derived as the following equations:

$$\begin{aligned}\delta(x) &= \zeta - \zeta' = \zeta - R_L \tan(\theta_0 - \omega t) \\ &= \zeta - R_L \tan\left(\theta_0 - \omega \frac{l-\zeta}{v}\right) = \zeta - R_L \tan\left(\theta_0 - \frac{l-\zeta}{R_e}\right) \\ &= x - l - R_L \tan\left(\theta_0 - \frac{2l-x}{R_e}\right),\end{aligned} \tag{4.5}$$

where $\theta_0=\cos^{-1}(R_L/R)$. The longitudinal deformation equations are plotted in Figure 4.14, which shows the same pattern as Figure 4.9. Corresponding stress distributions can be achieved by multiplying the deformation equations with the coefficient of the tread stiffness.

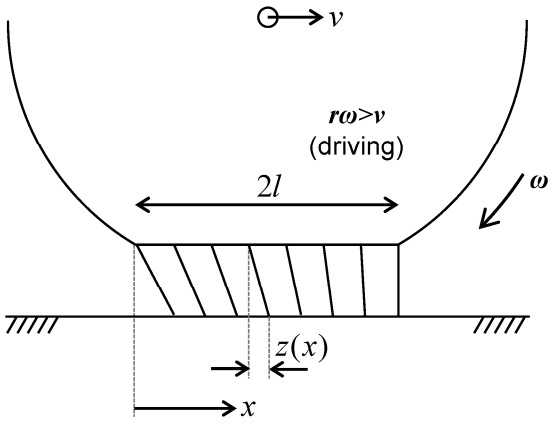

Figure 4.15 Tread deformation distribution under driving condition

When longitudinal slip exists due to acceleration or deceleration, tire deformation increases linearly with the tread-travel distance as shown in Figure 4.15 and the equation for tread deformation is as follows:

$$\begin{aligned}z(x) &= (r\omega - v)\Delta t = (r\omega - v)\frac{2l-x}{rw} \\ &= \kappa(2l-x),\end{aligned} \tag{4.6}$$

where, $\kappa=(r\omega-v)/\, r\omega$ is the slip ratio.

The two sources of longitudinal deformation discussed above are cumulative so that the total deformation is the combined effect of (4.5) and (4.6). However, the total deformation is not simply the summation of the three terms. The total deformation $d_x(x)$ should be saturated by the deformation limit as follows:

$$d_x(x) = \min\left(z(x) + \delta(x),\, d_{\lim}(x)\right),$$
$$d_{\lim}(x) = \frac{\mu}{c_{stiff}} \frac{3F_z}{2l} \frac{x}{l}\left(1 - \frac{x}{2l}\right). \tag{4.7}$$

The deformation limit $d_{\lim}(x)$ is determined by the friction coefficient, the stiffness coefficient, and the vertical stress, ignoring the rolling resistance in this case. An example of the deformation distribution is shown in Figure 4.16, where the slip ratio is 0.2 and the friction coefficient is 0.5.

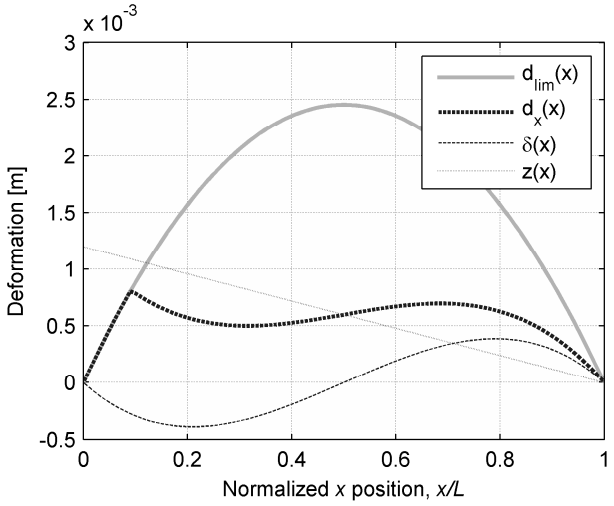

Figure 4.16 Longitudinal deformation of the tire tread using the Brush model under non-zero slip

4.1.4 Factors Affecting Longitudinal Force Generation

The tire longitudinal force model introduced in Chapter 2.2 is not consistent with the test results for small slip. This might be because the original Brush model ignores the phenomena discussed in section 4.1.2. In this chapter, we will see how the phenomena affect the longitudinal force curves.

4.1.4.1 Effect of Rolling Resistance

The first factor we did not consider in the original Brush model is rolling resistance. The vertical stress consists of the stresses due to the rolling resistance caused by vertical deformation and damping. The equations of the Brush model with rolling resistance are as follows:

$$\begin{aligned} F_x(\kappa) &= \int_0^{2l} \sigma_x(\kappa, x)dx, \\ \sigma_x(\kappa, x) &= \min\left(c_p e_x(\kappa, x),\ \mu\sigma_z(x)\right), \end{aligned} \tag{4.8}$$

where

$$e_x(\kappa, x) = (2l - x)\kappa, \qquad \sigma_z(x) = \sigma_{z,load}(x) + \sigma_{z,damping}(x),$$

$$\sigma_{x,load}(x) = \frac{3F_z}{2l}\frac{x}{l}\left(1 - \frac{x}{2l}\right), \qquad \sigma_{x,load}(x) = -c_d v \frac{1}{c_{stiff}}\frac{3F_z}{2l^2}\left(1 - \frac{x}{l}\right).$$

The effect of rolling resistance is shown in Figure 4.17, where longitudinal force curves move downward due to the longitudinal resistance. The rolling resistance reduces the longitudinal forces but does not significantly change the initial gradients of force curves at small slip ratios, as observed in experimental results.

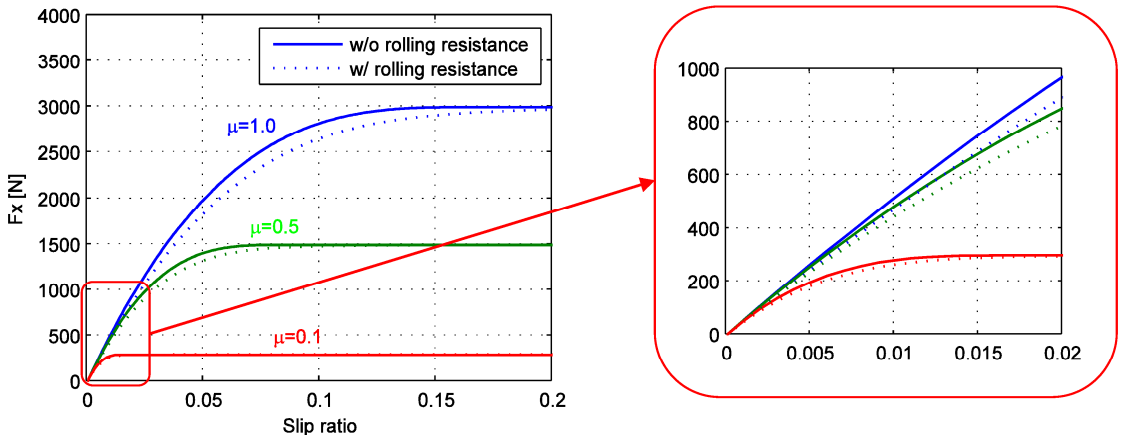

Figure 4.17 Effect of rolling resistance on longitudinal force of the Brush model

4.1.4.2 Effect of Stress Existing in a Free Rolling Tire

The second factor ignored in the original Brush model is the stresses due to the longitudinal deformation caused by local velocity differences in a free rolling tire, as shown in Figure 4.9 and Figure 4.16. The force curves can be computed using (4.8) with the following strain and normal stress distribution.

$$\begin{aligned} e_x(\kappa, x) &= (2l - x)\kappa + \delta(x), \\ \sigma_z(x) &= \frac{3F_z}{2l}\frac{x}{l}\left(1 - \frac{x}{2k}\right), \end{aligned} \tag{4.9}$$

where $\delta(x)$ is derived in (4.5) and the rolling resistance effect is ignored in this case. The longitudinal force curves with the internal stress are shown in Figure 4.18, which compares the force curve plots with and without internal stress. The stress existing in a free rolling tire results in force curves that are more separated in the small slip ratio region. This is because the stress existing in a free rolling tire reduces the overall stress at part of the contact patch. The force curves in the negative slip region are more separated than in the positive slip region, because of the asymmetric distribution of the stress existing in a free rolling tire.

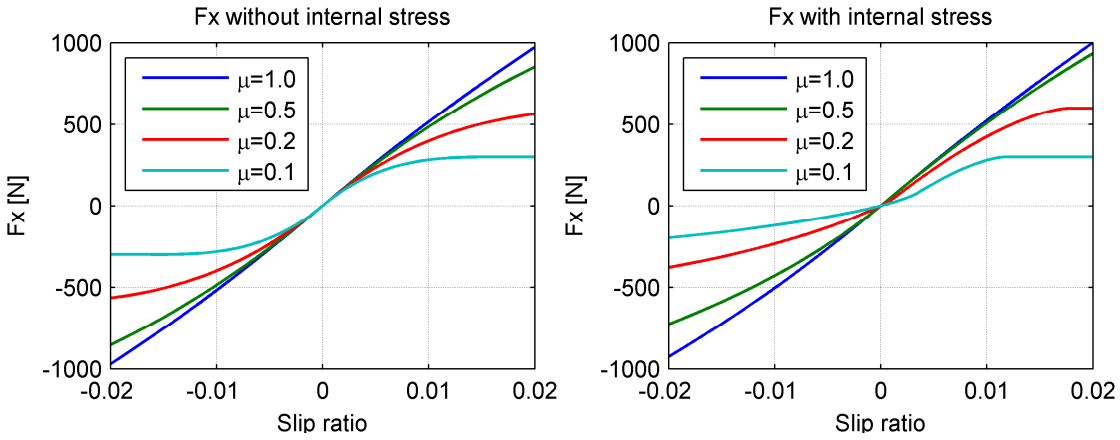

Figure 4.18 Effect of longitudinal internal stress on the Brush model

Figure 4.19 and Figure 4.20 show examples of stress distribution in the contact patch, where the friction coefficient is fixed at 0.15 for both cases, and the slip ratios are 0.01 and –0.01, respectively. The left plots are the stress distribution when the stress

existing in a free rolling tire is ignored, i.e. the original Brush model. The right plots are the stress distribution when the stress existing in a free rolling tire is considered. The representation of llongitudinal force can be achieved by integrating the red dot lines along the contact patch. The stress level increases due to the internal stress at the front half of the contact patch, but it decreases in the rear half of the contact patch, which results in a smaller longitudinal force than that of the original Brush model in the negative slip case. In the positive slip case, reduction in longitudinal force happens only in the small slip range and on low friction surfaces. Therefore, the force curves are not symmetrical when internal stress is considered.

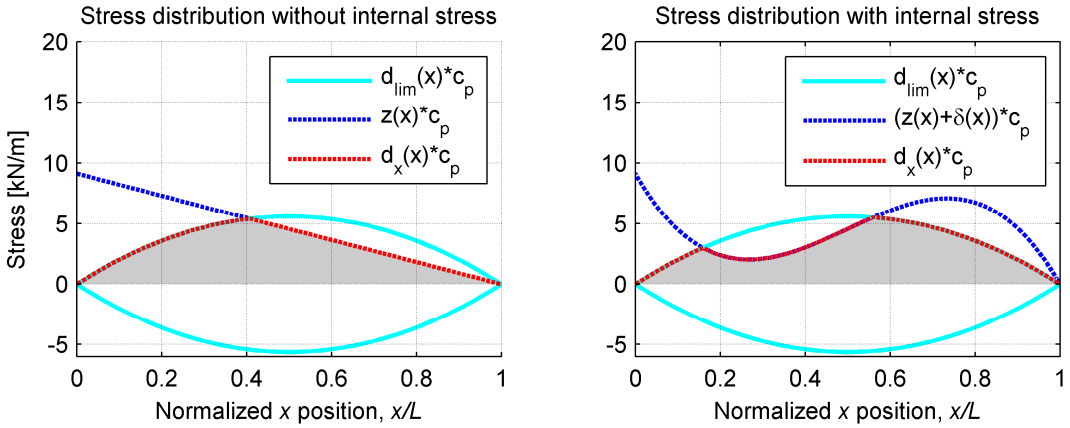

Figure 4.19 Stress distribution in contact patch at positive slip ratio 0.01

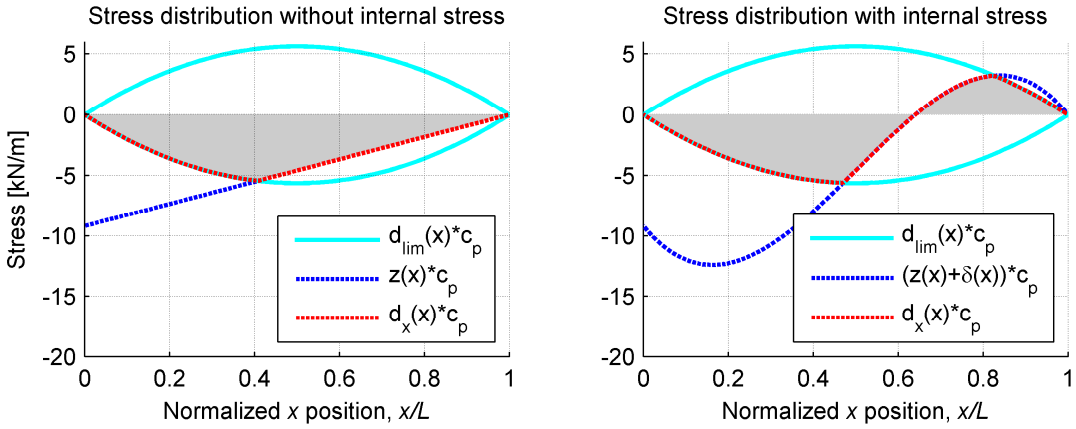

Figure 4.20 Stress distribution in the contact patch under negative slip ratio -0.01

4.1.4.3 Effect of Equivalent Tire-Road Surface Stiffness

Another possible factor for friction-sensitive longitudinal stiffness is the existence of soft material between the tire and the road surface. Deur [49] pointed out that snow or wet ice may reduce tire-road stiffness. He introduced an equivalent tire-road stiffness model that is a function of the friction coefficient and illustrated the influence of equivalent tire-road stiffness in longitudinal tire force generation, as shown in Figure 4.21. The effect of this equivalent stiffness concept can explain friction-level-dependent longitudinal force generation on snow and wet ice surfaces; however, it is not clear that the property and amount of the soft material are independent of the friction coefficient of the surface. This concept can explain the different tire longitudinal stiffness on different surfaces without bringing additional parameters, but the existence of soft material between a tire and a road results in a more complex friction model that has multiple parameters, and, therefore, may not be good for friction estimation.

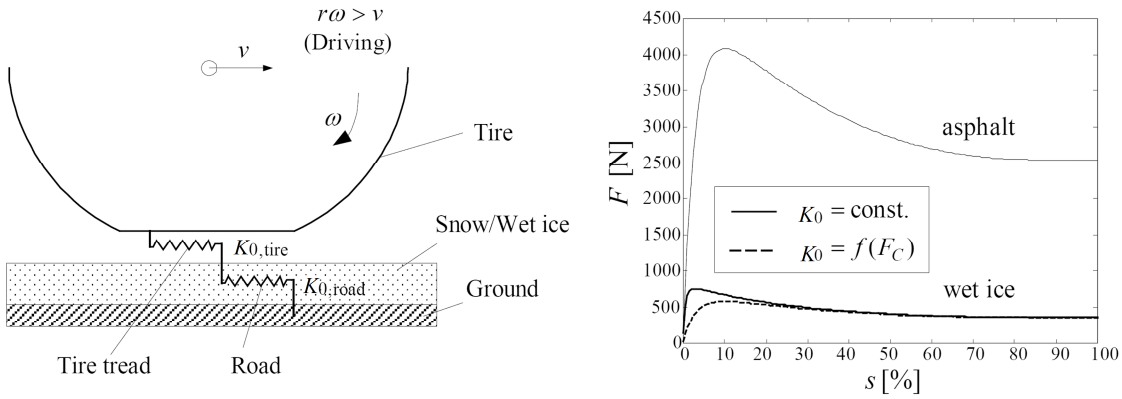

Figure 4.21 Longitudinal tire force for small-slip range and different road conditions as envisioned in the " equivalent tire-road stiffness" concept [49]

4.2 Estimation of Friction Coefficient in the Linear Range (0-2%)

4.2.1 Algorithm

4.2.1.1 Model for Tire Longitudinal Force in the Linear Range

The longitudinal force distribution extracted from our test result is plotted in Figure 4.22. In the small-slip range, the longitudinal force increases proportional to the

slip and the gradient of the force-slip curve is defined as the longitudinal force stiffness. Thus, the longitudinal force model in the small-slip range can be expressed as follows:

$$F_x(\kappa) = k(\mu)\cdot\kappa,\ for\ |\kappa| < 0.02, \tag{4.10}$$

The longitudinal stiffness $k(\mu)$ changes as friction level μ changes and is also dependent on the tire characteristic. The friction coefficients and longitudinal stiffness between a tire (Pirelli 255/50R-17 installed on the Jaguar S-type test vehicle used in this study) and three surfaces are listed in Table 4.1.

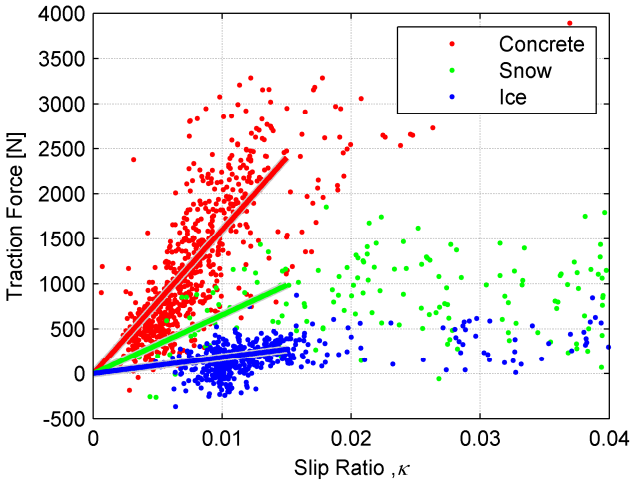

Figure 4.22 Longitudinal tire force in the small-slip region under different road conditions

Generally, the friction coefficient and longitudinal stiffness have a positive correlation and the relationship can be simplified as a curve obtained through interpolation of Table 4.1.

Table 4.1 Friction coefficient and longitudinal stiffness of our test tire on several surfaces

Surfaces	Friction Coefficient	Longitudinal Stiffness
Concrete	0.85~1.0	16.0×10^4
Snow	0.35~0.4	6.6×10^4
Ice	0.15~2	1.8×10^4

4.2.1.2 Recursive Least Squares (RLS)

The equation (4.10) can be rewritten into a standard parameter identification form as follows:

$$y(t) = \varphi^T(t)\theta(t), \tag{4.11}$$

where $y(t)=F_x$ is the system output, $\theta(t)=k(\mu)$, is the unknown parameter, and $\varphi(t)=\kappa$ is the measured slip ratio. The unknown parameter $\theta(t)$ can be identified in real-time using parameter identification approach. Once the stiffness $k(\mu)$ is identified, the friction coefficient μ can be classified using Table 4.1.

The recursive least squares algorithm [58] provides a method to iteratively update the unknown parameter at each sampling time to minimize the sum of the squares of the modeling error using the past data contained within the regression vector, $\varphi(t)$. The procedures for solving the RLS problem is as follows:

Step 0: Initialize the unknown parameter $\theta(0)$ and the covariance matrix $P(0)$; set the forgetting factor λ.

Step 1: Measure the system output $y(t)$ and compute the regression vector $\varphi(t)$.

Step 2: Calculate the identification error $e(t)$:

$$e(t) = y(t) - \varphi^T(t)\theta(t-1). \tag{4.12}$$

Step 3: Calculate the gain $K(t)$:

$$K(t) = P(t-1)\varphi(t)\left[\lambda + \varphi(t)^T P(t-1)\varphi(t)\right]^{-1}. \tag{4.13}$$

Step 4: Calculate the covariance matrix:

$$P(t) = \left(I - K(t)\varphi^T(t)\right)\lambda^{-1}P(t-1). \tag{4.14}$$

Step 5: Update the unknown parameter:

(4.15)

$$\theta(t) = \theta(t-1) + K(t)e(t).$$

Step 6: Repeat Steps 1~5 for each time step.

4.2.1.3 Stiffness Identification and Friction Coefficient Estimation

We derived an equation for vehicle longitudinal motion in (2.8). If we assume the road inclination angle is given for a rear-wheel-drive car, the standard form of parameter identification can be derived using the following equation.

$$ma_x + mg\sin\Theta + R_{xf} + R_{xr} + D_A = F_{x,rl} + F_{x,rr}, \tag{4.16}$$

where m is the vehicle weight, and a_x is the vehicle longitudinal acceleration. Using the linear tire force model shown in (4.10), (4.16) can be rewritten as follows:

$$a_x + g\sin\Theta + \frac{R_{xf} + R_{xr} + D_A}{m} = \frac{\kappa_{rl} + \kappa_{rr}}{m} K(\mu). \tag{4.17}$$

Each term on the left hand side can be measured, calculated, and predetermined. Then, we can identify the stiffness $K(\mu)$ if we configure the problem as follows:

$$\begin{aligned} y(t) &= a_x + g\sin\Theta + \frac{R_{xf} + R_{xr} + D_A}{m}, \\ \varphi(t) &= \frac{\kappa_{rl} + \kappa_{rr}}{m}, \\ \theta(t) &= K(\mu). \end{aligned} \tag{4.18}$$

The corresponding friction coefficient is calculated using a mapping function from the stiffness to the friction coefficient as shown in Table 4.1.

4.2.2 Simulations

The algorithm is evaluated with simulation where the road surface is designed to have sudden friction coefficient changes, a so called mu-jump surface and the vehicle maneuver is straight driving with intermittent gas pedal presses. The road surface condition and vehicle states are plotted in Figure 4.23. The estimated result is shown in

Figure 4.24 where the algorithm is activated only when longitudinal slip exists. Comparing the slip ratio in Figure 4.23 to the activation signal in Figure 4.24, the time duration of estimation is relatively smaller on the low friction surface than on the high friction surface. This is because the slip ratio quickly increases on slippery surfaces. The estimator encounters two sudden surface changes at 5 seconds and at 11.5 seconds. The estimator shows delayed estimation at the first change due to lack of excitation at that time. Once excitation occurs at 5.5 seconds, the estimator updates the friction coefficient. At the time of the second surface change, the excitation duration is coincident with the change so that the estimated friction coefficient tracks the actual value immediately. However, this algorithm does not provide slip angle estimation and the accuracy of estimation will deteriorate if combined slip exists.

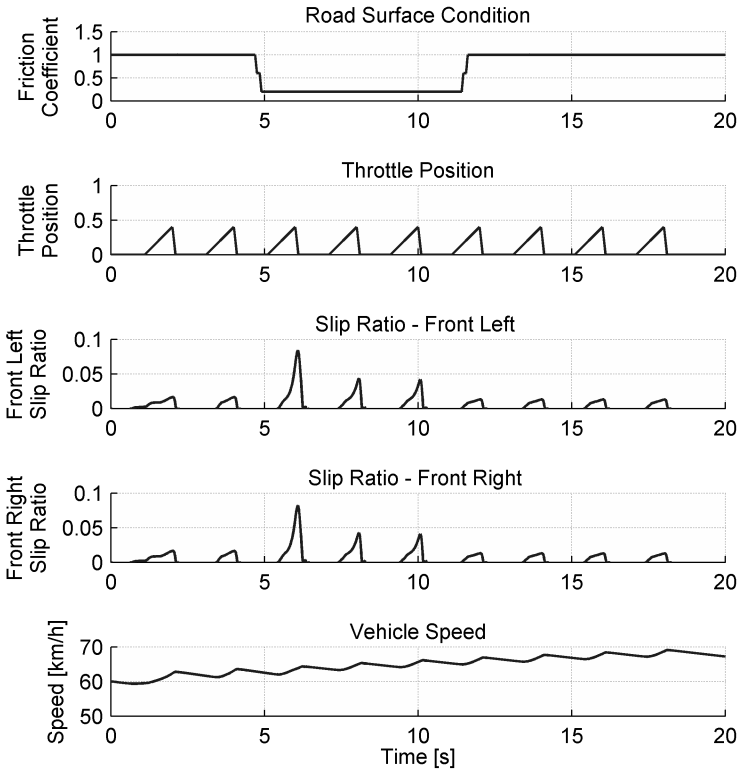

Figure 4.23 Road surface condition and the vehicle states of the simulation to evaluate the small longitudinal slip based algorithm

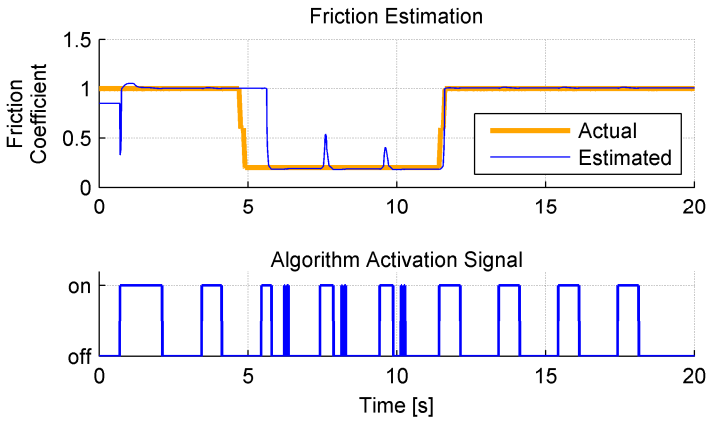

Figure 4.24 Friction estimation result and corresponding activation signal when the small longitudinal slip based algorithm is used

4.3 Estimation of Friction Coefficient in the Saturation Range (30~100%)

4.3.1 Algorithm

The friction estimation algorithm based on tire stiffness identification does not work if a wheel is spinning because the estimation algorithm using tire stiffness is valid only at a linear range. When a wheel is spinning, the tire longitudinal force saturates and it becomes insensitive to the slip ratio and wheel speed. The tire longitudinal force is dependent on the friction coefficient and the tire vertical force when the wheel is spinning, as shown in Figure 4.3 and Figure 4.4, which situation results in a simple longitudinal tire force model, as shown in (2.11). If the wheel is spinning, $|\kappa|>\kappa_{sl}$, the longitudinal force can be easily determined using the friction coefficient and the normal tire, as follows:

$$f_x(\kappa,\ \mu) = \mu F_z \cdot sign(\kappa). \tag{4.19}$$

When a car is experiencing acceleration close to the friction limit, the driving tires are saturated, which provides information about the friction level. For the rear-wheel-drive vehicle shown in Figure 4.25, the traction force is computed from:

$$F_{xr} = \mu F_{zr} = \mu \frac{a}{a+b} mg. \tag{4.20}$$

Therefore, the friction coefficient is easily computed as follows

$$\mu = \frac{a+b}{a}\left(\frac{a_x}{g} + \sin\Theta + \frac{R_{xf} + R_{xr} + D_A}{mg}\right) \tag{4.21}$$

Even though we can calculate the friction coefficient directly from the longitudinal acceleration, we use RLS for a smoother estimation as follows:

$$\frac{a+b}{a}\left(\frac{a_x}{g} + \sin\Theta + \frac{R_{xf} + R_{xr} + D_A}{mg}\right) = 1 \cdot \mu. \tag{4.22}$$

By comparing (4.11) and (4.22), we can configure a RLS problem as follows:

$$\begin{aligned} y(t) &= \frac{a+b}{a}\left(\frac{a_x}{g} + \sin\Theta + \frac{R_{xf} + R_{xr} + D_A}{mg}\right), \\ \varphi(t) &= 1, \\ \theta(t) &= \mu. \end{aligned} \tag{4.23}$$

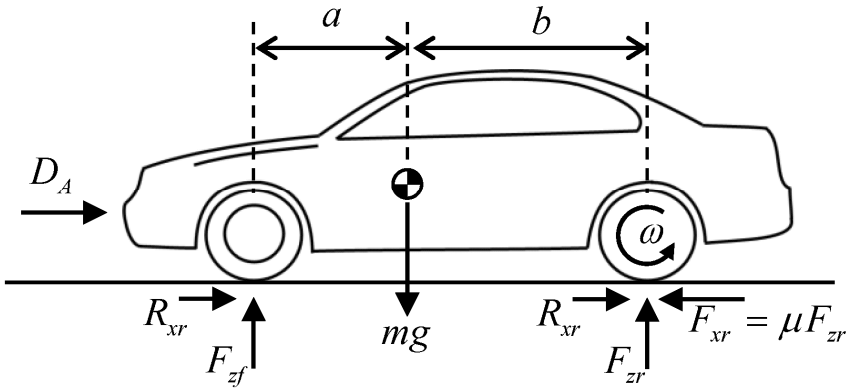

Figure 4.25 Force distribution when the rear wheels are spinning; the traction force is independent of slip ratio and a function of the friction coefficient and the normal force.

This estimation algorithm is valid only when the slip ratio is higher than 30%. In the case where only one driving wheel is spinning, (4.20) still holds because the differential of the drive train keeps the torques of both driving wheels equal. Therefore, this estimation algorithm is still applicable when only one driving wheel is spinning.

4.3.2 Simulations

The evaluation of the algorithm is performed with the same conditions used for the small slip based algorithm except for excitation level. The throttle input is increased to generate a large slip ratio as shown in Figure 4.26. The slip ratio on the low friction surface increases up to 0.5, which is in the saturation range, thereby activating the large slip based algorithm.

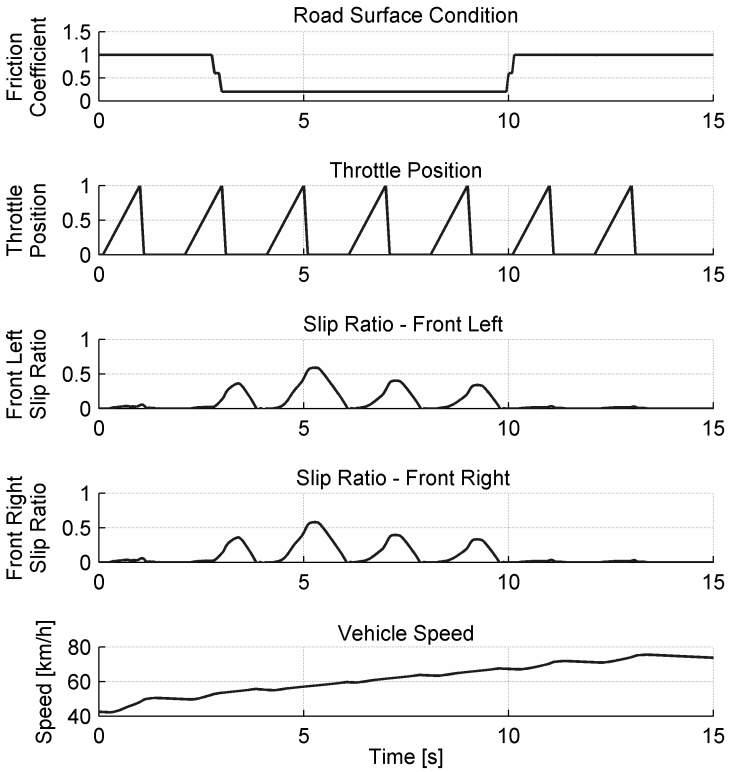

Figure 4.26 Road surface condition and the vehicle states of the simulation to evaluate the large longitudinal slip based algorithm

Figure 4.27 shows the estimation result. As the estimation algorithm is activated only for large slip cases, the estimated friction coefficient is updated only on slippery surfaces. During the time intervals of 0~2.5 seconds and 10~15 seconds, no update occurs even if the gas pedal of the vehicle is pressed several times because the resulting slip is small. These small excitation cases can be dealt with by using the small longitudinal slip based algorithm.

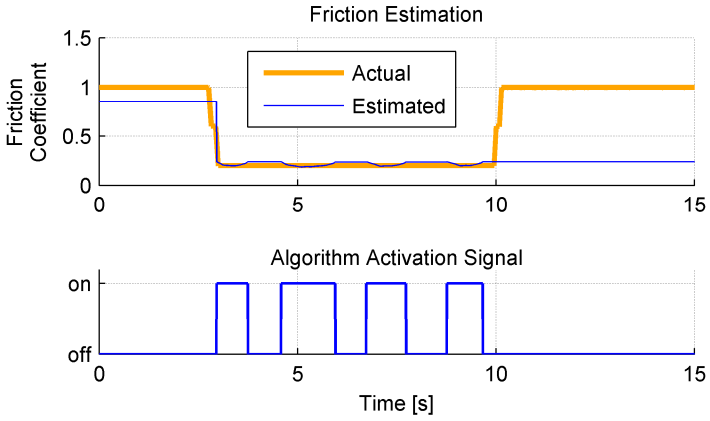

Figure 4.27 Friction estimation result and corresponding activation signal when the large longitudinal slip based algorithm is used

To use both small and large excitations, we applied both of the longitudinal slip based algorithms for the simulation data and the estimation results are shown in Figure 4.28. We have more chances to update the friction coefficient by using two algorithms and, therefore, the friction estimation is available in the time period 0~2.5 seconds and 10~15 seconds, which was previously noted to be the time period that the estimation is not available with the large longitudinal slip based algorithm. It is worthwhile to note that integrating the estimators that require different excitation conditions improves the estimation quality. Therefore, the integration of all the proposed algorithms – the lateral excitation based algorithms and the longitudinal excitation based algorithms – will be discussed in the next chapter.

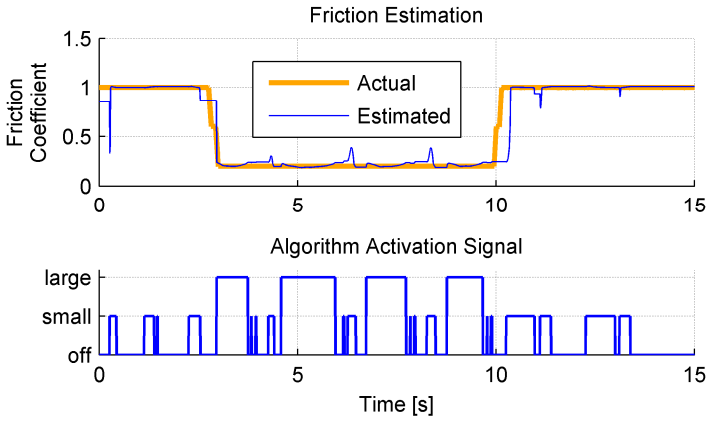

Figure 4.28 Friction estimation result and corresponding activation signal when both of the small and the large longitudinal slip based algorithms are used

4.4 Summary

There are two reasons why longitudinal dynamics friction estimation is important; availability of required sensors, and the fact that vehicles frequently operate in regions with only longitudinal excitations. We divide the longitudinal slip range into three ranges: the linear range, the transient range and the saturation ranges. The tire force generation shows simple relations between the tire slip ratio and tire normal force and friction coefficient in the linear and saturation ranges. However, in the transient range, the tire force generation is affected by many factors so that the nonlinear models having a single parameter are not valid when the factors are uncertain. We developed two algorithms for the linear and the saturation ranges using simple force generation equations. In the case of the transient range, we assume ABS/TCS systems can provide friction coefficient information estimated using internal signals of the systems.

For the linear range case, the algorithm is based on the observation that longitudinal tire stiffness is dependent on the friction coefficient, which is not explained well by physics based tire models such as the Brush model. The phenomena in the tire contact patch are explored to explain the friction coefficient dependent longitudinal tire stiffness and it is found that the stress existing in a free rolling tire can explain such property of tire stiffness. For the saturation range case, the algorithm is based on the fact that the generated longitudinal force is insensitive to the slip ratio and only dependent on the friction coefficient and normal force.

These algorithms work well only for pure longitudinal excitation. Accuracy is not guaranteed when lateral excitation coexists with longitudinal excitation. In this case, the friction coefficient can be estimated by a lateral dynamics based method, which will be described in the next chapter.

CHAPTER 5
INTEGRATED FRICTION ESTIMATION ALGORITHM

The algorithms presented in CHAPTER 3 and CHAPTER 4 were developed based on certain assumptions of the type/level of excitations. These assumptions need to be kept in mind because the algorithms are likely to behave satisfactorily only under these excitations. For example, the maximum aligning moment method is based on the assumption that large lateral excitations exist, and the nonlinear observer is based on medium lateral excitations, whereas, the longitudinal dynamics based method requires less than about 2% of longitudinal slip for the linear range method and 30%~100% of longitudinal slip for the saturation range method.

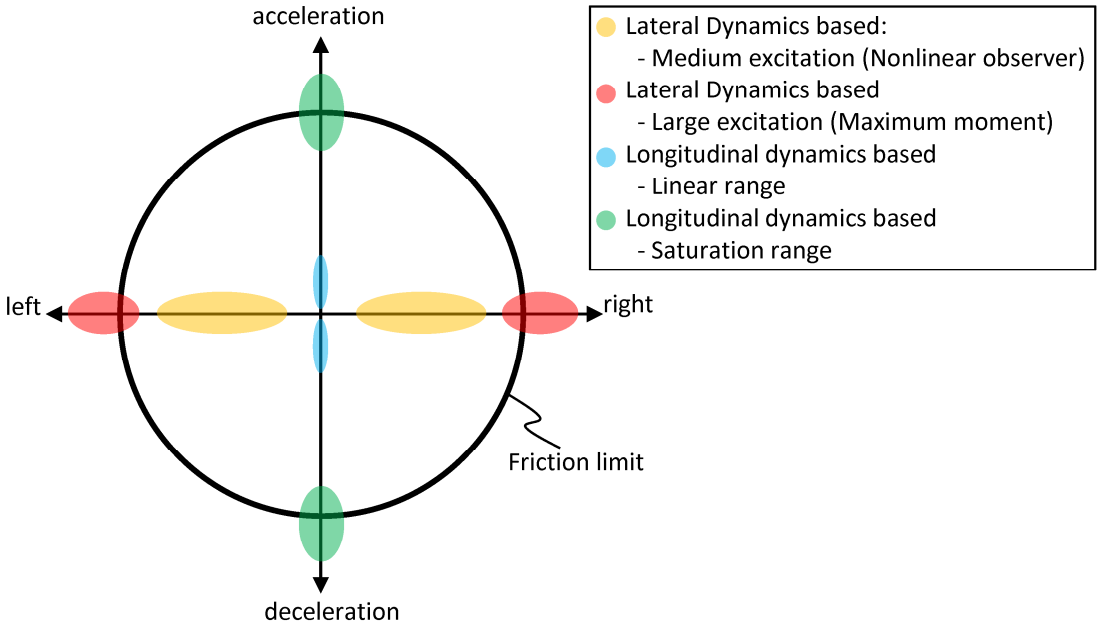

Figure 5.1 Coverage of the presented estimation methods in the friction circle

In Figure 5.1, the two longitudinal excitation based methods cover only a small range of pure longitudinal excitations, whereas, the two lateral excitation based methods cover almost all of the range of pure lateral excitations except around zero excitation and

just below the maximum excitation. However, all four methods were developed based on the pure-slip assumption and might not handle combined slip cases well. Therefore, in this chapter, we are going to discuss ways to increase the coverage, mainly by switching between different estimators.

5.1 Increasing Coverage of the Lateral Dynamics Based Methods

The nonlinear observer derived in (3.38) uses a Brush model and assumes pure lateral slip. Therefore, if the vehicle is cornering and accelerating/decelerating at the same time, the estimation algorithm might not produce an accurate road friction estimate. Furthermore, asymmetric longitudinal force distribution on the left and right tires causes an additional yaw moment. In this case, the observer performance will degrade, or even worse, the estimation output might diverge, as shown in Figure 5.2, where large (about 30%) longitudinal slip (at around 6 second) causes observer instability.

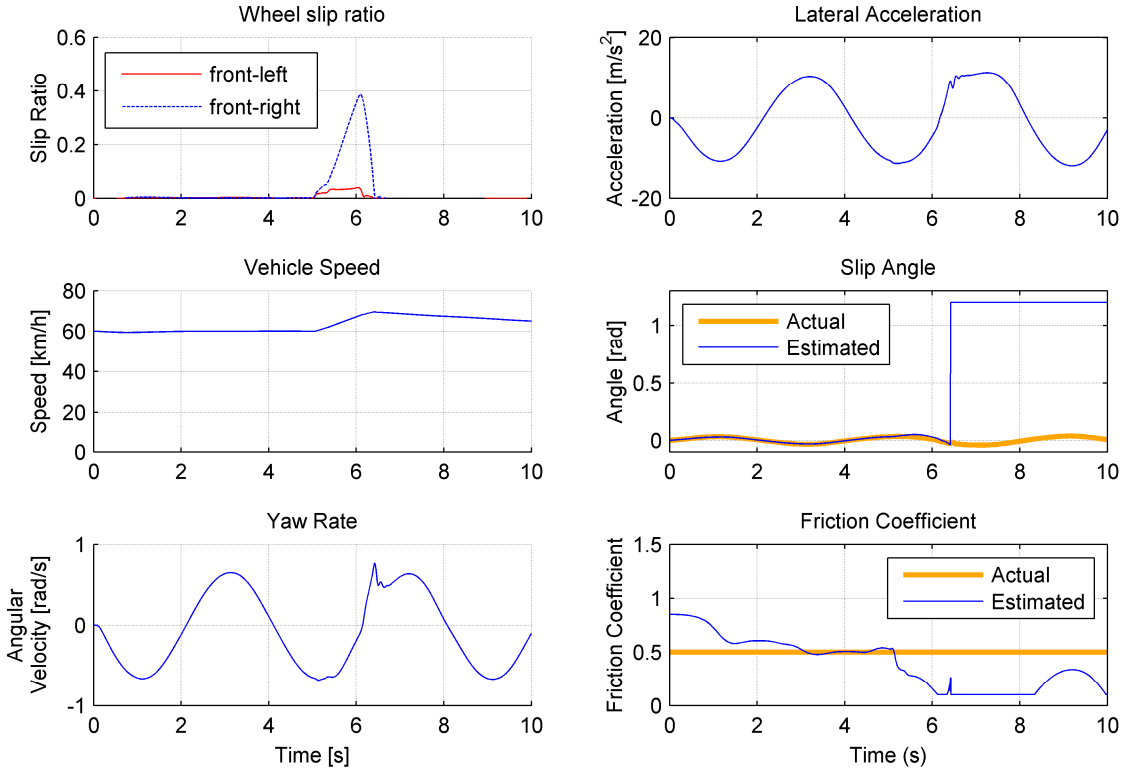

Figure 5.2 Performance of the lateral dynamics based method in a combined slip simulation

To avoid this problem, we have to use a Brush model for combined slip cases and a four-wheel vehicle model. A Brush model for combined slip is derived in (2.14) and a four wheel vehicle model is shown in Figure 5.3 and the corresponding vehicle dynamics are as follows:

$$\begin{aligned} m\left(\dot{v}_y + v_x r\right) &= F_{yf} + F_{yr}, \\ I_z \dot{r} &= aF_{yf} - bF_{yr} + \frac{w}{2}F_{xr} - \frac{w}{2}F_{xl}. \end{aligned} \tag{5.1}$$

Note that there are two new terms from longitudinal forces in the moment balance equation.

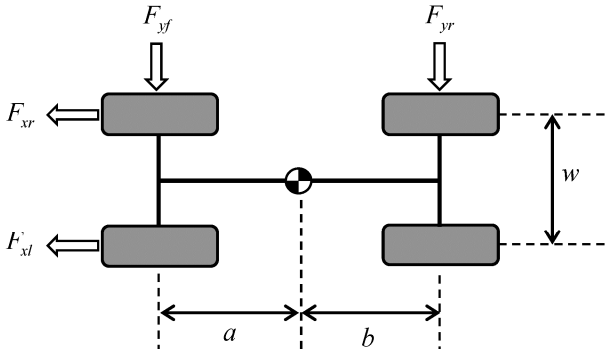

Figure 5.3 Four wheel bicycle model

Based on the four-wheel bicycle model, the new observer equations are:

$$\begin{aligned} \dot{\hat{\alpha}}_f &= \left(\frac{1}{mv_x} + \frac{a^2}{I_z v_x}\right)\hat{F}_{yf} + \left(\frac{1}{mv_x} - \frac{ab}{I_z v_x}\right)\hat{F}_{yr} + \frac{w}{2I_z V_x}(\hat{F}_{xr} - \hat{F}_{xl}) - r - \dot{\delta} \\ &\quad + l_1\left(ma_y - \left(\hat{F}_{yf} + \hat{F}_{yr}\right)\right) + l_2\left(\tau_a - \hat{\tau}_a\right), \\ \dot{\hat{\mu}} &= l_3\left(ma_y - \left(\hat{F}_{yf} + \hat{F}_{yr}\right)\right) + l_4\left(\tau_a - \hat{\tau}_a\right), \end{aligned} \tag{5.2}$$

where $\hat{F}_{yf}$ and $\hat{F}_{yr}$ are calculated by the combined slip Brush model (2.14) using the estimated slip angle and measured slip ratio.

The estimation results with observer (5.2) are shown in Figure 5.4, where the observer does not diverge as before, but it is not as accurate. There are several reasons for this. One reason is the un-modeled compliance steering effect due to the longitudinal and

lateral tire forces; another is the significant mismatch between the Brush model used for the observer and the Magic Formula model used for the vehicle simulations, especially when the longitudinal slip is large. We can compensate for the compliance steering effect by modeling it, but the tire model mismatch cannot be captured—and in fact the Magic Formula would not be the "truth" in field testing anyway, especially under large tire slips. So tire mismatch always exists and robustness against it must be tested.

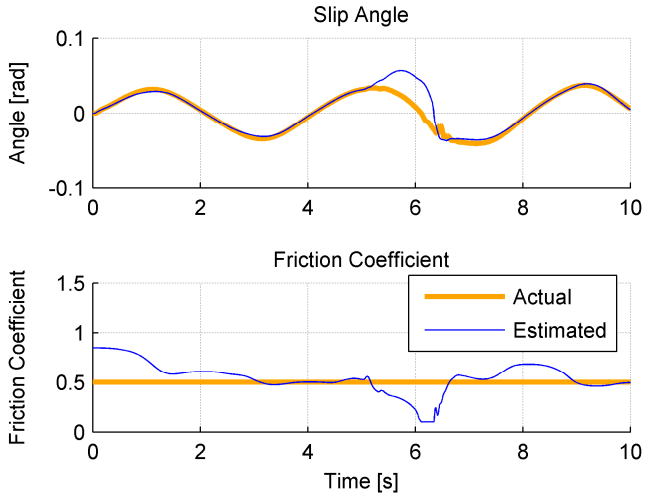

Figure 5.4 Improved observer performance by including combined slip in the observer design

Because model mismatch is unavoidable, we choose to improve the observer performance by reducing the effect of model mismatch, rather than trying to reduce the model mismatch itself. One way to reduce the effect of model mismatch is to reduce the magnitude of the observer gains driven only by measurement error feedback because the state estimation is driven by its own dynamics and measurement feedback. The observer with adaptive gains to longitudinal slip is as follows:

$$\begin{aligned}\dot{\hat{\alpha}}_f &= \left(\frac{1}{mv_x}+\frac{a^2}{I_z v_x}\right)\hat{F}_{yf}+\left(\frac{1}{mv_x}-\frac{ab}{I_z v_x}\right)\hat{F}_{yr}+\frac{w}{2I_z V_x}(\hat{F}_{xr}-\hat{F}_{xl})-r-\dot{\delta}\\ &\quad +l_1\left(ma_y-\left(\hat{F}_{yf}+\hat{F}_{yr}\right)\right)+l_2\left(\tau_a-\hat{\tau}_a\right),\\ \dot{\hat{\mu}} &= k_{slip}\cdot l_3\left(ma_y-\left(\hat{F}_{yf}+\hat{F}_{yr}\right)\right)+k_{slip}\cdot l_4\left(\tau_a-\hat{\tau}_a\right),\end{aligned} \tag{5.3}$$

where k_{slip} is the gain reduction parameter. Because the measurement model consists of the tire model, by reducing the observer gain magnitude, we can reduce the effect of tire model error in the measurement.

The gain reduction is adaptive to the magnitude of slip ratio and the level of reduction can be tuned heuristically. An example of the gain reduction function is shown in Figure 5.5, in which case the observer gains of (5.3) are reduced to almost zero when the slip ratio is larger than 5%. This gain reduction function results in open loop estimation for the friction coefficient when model uncertainty is high. Therefore this method is only valid under the assumption that the current estimate of the friction coefficient is close to the true value.

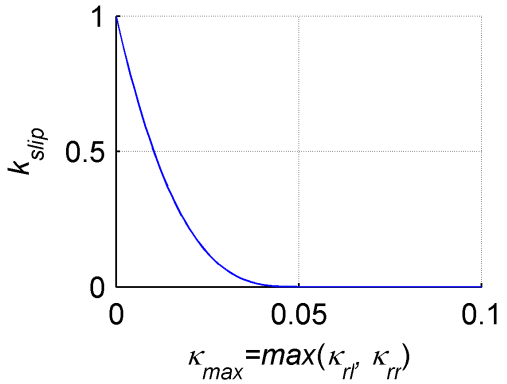

Figure 5.5 The proposed gain reduction function

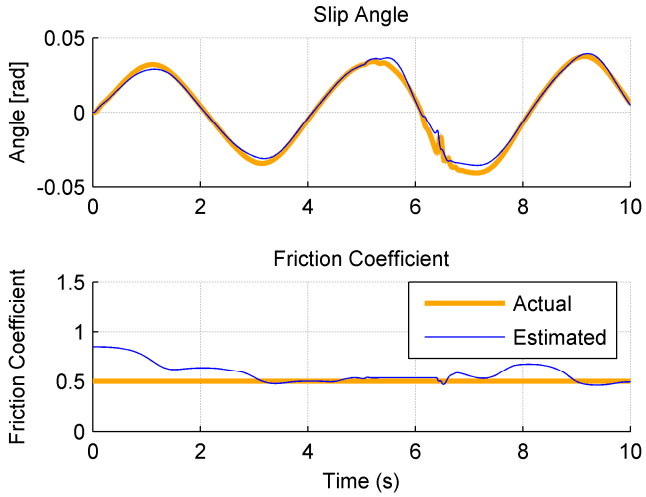

Figure 5.6 Estimation result of the observer with the gain reduction function

The method using the combined slip tire model increases the coverage of the lateral dynamics based method, as shown in Figure 5.7. In the yellow area, not covered by any of the algorithms we proposed, an open loop observer is used and the equations are as follows:

$$\dot{\hat{\alpha}}_f = \left(\frac{1}{mv_x} + \frac{a^2}{I_z v_x}\right)\hat{F}_{yf} + \left(\frac{1}{mv_x} - \frac{ab}{I_z v_x}\right)\hat{F}_{yr} + \frac{w}{2I_z V_x}(\hat{F}_{xr} - \hat{F}_{xl}) - r - \dot{\delta},$$
$$\dot{\hat{\mu}} = 0, \tag{5.4}$$

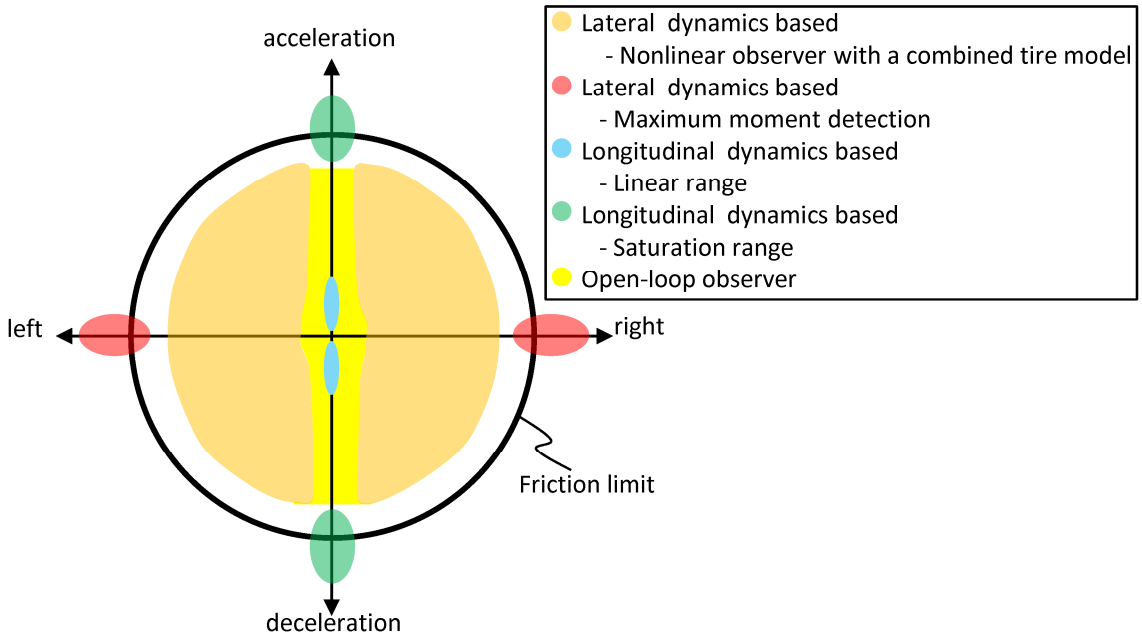

Figure 5.7 Increased coverage of the estimators by using the combined slip tire model

The equations for estimators are summarized in Table 5.1. The nonlinear observer for medium lateral excitation is modified to cover combined slip excitation and the open loop observer is used to fill the gap between the coverage of the estimators. The remaining step for utilizing the four approaches is to define a logic to switch between estimators, which is discussed in Chapter 5.2.

Table 5.1 Comparison of the friction coefficient estimators for different excitation conditions

Excitation	Estimator for pure excitation	Estimators for integration	Remarks
Medium lateral excitation	$\dot{\hat{\alpha}}_f = \left(\frac{1}{mv_x} + \frac{a^2}{I_z v_x}\right)\hat{F}_{yf} + \left(\frac{1}{mv_x} - \frac{ab}{I_z v_x}\right)\hat{F}_{yr} - r - \dot{\delta} + l_1\left(ma_y - \left(\hat{F}_{yf} + \hat{F}_{yr}\right)\right) + l_2\left(\tau_a - \hat{\tau}_a\right),$ $\dot{\hat{\mu}} = l_3\left(ma_y - \left(\hat{F}_{yf} + \hat{F}_{yr}\right)\right) + l_4\left(\tau_a - \hat{\tau}_a\right).$	$\dot{\hat{\alpha}}_f = \left(\frac{1}{mv_x} + \frac{a^2}{I_z v_x}\right)\hat{F}_{yf} + \left(\frac{1}{mv_x} - \frac{ab}{I_z v_x}\right)\hat{F}_{yr} - r - \dot{\delta} + l_1\left(ma_y - \left(\hat{F}_{yf} + \hat{F}_{yr}\right)\right) + l_2\left(\tau_a - \hat{\tau}_a\right),$ $\dot{\hat{\mu}} = k_{slip} \cdot l_3\left(ma_y - \left(\hat{F}_{yf} + \hat{F}_{yr}\right)\right) + k_{slip} \cdot l_4\left(\tau_a - \hat{\tau}_a\right).$	A combined tire model and a gain reduction function are used for the integrated estimator.
Large lateral excitation	$\tau_{a,\max} = \max_{\tau \in [t - t_h, t]}\left(\tau_a(\tau)\right),$ $\mu_{lower\,bound} = \frac{256}{27}\frac{\tau_{a,\max}}{F_z c}.$	$\tau_{a,\max} = \max_{\tau \in [t - t_h, t]}\left(\tau_a(\tau)\right),$ $\mu_{lower\,bound} = \frac{256}{27}\frac{\tau_{a,\max}}{F_z c}.$	It is valid when longitudinal excitation is small. It provides the lower bound of the friction coefficient.
Small longitudinal excitation (0-2%)	$y(t) = \varphi^T(t)\theta(t),$ $y(t) = a_x + g\sin\Theta + \frac{R_{xf} + R_{xr} + D_A}{m},$ $\varphi(t) = \frac{\kappa_{rl} + \kappa_{rr}}{m},\ \ \theta(t) = K(\mu).$	$y(t) = \varphi^T(t)\theta(t),$ $y(t) = a_x + g\sin\Theta + \frac{R_{xf} + R_{xr} + D_A}{m},$ $\varphi(t) = \frac{\kappa_{rl} + \kappa_{rr}}{m},\ \ \theta(t) = K(\mu).$	
Large longitudinal excitation (30-100%)	$y(t) = \varphi^T(t)\theta(t),$ $y(t) = \frac{a+b}{a}\left(\frac{a_x}{g} + \sin\Theta + \frac{R_{xf} + R_{xr} + D_A}{mg}\right),$ $\varphi(t) = 1,\ \ \theta(t) = \mu.$	$y(t) = \varphi^T(t)\theta(t),$ $y(t) = \frac{a+b}{a}\left(\frac{a_x}{g} + \sin\Theta + \frac{R_{xf} + R_{xr} + D_A}{mg}\right),$ $\varphi(t) = 1,\ \ \theta(t) = \mu.$	
All other excitations	-	$\dot{\hat{\alpha}}_f = \left(\frac{1}{mv_x} + \frac{a^2}{I_z v_x}\right)\hat{F}_{yf} + \left(\frac{1}{mv_x} - \frac{ab}{I_z v_x}\right)\hat{F}_{yr} - r - \dot{\delta} + l_1\left(ma_y - \left(\hat{F}_{yf} + \hat{F}_{yr}\right)\right) + l_2\left(\tau_a - \hat{\tau}_a\right),$ $\dot{\hat{\mu}} = 0.$	Open loop observer is used for the integrated estimator.

5.2 Integration of the Estimators

We proposed two estimation algorithms for lateral excitation in CHAPTER 3 and two estimation algorithms for longitudinal excitation in CHAPTER 4. In Chapter 5.1, the medium lateral excitation based algorithm is modified to work with combined excitation cases. Also, an open-loop observer is proposed to cover the cases that are not handled by these algorithms. The lateral dynamics based methods and longitudinal dynamics based methods are complementary because they rely on different excitation conditions. Therefore, they are integrated through switching, which is mainly based on the level and the type of excitations.

The excitation index and the activation condition for the medium lateral excitation based method can be determined by the stability map shown in Figure 5.8 (a), which is the same as Figure 3.13. The estimator should be activated when the tuple of the normalized front tire slip angle and the normalized rear tire slip angle is in the blue region. The normalized slip angles, $\bar{\alpha}_f$ and $\bar{\alpha}_r$ are defined as follows:

$$\bar{\alpha}_f = \left| \frac{\alpha_f}{\alpha_{f,sl}} \right|, \quad \bar{\alpha}_r = \left| \frac{\alpha_r}{\alpha_{r,sl}} \right|, \tag{5.5}$$

where

$$\alpha_{f,sl} = \tan^{-1}\left(\frac{3\mu F_{zf}}{2c_p l^2} \right), \qquad \alpha_{r,sl} = \tan^{-1}\left(\frac{3\mu F_{zr}}{2c_p l^2} \right).$$

To evaluate these indices, we need the slip angles and the friction coefficient, which are the unknowns that we are estimating. Rather than using the normalized slip angles, we will use the normalized lateral acceleration and the normalized angle difference, which are defined as follows:

$$index1 = \frac{a_y}{\mu g}, \qquad index2 = \frac{(a+b)r / v_x - \delta}{\alpha_{f,sl} + \alpha_{r,sl}}. \tag{5.6}$$

where the two indices are still dependent on the friction coefficient but not on the slip angles. For implementation, we use $\hat{\mu}$ instead of μ.

The stability map based on these two new indices can be achieved by the transformation of the stability map shown in Figure 5.8 (a). The transformation functions are from the vehicle lateral dynamics (2.1) and the kinematic angle relationship (2.2), as follows:

$$\begin{aligned} a_y &= \frac{F_{yf}(\alpha_f, \mu) + F_{yr}(\alpha_r, \mu)}{m}, \\ (a+b)r / v_x - \delta &= \alpha_f - \alpha_r. \end{aligned} \tag{5.7}$$

By mapping from the α_f–α_r coordinate to the *index1*–*index2* coordinate, we achieve a new stability map, as shown in Figure 5.8 (b).

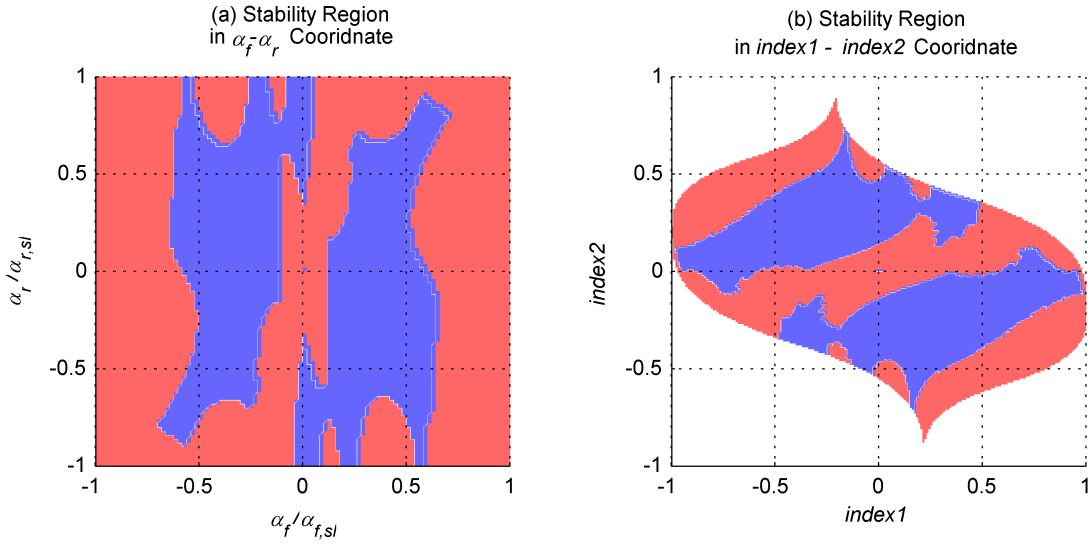

Figure 5.8 The stability map in the α_f–α_r coordinate (a), The stability map in the *index1*–*index2* coordinate (b)

The medium lateral excitation based method should be activated when the tuple of *index1* and *index2* is in the blue region. The activation condition is a function of *index1* and *index2* and is defined as follows:

$$Activate \quad if \ f_{blue}(index1, index2) = True \tag{5.8}$$

where

$$f_{blue}(x,\ y) = g(x,\ \ y) \text{ OR } g(-x, -y)$$

$$g(x,\ \ y) = \begin{cases} True, & If\ \ g_{upper}(x,\ \ y) <= 0\ \ AND\ \ g_{lower}(x,\ \ y) >= 0, \\ False, & Otherwise \end{cases}$$

The boundary curves of the upper left blue region can be approximated by $f_k(-x, -y)$, because both regions are point symmetrical. The regions consist of two curves, upper and bottom, named g_{upper} and g_{lower}, which are interpolation functions of several points. The points of the two functions are listed in Table 5.2.

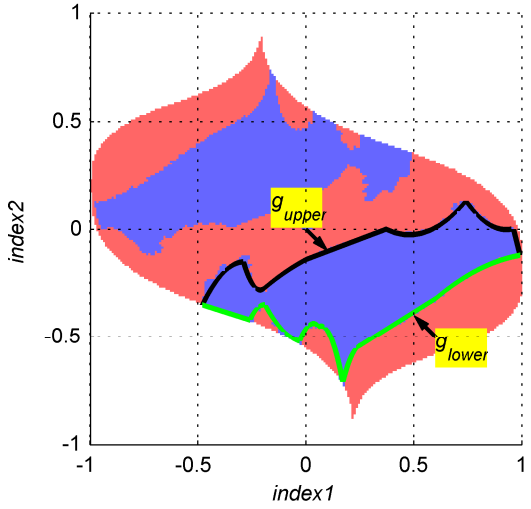

Figure 5.9 The boundary curves of the stable region

The maximum self-aligning moment detection method is used when a large lateral excitation exists. This method is valid only when longitudinal excitation does not exist because the method is based on a pure lateral slip tire model. This method always underestimates the friction coefficient if the lateral excitation is not sufficiently large, thus it can provide the lower bound of the friction coefficient to other estimators. Therefore, we do not need to turn off this method unless there is longitudinal excitation. The activation condition of the large lateral excitation based method is as follows:

$$\left|\kappa_{fl}\right| < 0.02 \ \ and \ \ \left|\kappa_{fr}\right| < 0.02. \tag{5.9}$$

The activation condition for the small slip ratio method is that both driving wheels' slip ratio should be less than 2%, as shown in Figure 4.22. The activation condition for the large slip ratio method is that one of the driving wheels' slip ratio should be larger than 30%, as shown in Figure 4.2. Both longitudinal based algorithms are valid only when the lateral excitation is small, which can be defined as follows:

$$\left|a_y\right| < 0.5\, m/s^2 \; and \; \left|r\right| < 0.05 \; rad/s. \tag{5.10}$$

Table 5.2 The points for the interpolation function of the boundary curves

g_{upper}						g_{lower}					
No.	*x*	*y*	*No.*	*x*	*y*	*No.*	*x*	*y*	*No.*	*x*	*y*
1	-0.480	-0.350	14	0.370	0.000	1	0.893	-0.146	14	0.038	-0.437
2	-0.433	-0.265	15	0.463	-0.026	2	0.795	-0.187	15	0.015	-0.444
3	-0.385	-0.203	16	0.555	-0.013	3	0.698	-0.246	16	-0.008	-0.472
4	-0.337	-0.165	17	0.648	0.039	4	0.600	-0.320	17	-0.030	-0.520
5	-0.290	-0.150	18	0.740	0.130	5	0.250	-0.540	18	-0.070	-0.501
6	-0.265	-0.221	19	0.793	0.066	6	0.230	-0.556	19	-0.110	-0.466
7	-0.240	-0.265	20	0.845	0.023	7	0.210	-0.589	20	-0.150	-0.416
8	-0.215	-0.281	21	0.898	0.001	8	0.190	-0.640	21	-0.190	-0.350
9	-0.190	-0.270	22	0.950	0.000	9	0.170	-0.710	22	-0.208	-0.352
10	-0.143	-0.232	23	0.990	-0.120	10	0.143	-0.586	23	-0.225	-0.365
11	-0.095	-0.198				11	0.115	-0.501	24	-0.243	-0.387
12	-0.047	-0.167				12	0.088	-0.456	25	-0.260	-0.420
13	0.000	-0.140				13	0.060	-0.450	26	-0.480	-0.350

Using the excitation conditions, the overall estimation flow of the integrated estimator is shown in Figure 5.10. The estimators are activated based on the magnitude of excitation signals, and the initial values for the estimator are the last estimated results of the previously selected estimator. The estimation process is grouped into three categories based upon the magnitude and the kinds of excitation. The evaluation of this integrated algorithm will be performed by the simulations similarly to Chapter 5.3.

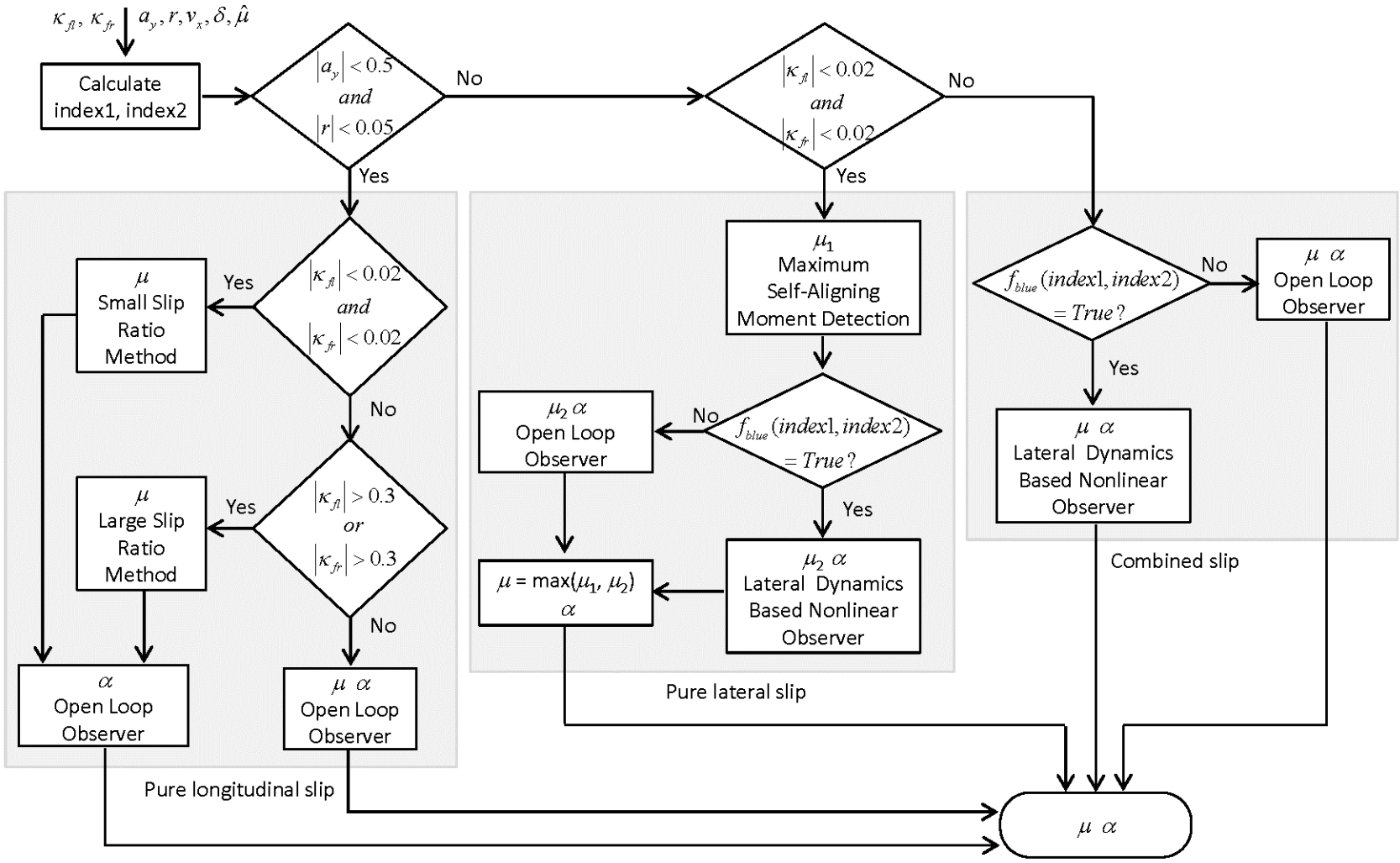

Figure 5.10 Estimation flow of the integrated estimator

5.3 Simulations

The performance of the integrated algorithm is evaluated by simulations. The test maneuvers and road surfaces are designed for the vehicle to undergo various excitations. The load surface is designed to have sudden friction coefficient changes. The test maneuvers are designed using different steering inputs and gas pedal inputs. Two maneuvers are used. For Simulation #1, the steering input is zero until 10 second and sinusoidal after 10 second. The gas pedal input is intermittent until 8 second and zero after that. For Simulation #2, the steering input is sinusoidal and the gas pedal input is intermittent for the whole simulation time.

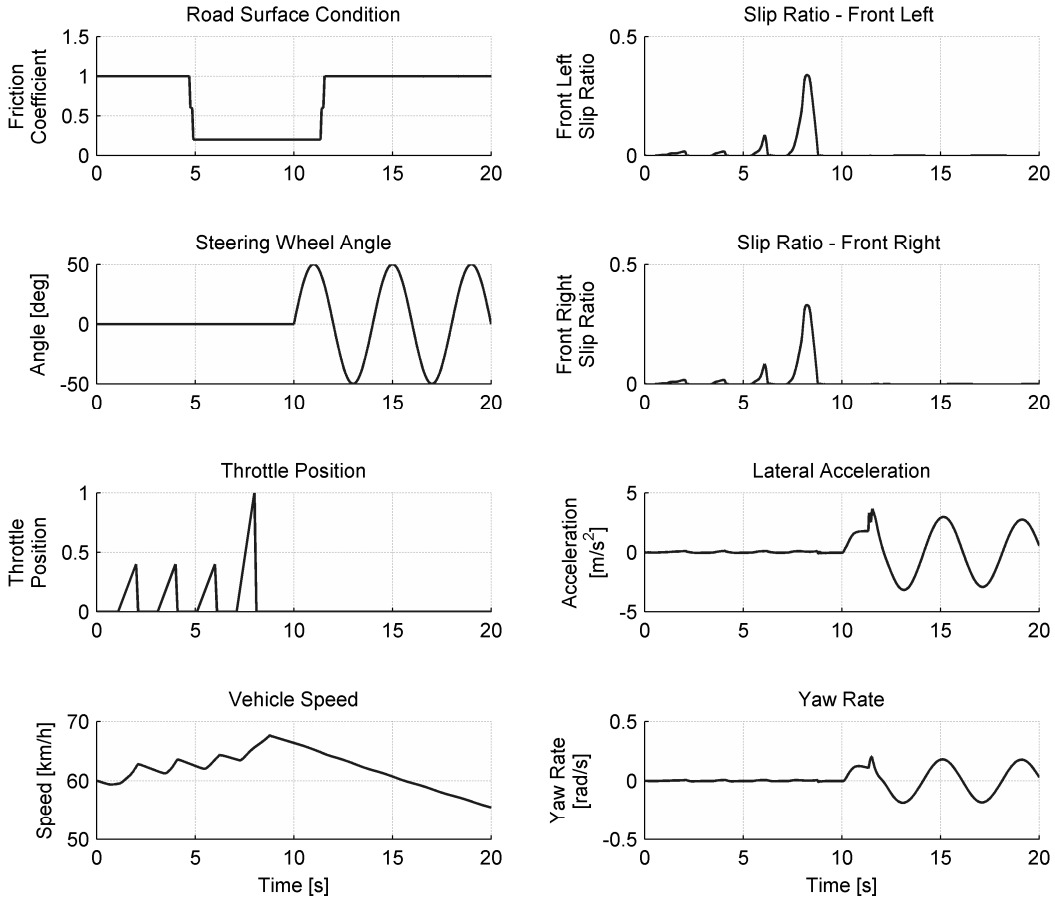

Figure 5.11 Excitation inputs and vehicle states of Simulation #1

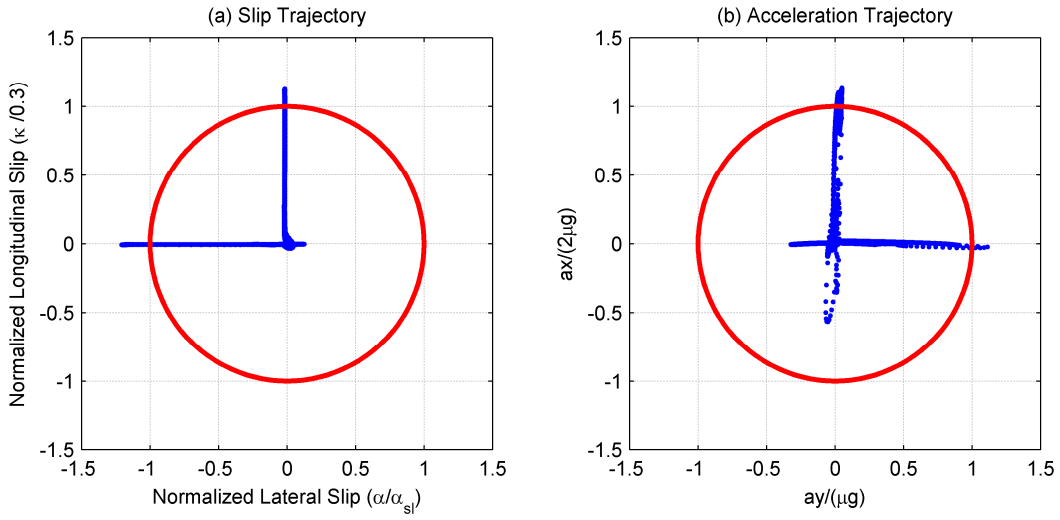

Figure 5.12 Excitation trajectory of Simulation #1 in the friction circle

The inputs and coressponding vehicle states for Simulation #1 are shown in Figure 5.11, where only longitudinal excitations exist during the first half of the test and only lateral excitations during last half of the test. The correspoding excitation trajectories are plotted in Figure 5.12, where the left plot shows the slip trajectory normalized in staturation slip and the right plot shows the acceleration trajectory normalized by the maximum accleration. Note that the longitudinal acceleration is normalized by $\mu g/2$ because the vehicle is a front wheel drive car.

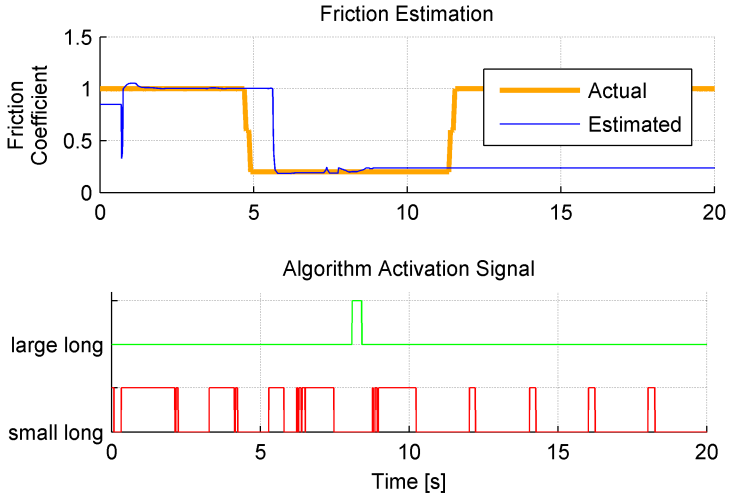

Figure 5.13 Estimation results of Simulation #1 using the longitudinal excitation based algorithms

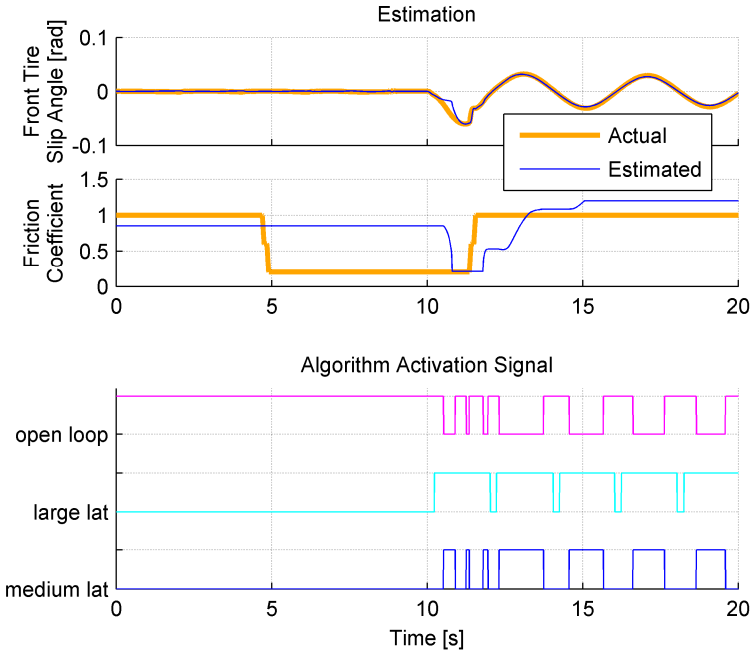

Figure 5.14 Estimation results of Simulation #1 with the lateral excitation based methods and the open loop observer turned on

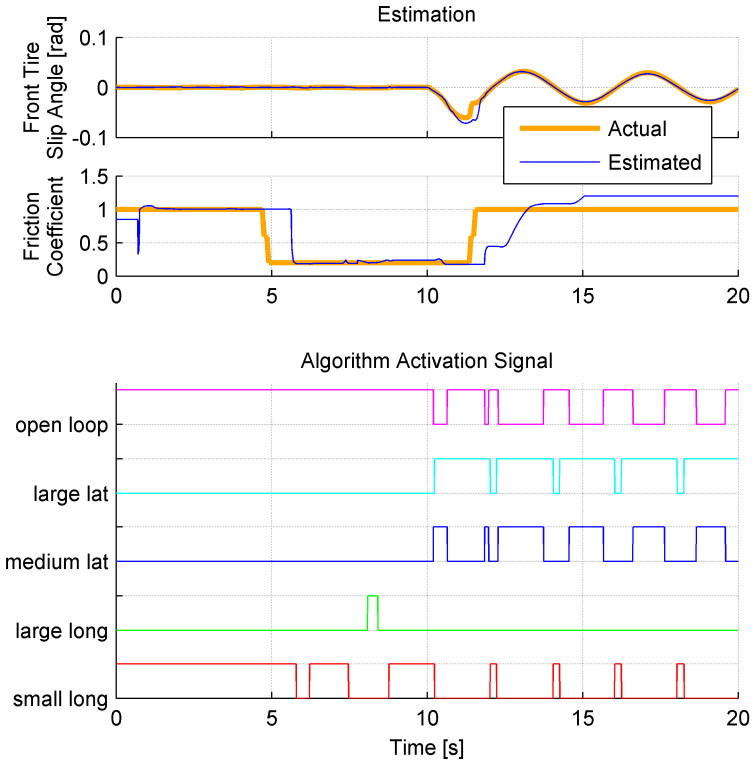

Figure 5.15 Estimation results of Simulation #1 using the integrated algorithm

The longitudinal excitation based algorithms only work for the first 10 seconds and do not estimate the friction coeffiicient after 10 seconds, as shown in Figure 5.13, due to the lack of sufficient longitudinal excitations. However, the lateral excitation based algorithms only work for the last 10 seconds, as shown in Figure 5.14. If we apply the integrated algorithm for the same simulation data, the algorithm effectively takes advantage of the both excitations, as shown in Figure 5.15. It is worthwhile to note that the large lateral excitation based algorithm is activated even when there is not enough large lateral excitation because it can provide the lower bound of the friction coefficient when lateral excitation is small.

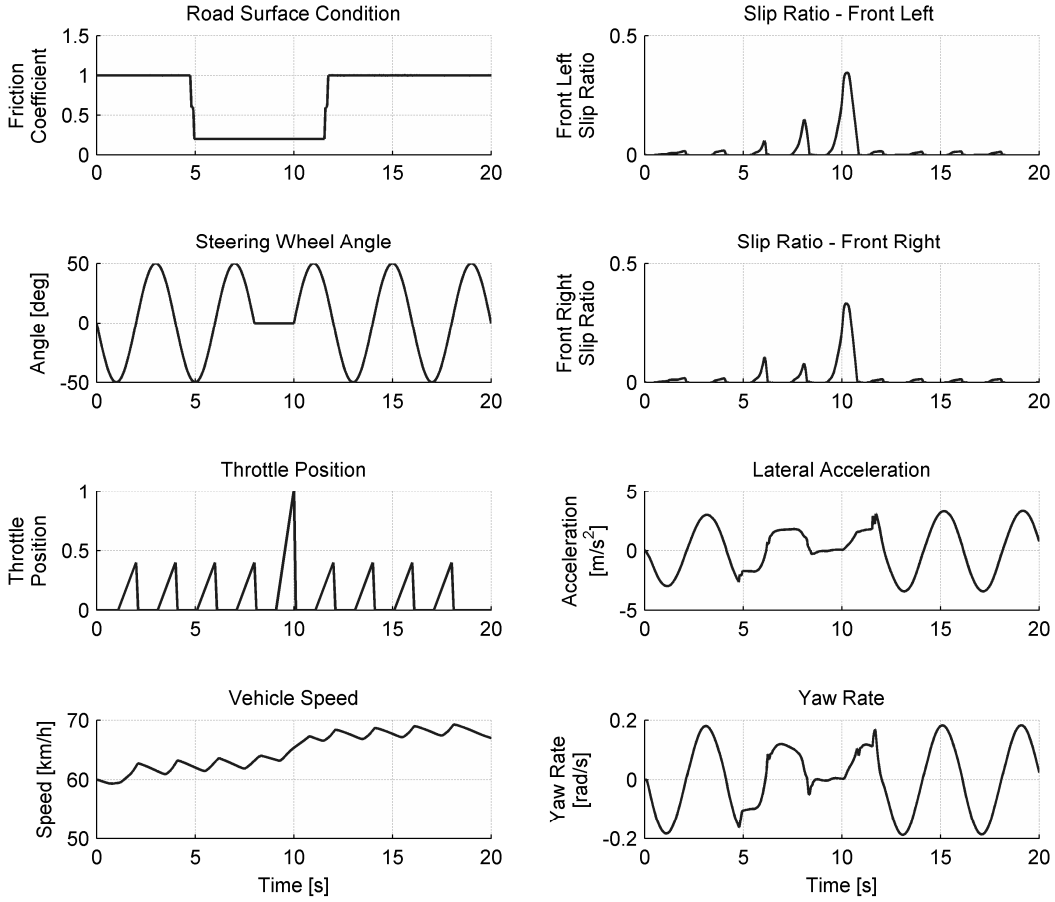

Figure 5.16 Driver's inputs and vehicle states of Simulation #2

Simulation #2 is designed to have both directional excitations at the same time. Figure 5.16 shows the driver's inputs and vehicle states of the simulation. The excitation

trajectory plot, Figure 5.17, shows that the vehicle frequently experiences the combined slip.

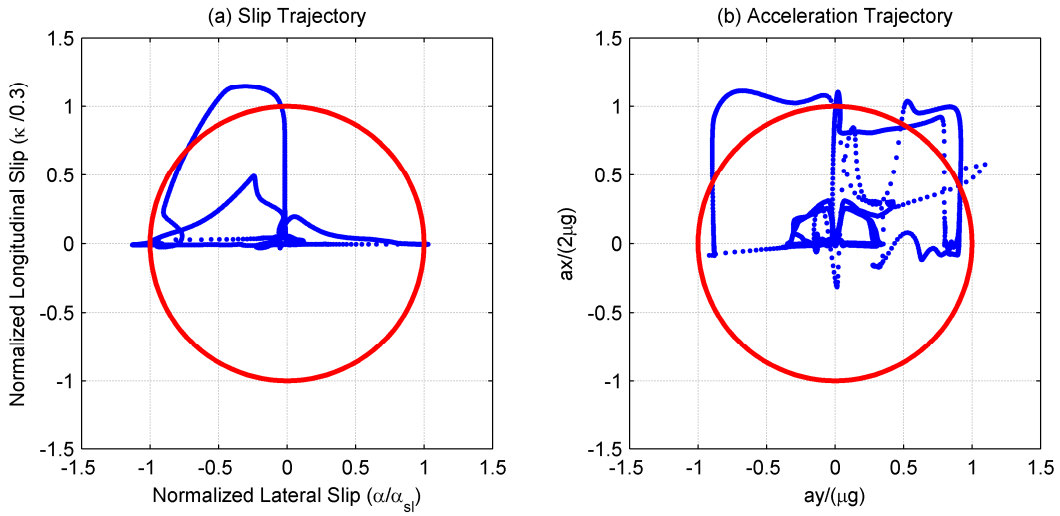

Figure 5.17 Excitation trajectory of Simulation #2 in the friction circle

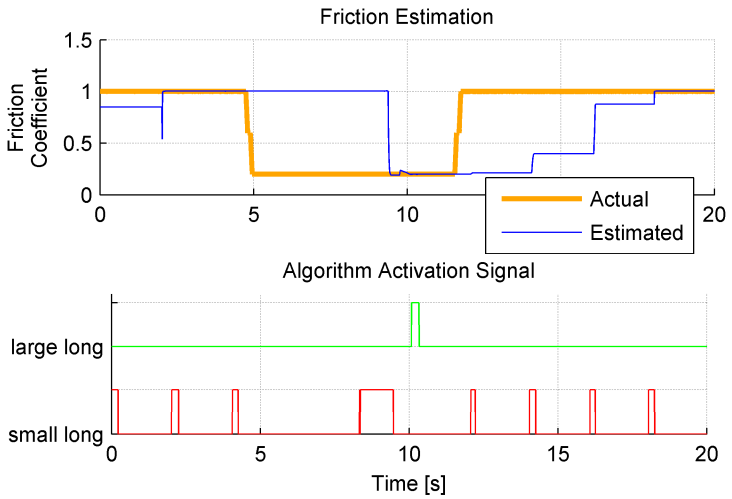

Figure 5.18 The estimation result of Simulation #2 with the small and large longitudinal slip based methods turned on

In Simulation #2, the longitudinal excitation based algorithms have fewer chances of activation than in Simulation #1 due to the lack of pure longitudinal excitations. Therefore, the friciton coefficient is updated less frequently and the convergence is slow, as shown in Figure 5.18. However, the frequent lateral excitations are beneficial to the

lateral excitation based algorithms, which provide better accuracy and convergence than the longitudianl excitation based algorithms, as shown in Figure 5.19.

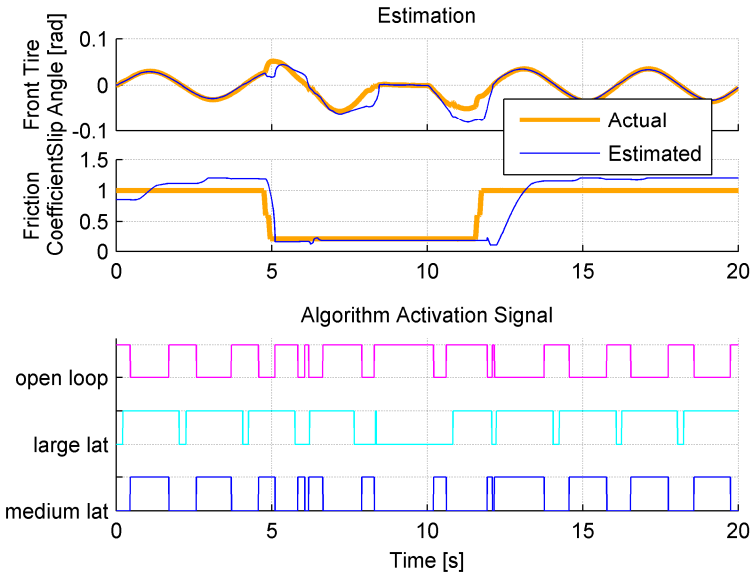

Figure 5.19 The estimation result of Simulation #2 with the lateral excitation based methods and the open loop observer turned on

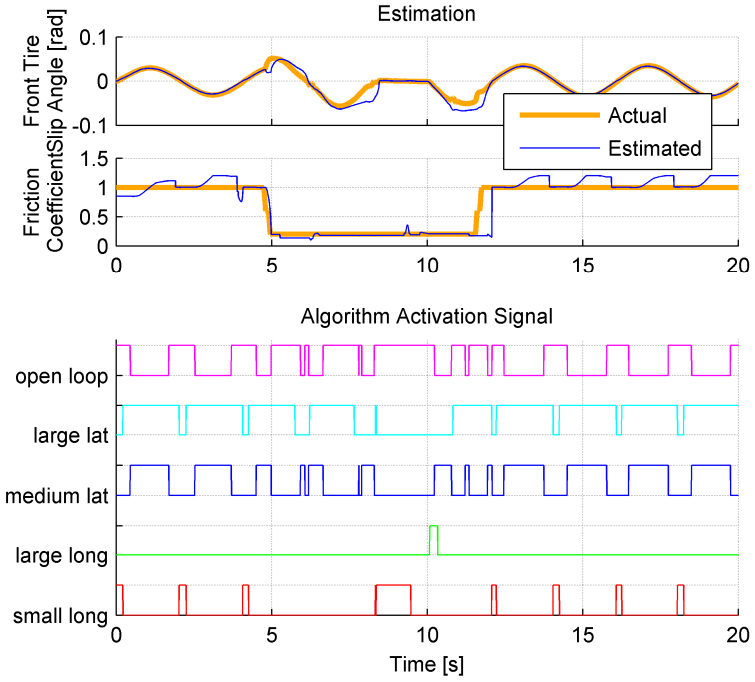

Figure 5.20 The estimation result of Simulation #2 using the integrated algorithm

The integrated algorithm shows better performance than any longitudinal or lateral excitation based algorithms, as shown in Figure 5.20. At 12 seconds, the friciton coefficient estimated by the integrated algorithm shows faster convergence than that of Figure 5.19 thanks to longitudinal excitations.

These simulation results show that the integrated algorithm works for wider range of excitations and shows superior performance than any single directional excitation based algorithms. Figure 5.21 shows the estimation errors for different excitation based algorithms. Due to the step change of the surface, a maximum error is not a good indicator of the estimation quality. The integrated alogithm shows the better estimation quality in the sense of RMS (Root Mean Square) error for both simulations. Note that the longitudinal excitation based method does not estimate slip angles. The experimental evaluation will be discussed in CHAPTER 6 and the results will show that the proposed algorithm has practical applicability to vehicle active safety control.

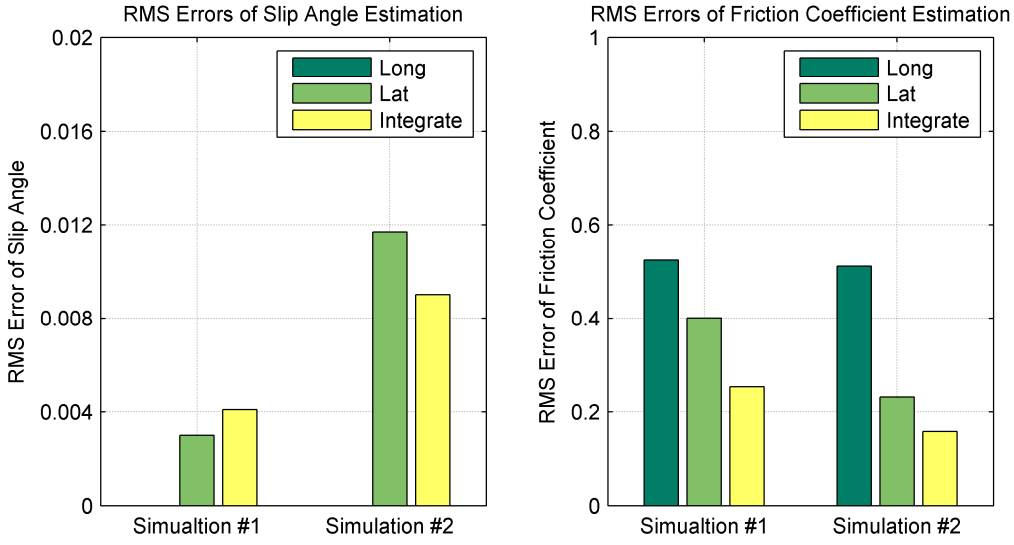

Figure 5.21 Performance comparison between estimation algorithms

CHAPTER 6
EXPERIMENTAL VALIDATION

6.1 Experimental Vehicle

The experimental validation of the proposed algorithms was performed on Ford Motor Company's winter test track in Sault Ste. Maire, Michigan. The test vehicle used was a rear wheel drive Jaguar S-type, specially modified for the development of vehicle dynamics control algorithms. This car is equipped with several active safety systems including AFS (active front steering), ABS (anti-lock braking system), TCS (traction control system), and ESC (electronic stability control). Given the presence of these systems, we had access to a large set of vehicle state measurements, available from standard ESC sensors, such as an inertial yaw rate and lateral acceleration sensor, four wheel speed sensors, a steering wheel angle sensor, and a steering torque sensor. Figure 6.1 shows the test vehicle.

Figure 6.1 The test vehicle and GPS/INS system

An additional piece of test equipment, Oxford Technology RT-2500, was used to provide the reference (truth) signals. It has two antenna based GPS integrated with INS and enables measurements of three dimensional vehicle positions and orientations as well

as three dimensional linear and angular velocities of the vehicle. The performance specification of RT-2500 is shown below in Table 6.1.

Table 6.1 Performance specification of RT-2500

Signal	Accuracy	Signal	Accuracy
Position	3.0m CEP*	Angular Rate	
Velocity	0.2 km/h RMS	– Bias	0.02º/s 1σ
Acceleration		– Scale Factor	0.2º/s 1σ
– Bias	10 mm/s^2 1σ	– Range	100º/s
– Linearity	0.01% 1σ	Track** (at 50 km/h)	0.25º 1σ
– Scale Factor	0.1% 1σ	Slip Angle (at 50 km/h)	0.4º 1σ
– Range	100 m/s^2	Lateral Velocity	0.04% 1σ
Roll/Pitch	0.15º 1σ	Update Rate	100 Hz
Heading	0.3º 1σ	Calculation Latency	3.9 ms

*CEP: Circular Error Probable
**Track: Angle from the north to the velocity direction

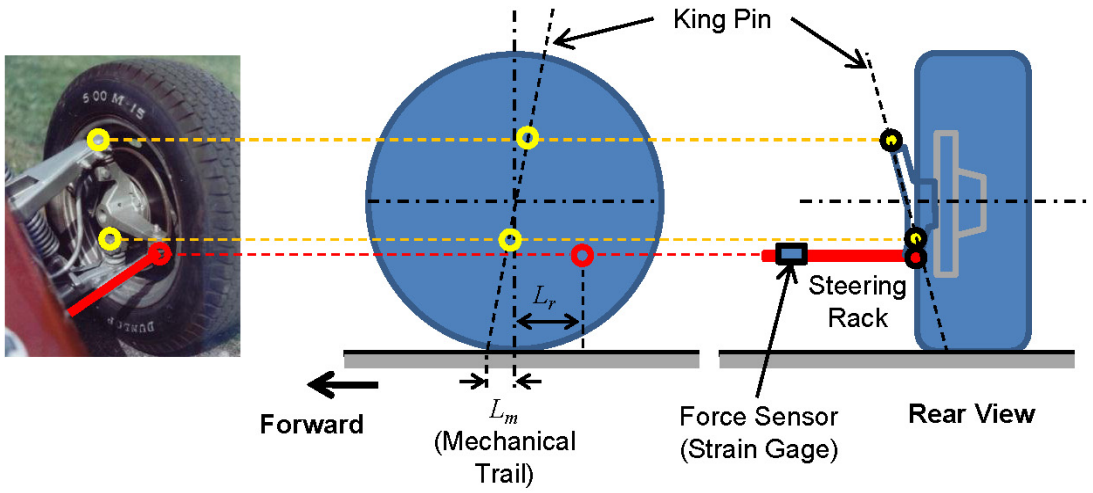

Figure 6.2 Steering system geometry and the location of the force sensor

For the measurement of the aligning moment of the front tires, the car, unfortunately, does not have an electric steering power system that can measure the tire reactive moment against the road through the assisting motor current. The car has a

conventional hydraulic power assisting system; therefore, strain gauges are installed at both steering racks, as shown above in Figure 6.2. The sensors installed in the test vehicle are listed below in Table 6.2 and categorized in terms of their purpose.

Table 6.2 Sensors installed in test vehicle

For algorithm implementation	For reference signal acquisition
Yaw rate sensor	Vehicle position (GPS)
Lateral accelerometer	Vehicle orientation (GPS)
Longitudinal accelerometer	3-dimensional velocities (GPS)
Wheel speed sensor	3-dimensional acceleration (GPS)
Steering wheel angle sensor	3-dimensional angular velocities (GPS)
Rack force sensor	Vehicle slip angle (GPS)
	Road steer angle sensor

The test site has several kinds of well-maintained surfaces, such as a concrete road, a dry icy road, and a packed snow road. Vehicle tests were performed on several surfaces with several maneuvers to evaluate the performance and robustness of the algorithms. Figure 6.3 shows the main test track of the test site.

Figure 6.3 Test track

The tests were designed for the two purposes: parameter identification and algorithm verification. For parameter identification, the maneuver was carefully controlled to obtain clean signals on even surfaces, such as on dry ice or packed snow.

For the algorithm verification, three kinds of maneuvers were designed: lateral excitation oriented maneuvers, longitudinal excitation oriented maneuvers, and combined excitation oriented maneuvers. Table 6.3 lists the designed tests, their purposes, the excitations each involved, and the surfaces they were tested on.

Table 6.3 The list of tests

Test No.	Major excitation	Main Purpose	Surface
1	Lateral (Circular turn)	Tire parameter identification	Ice
2	Lateral (Circular turn)	Tire parameter identification	Snow
3	Lateral (Sinusoidal steer input)	Steering parameter identification	Snow
4	Lateral (Single lane change)	Model validation	Snow
5	Lateral (Sinusoidal steer input)	Evaluation of lateral dynamics based algorithms	Mixed
6	Lateral (Single lane change)	Evaluation of lateral dynamics based algorithms	Mixed
7	Longitudinal (Acceleration/Deceleration)	Evaluation of longitudinal dynamics based algorithms	Mixed
8	Longitudinal + Lateral (Single Lane change)	Evaluation of the integrated algorithms	Mixed

6.2 Model Identification and Validation

6.2.1 Vehicle and Tire Parameter Identification

While vehicle parameters are easily obtained from the vehicle design specifications, tire parameters are usually not readily available and therefore need to be identified through bench tests or vehicle tests. We performed steady state turning maneuvers (Test 1 and Test 2) to identify the key tire parameters: stiffness of the tread

element and the length of contact patch. In contrast, the steering system parameters, such as the rotational inertia and the damping coefficient are identified through transient maneuvers in situations involving fast steering changes (Test 3). Finally, a transient maneuver (Test 4) with sinusoidal steering inputs was performed for the purpose of verifying the fidelity of the vehicle and tire models.

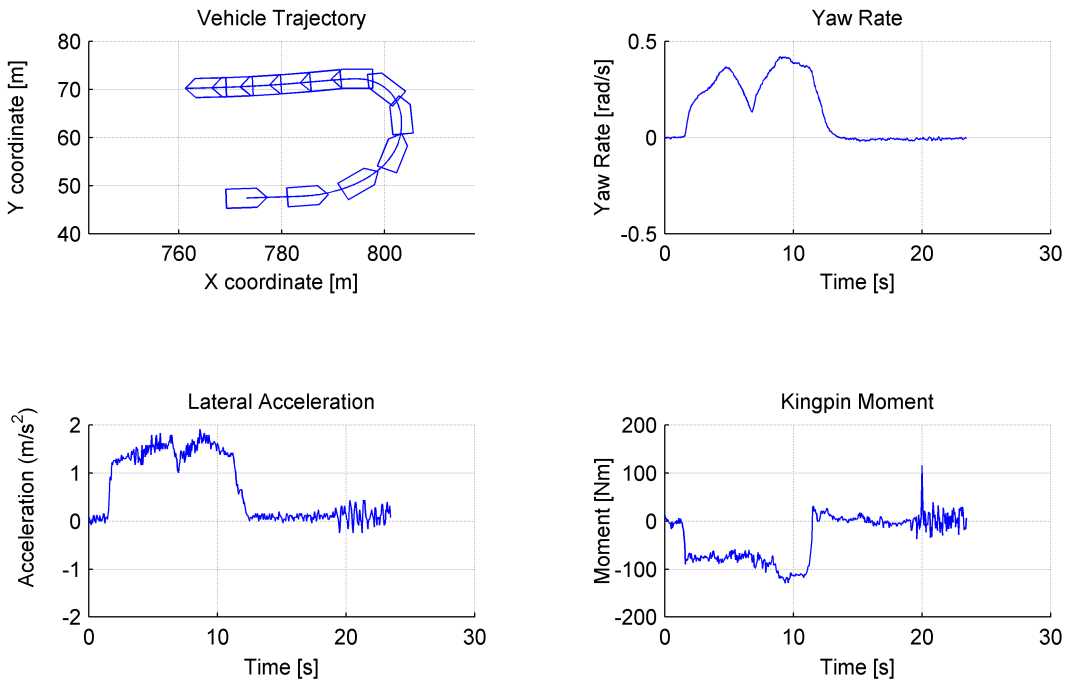

Figure 6.4 Measured signals of the steady state maneuver on ice (Test 1)

Figure 6.4 shows the signals of a J-turn maneuver that was designed for tire parameter identification. The tire parameters, contact patch length, l, and tread stiffness, c_p, are identified from the tire force and moment versus the slip angle plot. The lateral tire force and king-pin moment were measured and the tire models, $f_y(\alpha, \mu)$ and $\tau_a(\alpha, \mu)$, are given as (2.12) and (2.13). The slip angle α was measured and μ can be determined from extreme braking maneuvers. The signals from the identified tire model and the measured signals are compared in Figure 6.5, where the king-pin moment is achieved from the measured rack force and moment arm length L_r and the tire lateral force is extracted from the lateral acceleration and the yaw-rate using the following equations. Note that the time derivative of the yaw rate was obtained using an off-line low-pass-filter only for identification and verification purposes.

$$F_f = \frac{b \cdot m \cdot a_y + I_z \dot{r}}{(a+b)\cos\delta}, \quad F_r = \frac{a \cdot m \cdot a_y - I_z \dot{r}}{(a+b)}. \tag{6.1}$$

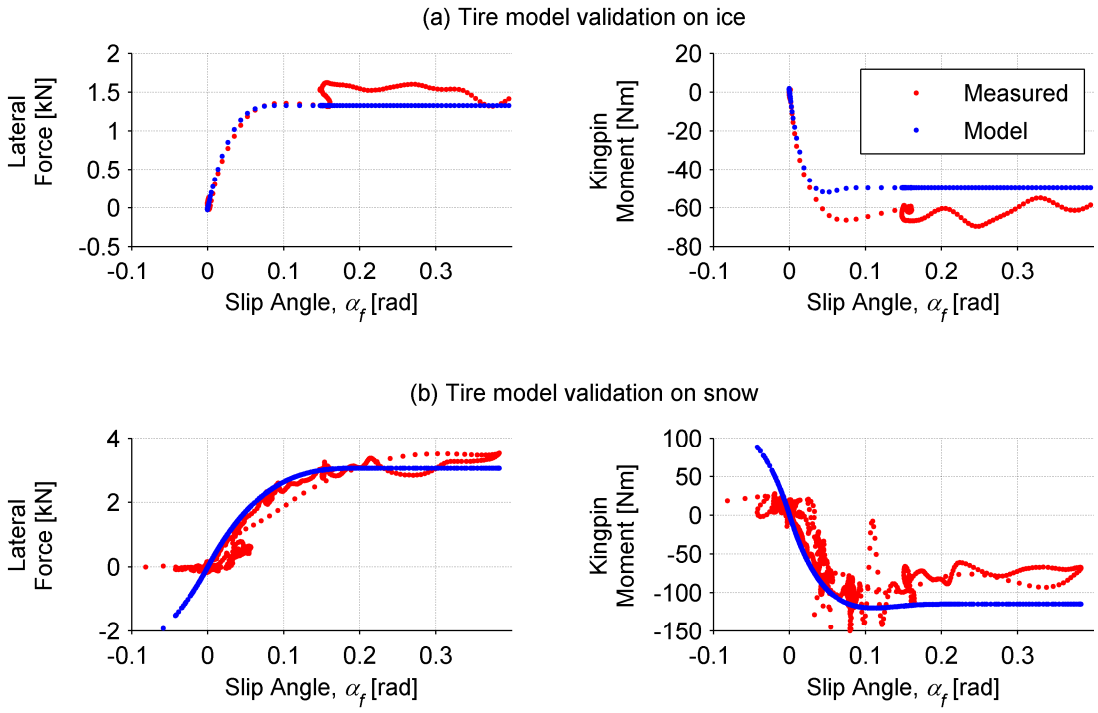

Figure 6.5 Measured tire force vs. model predicted tire force (Test 1 and Test 2)

6.2.2 Steering System Parameter Identification

The steering system parameters, including the effective inertia and damping coefficient of the steering system, affect the aligning moment measurement and are identified from the transient maneuvers that cause sufficient inertial and damping resistance moments for identification. The steering system with correlated force and moment is shown in Figure 6.6. The corresponding dynamics are:

$$J_{eff}\ddot{\delta} + b_{eff}\dot{\delta} + k\delta = \tau_a + f_y \cdot L_m - f_{rack} \cdot L_r, \tag{6.2}$$

where δ is the road steer angle, J_{eff} is the effective moment of inertia, b_{eff} is the effective damping of the steering system, and k is the jack-up moment coefficient. The parameters are identified using the following equations:

$$
\begin{aligned}
&[J_{eff},\, b_{eff}, k] = \arg\min_{J,b,k} \sum \left(\tau_{king\ pin} - \hat{\tau}_{king\ pin}\right)^2, \\
&\tau_{king\ pin} = f_{rack} \cdot L_r, \\
&\hat{\tau}_{king\ pin} = \hat{\tau}_a + \hat{f}_y \cdot L_m - \left(J\ddot{\delta} + b\dot{\delta} + k\delta\right),
\end{aligned}
\tag{6.3}
$$

where $\hat{\tau}_a$ and $\hat{f}_y$ can be computed using (2.12) and (2.13).

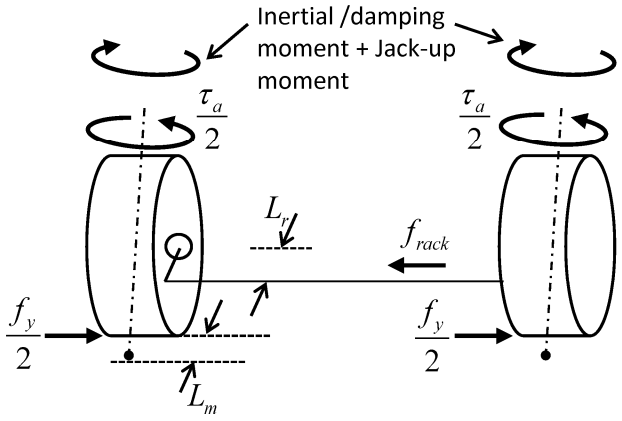

Figure 6.6 Steering system and rack force measurement

Table 6.4 Model parameters of the test vehicle

Parameter	Value	Unit	Description
m	2050	kg	Vehicle mass
I_z	3344	kg·m^2	Yaw moment of inertia of the vehicle
a	1.432	m	Distance from front axle to center of mass
b	1.472	m	Distance from rear axle to center of mass
w	1.52	m	Vehicle track width
l	0.1	m	Half of the tire contact length
c_p	1.65 ×10^6	N/m^2	Tread stiffness of unit length
J_{eff}	4	kg·m^2	Effective rotational inertia
b_{eff}	88	Nm/(rad/s)	Effective damping coefficient
k	–362	Nm/rad	Jack-up moment coefficient

The steering system parameters are identified through the optimization process and listed in Table 6.4. The comparison of the king-pin moment signals from the model and the measurements is shown in Figure 6.7, where the king-pin moment signal from the model has phase lead against the measured signal. If we ignore all the steering system dynamics, then the model error is within the range of −90~80 Nm. The model with the identified steering system parameters shows an in-phase signal match and reduced error whose range is −50~50 Nm. The identified vehicle and tire models are validated, as shown in Figure 6.8, which demonstrates good agreement with the measured results.

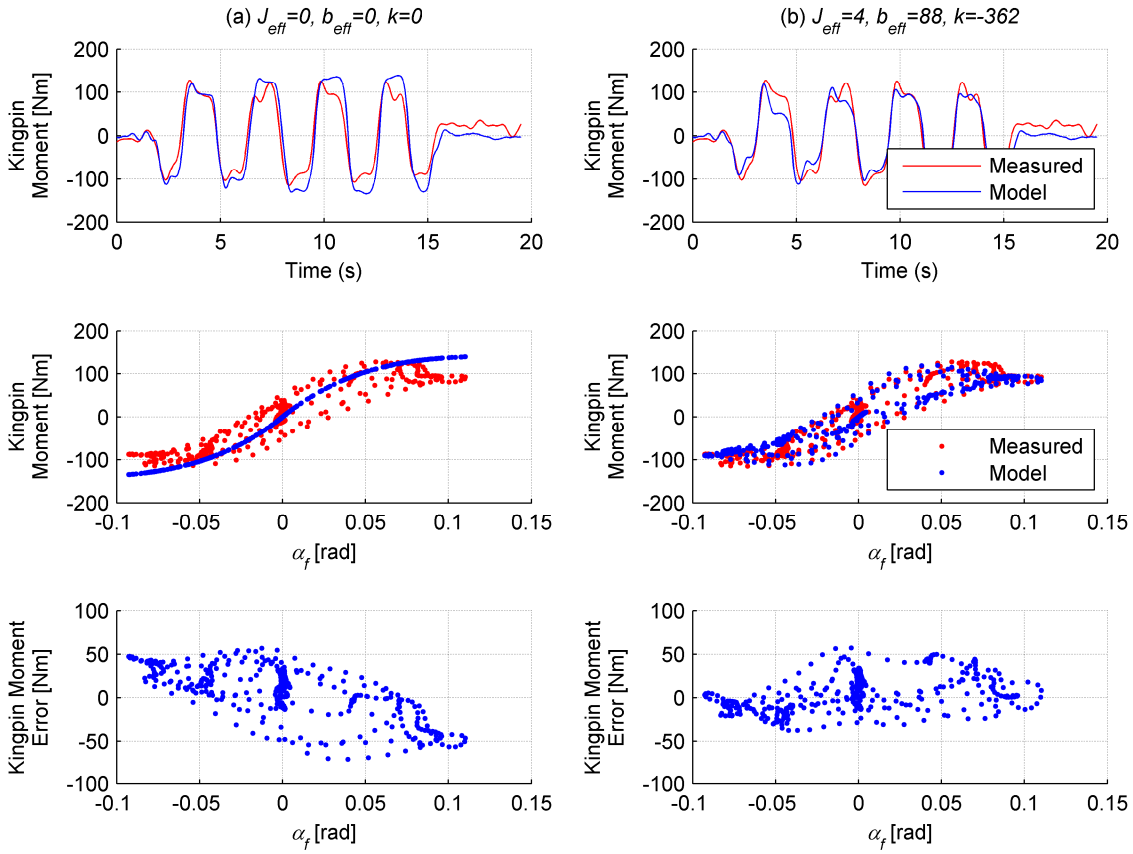

Figure 6.7 Comparison of the kingpin moment signals

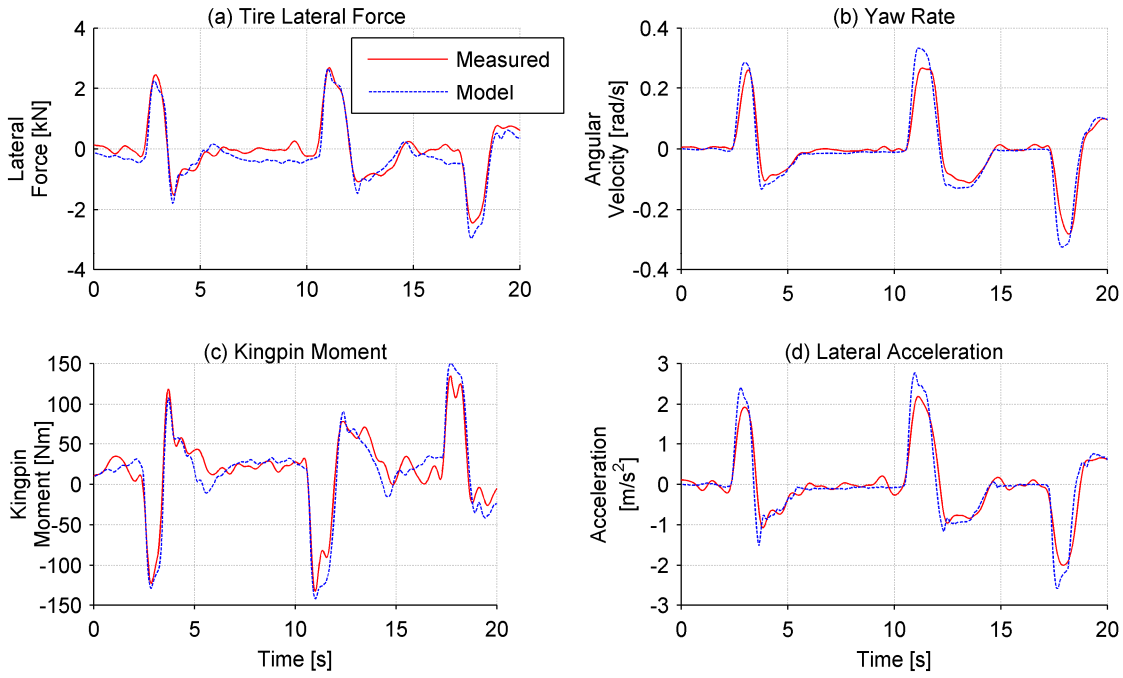

Figure 6.8 Validation of tire, vehicle, and steering system model

6.3 Validation of the Lateral Dynamics Based Algorithm

6.3.1 Observer with King-pin Moment Measurement

The strain gauges installed on the steering rack measure the forces induced by the moment around the king-pin axis. However, the king-pin moment ($\tau_{krack\ pin}$) contains not only the tire aligning moment (τ_a) but also the moment due to the mechanical trail and lateral tire forces (τ_{mech}) and the resistance moment. When these moments are taken together, the aligning moment signals can be obtained as follows:

$$\begin{aligned}\tau_a &= \tau_{king\ pin} - \tau_{mech} + \left(J\ddot{\delta} + b\dot{\delta} + k\delta\right) \\ &= f_{rack} \cdot L_r - f_y \cdot L_m + \left(J\ddot{\delta} + b\dot{\delta} + k\delta\right),\end{aligned} \tag{6.4}$$

where f_{rack} is a measured force at the steering rack and f_y is the tire lateral force.

However, this equation is not used to achieve the tire aligning moment because i) we do not have a sensor to measure tire lateral force in the test configuration, and ii) the aligning moment is smaller than the king-pin moment which results in smaller Signal to

Noise Ratio (SNR) of the aligning moment signal is lower than that of the king-pin moment signal.

In the light of these two issues — absence of a sensor and the smaller SNR of aligning moment signals compared to the SNR of the king-pin moment signals — we use the king-pin moment signal as one of the measurement signals instead of using the aligning moment signal. This change does not have any impact on the observer synthesis introduced in Chapter 3.2.2 as we only need to re-optimize the observer gains. The king-pin moment signal can be obtained using the force signal measured at the tie rod, as follows:

$$\tau_{king\ pin} = f_{rack} \cdot L_r \tag{6.5}$$

For measurement feedback into the observer, the model output of the king-pin moment is derived as follows:

$$\hat{\tau}_{king\ pin} = \hat{\tau}_a + \hat{f}_y \cdot L_m - \left(J\ddot{\delta} + b\dot{\delta} + k\delta \right) \tag{6.6}$$

Then, the observer is as follows:

$$\begin{aligned} \dot{\hat{\alpha}}_f &= \left(\frac{1}{mv_x} + \frac{a^2}{I_z v_x} \right) \hat{F}_{yf} + \left(\frac{1}{mv_x} - \frac{ab}{I_z v_x} \right) \hat{F}_{yr} - r - \dot{\delta} \\ &\quad + l_1 \left(ma_y - \left(\hat{F}_{yf} + \hat{F}_{yr} \right) \right) + l_2 \left(\tau_{king\ pin} - \hat{\tau}_{king\ pin} \right), \\ \dot{\hat{\mu}} &= l_3 \left(ma_y - \left(\hat{F}_{yf} + \hat{F}_{yr} \right) \right) + l_4 \left(\tau_{king\ pin} - \hat{\tau}_{king\ pin} \right). \end{aligned} \tag{6.7}$$

Note that the error of the aligning moment measurement in the feedback term is replaced by the king-pin moment error.

6.3.2 Experimental Validation

The test vehicle traveled around the test track on concrete, ice, snow and slippery concrete surfaces, as shown in Figure 6.9. In other words, the friction levels change abruptly to different levels. The driver was asked to intentionally perform continuous sinusoidal steering to generate sufficient lateral excitation, but not to create a large

longitudinal slip. The front tire slip angle was calculated by using the actual vehicle slip angle measured through the GPS/INS box. The friction coefficient of different surfaces were then identified by a maximum braking acceleration test. Two test runs, with distinctively different levels of excitations, were chosen to evaluate the estimation algorithm. Figure 6.10 shows the measured signals of one of the test runs.

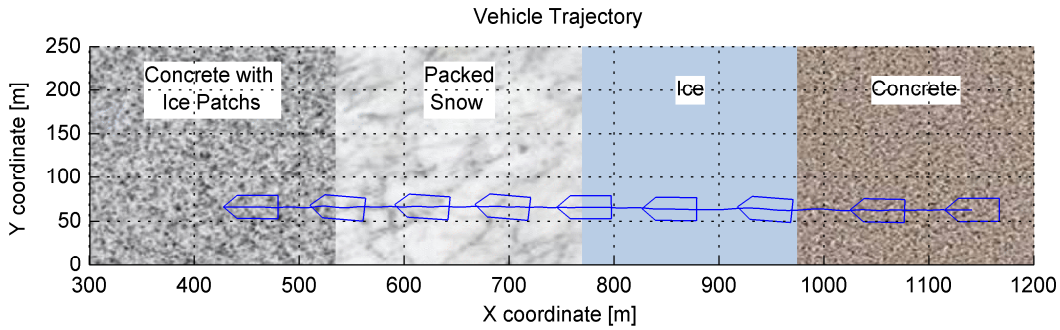

Figure 6.9 The test surface and a vehicle trajectory

The data from Test 5 was obtained with a 0.3 Hz steering input and the measured signals are shown in Figure 6.10. The test vehicle shows an excessively large slip angle on ice where the lateral acceleration and the kingpin moment are generally smaller than those on other surfaces. The estimation result is shown in Figure 6.11, in which "Observer" refers to the estimate from the nominal nonlinear observer and "Switching" refers to the estimate from the switching gain observer. The car experienced three abrupt friction level changes: high to low at around 18 seconds, low to medium at around 41 seconds, and medium to high at around 72 seconds. The most challenging change is the one that occurred at 18 seconds during which the nominal nonlinear observer loses track of the friction coefficient because the difference between the true and estimated friction coefficients is too large to stabilize the observer at the estimated vehicle states. The estimated friction coefficient does not converge to the true value until the estimated vehicle states enter into the stable region. The switching gain observer converges to the true value earlier than the nonlinear observer, thanks to the switching gain algorithm which detects the surface change. The better tracking performance of the switching gain observer is exhibited at 20 seconds and 41 seconds. Between 19 and 22 seconds, the observer underestimates or even fails to estimate the slip angle because of the overestimated friction coefficient. When the vehicle slip angle is large, e.g., on the ice,

the slip angle estimate is not accurate because observability of the slip angle decreases due to tire force saturation, which occurs on low friction surfaces.

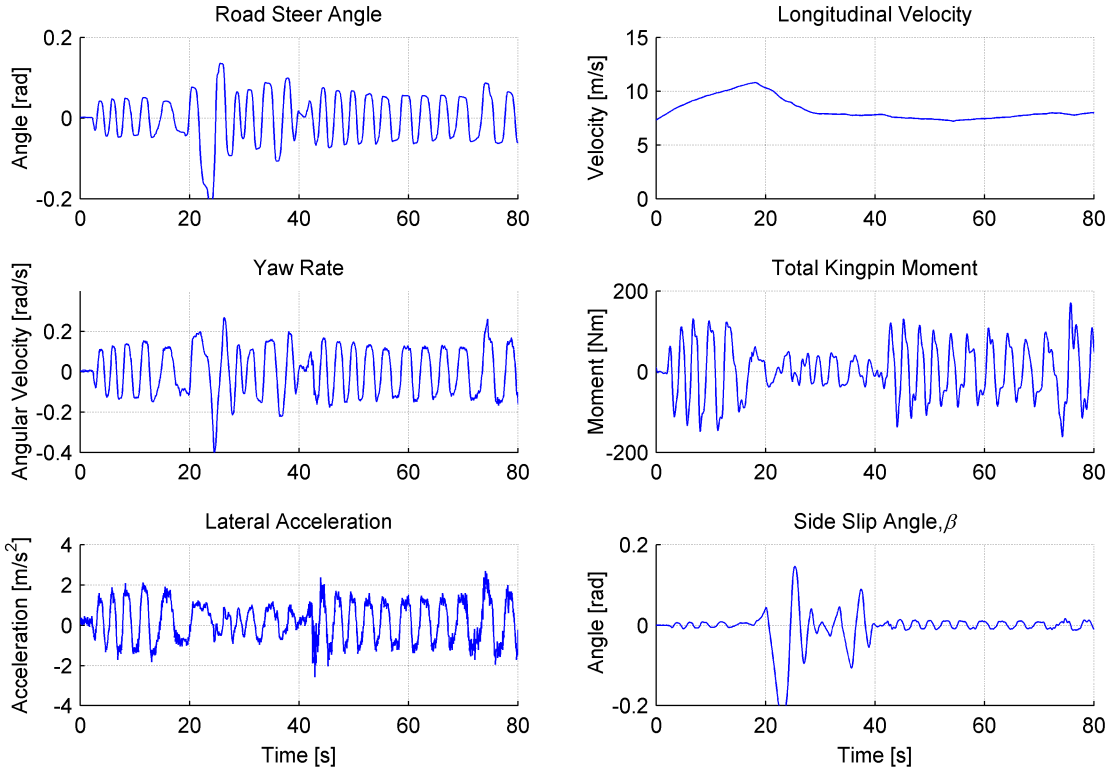

Figure 6.10 Measured signals of Test 5

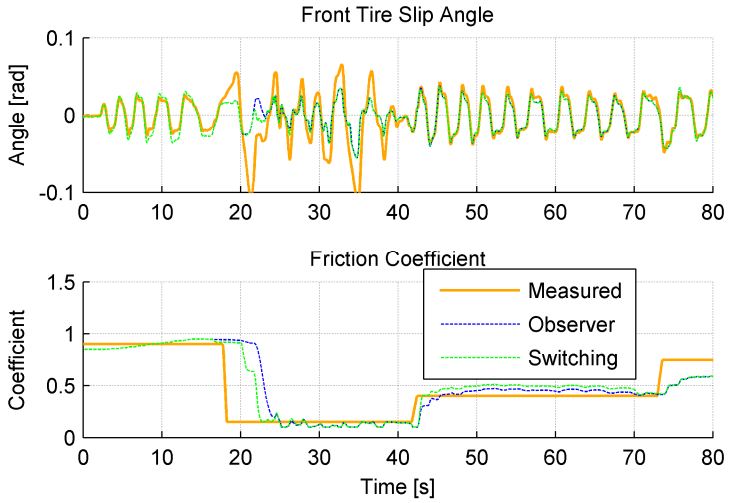

Figure 6.11 Evaluation of the lateral dynamics based algorithm using Test 5

The data of Test 6 was obtained on the same test surface, but with different excitation patterns. The lateral excitation in Test 6 is not as rich as that of Test 5 and is also smaller in magnitude and intermittent as shown in Figure 6.12.

The friction coefficient and slip angle were estimated by the same estimators and are plotted in Figure 6.13. Again, the nonlinear observer shows delayed tracking of the friction coefficient when an abrupt change occurs and also shows loss of accuracy in estimating the slip angles on an icy surface. Due to the lack of sufficient excitation, converging to the true value does not take place until sufficient lateral excitation occurs, which may be the drawback of lateral dynamics based estimators given that lateral excitation may not be frequent or sufficiently intense in daily driving. However, when the excitation level is adequate, the estimators quickly produce accurate estimates.

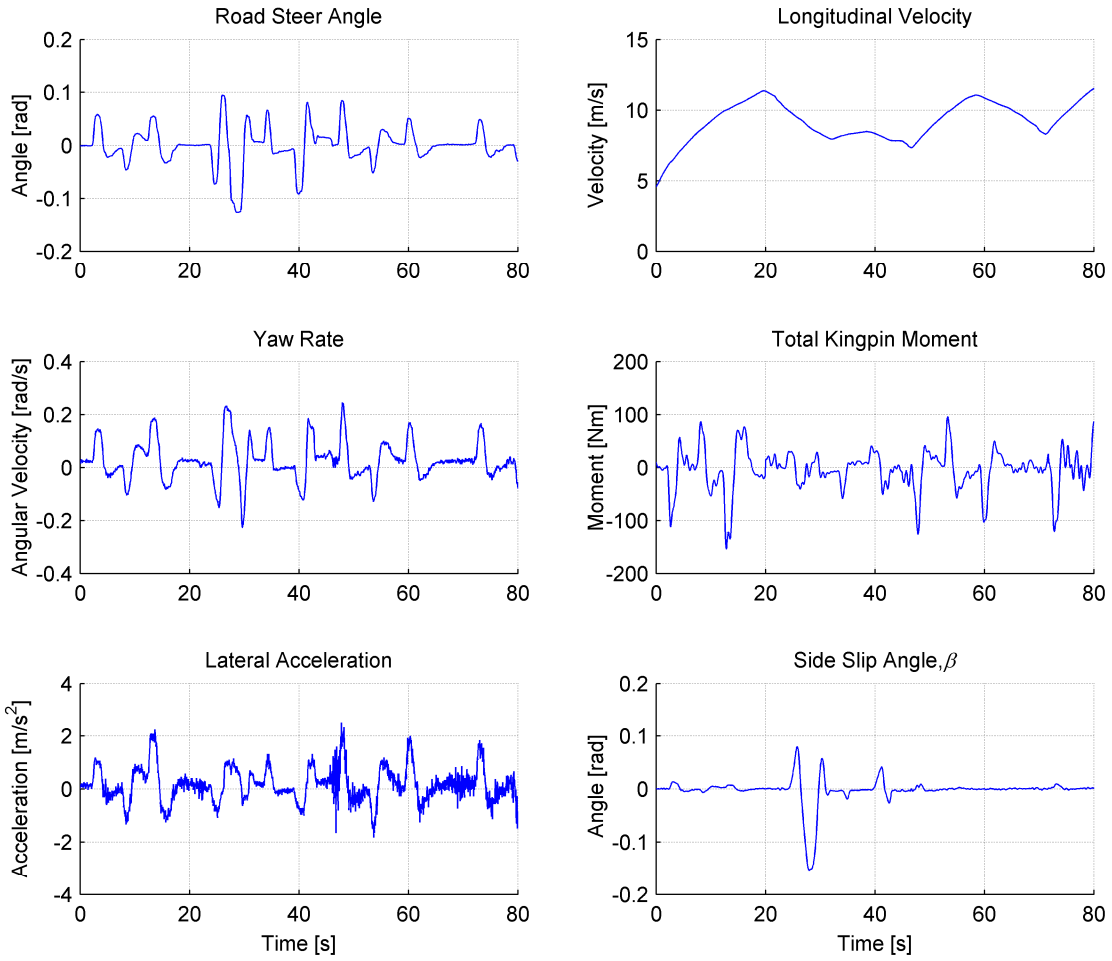

Figure 6.12 Measured signals of Test 6

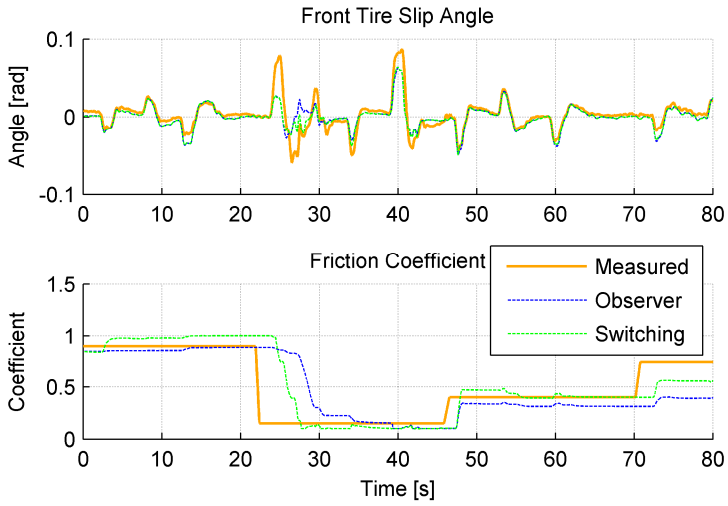

Figure 6.13 Evaluation of the lateral dynamics based algorithm using Test 6

6.4 Validation of the Longitudinal Dynamics Based Algorithm

The longitudinal dynamics based algorithm was evaluated on the same test surfaces used for the evaluation of the lateral based algorithms. During Test 7, the driver tried to simulate daily driving patterns, such as smooth acceleration and taking the foot off the gas pedal while coasting, with intermittent and small steering input for single lane changes. Test 7's measured signals are shown in Figure 6.14, where the vehicle lost stability on ice so that the driver turned the steering wheel excessively to stabilize the vehicle. Except for the instance of large steering that occurred on ice, this test maneuver represents daily driving behaviors such as slight acceleration, deceleration, and lane changes.

The estimation results of Test 7 are shown in Figure 6.15. The estimated longitudinal tire stiffness, a comparison of the estimated friction coefficient and measured coefficient, and time of activation of the algorithm are shown in the first, second and third plot, respectively. As we can see in the update signal plot, longitudinal excitations occur frequently, which is the major benefit of longitudinal dynamics based algorithms. The estimated friction coefficient generally tracks the measured coefficient due to rich excitation, except on ice. The estimator does not update the friction coefficient from 20 seconds to 32 seconds when adequate excitation does not exist.

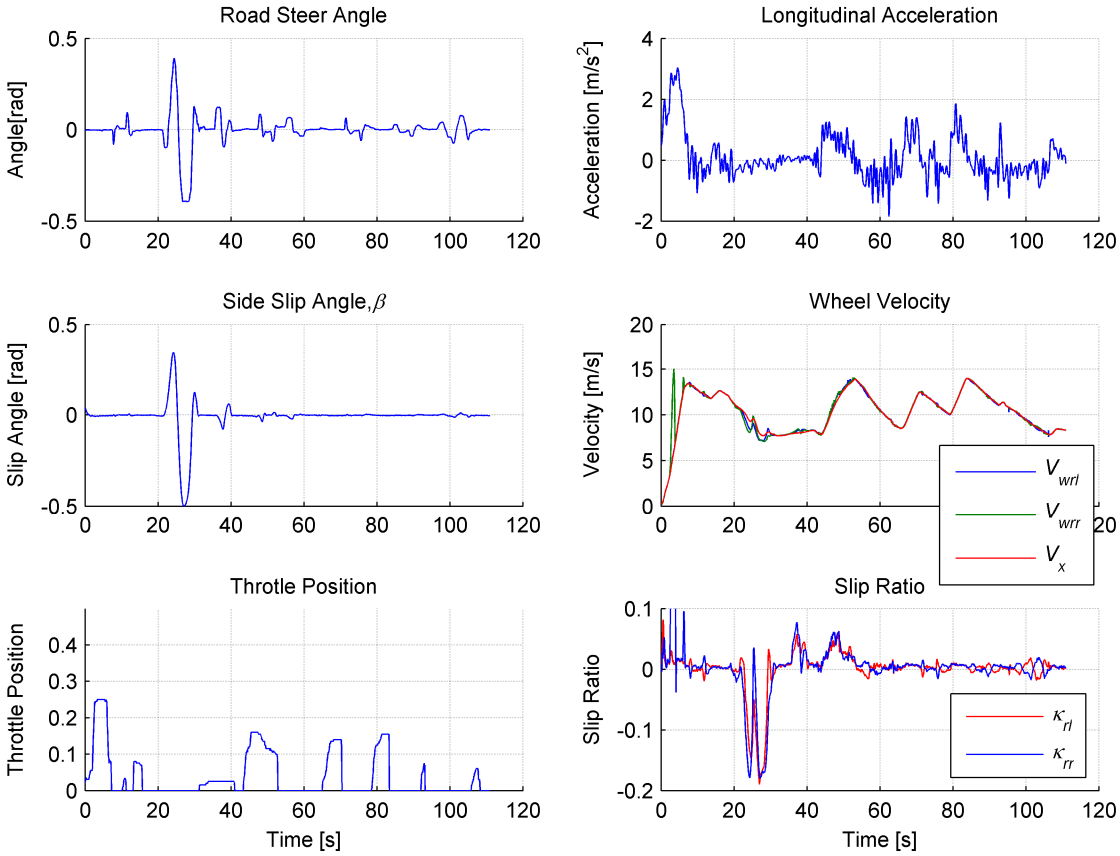

Figure 6.14 Measured signals of Test 7

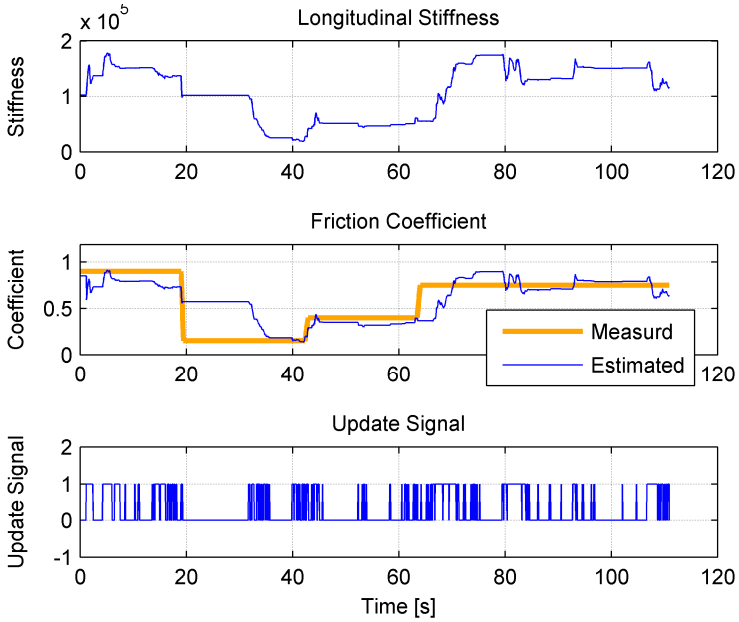

Figure 6.15 Evaluation of the longitudinal dynamics based algorithm using Test 7

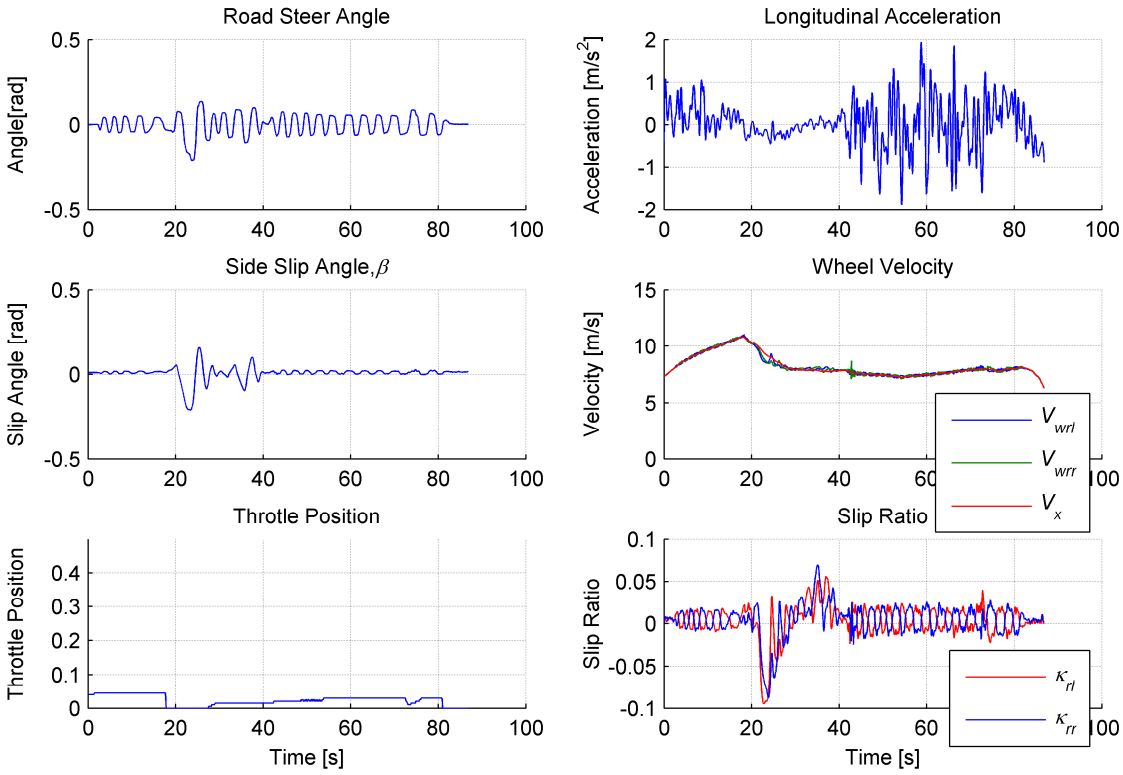

Figure 6.16 The signals related to longitudinal direction and measured during Test 5

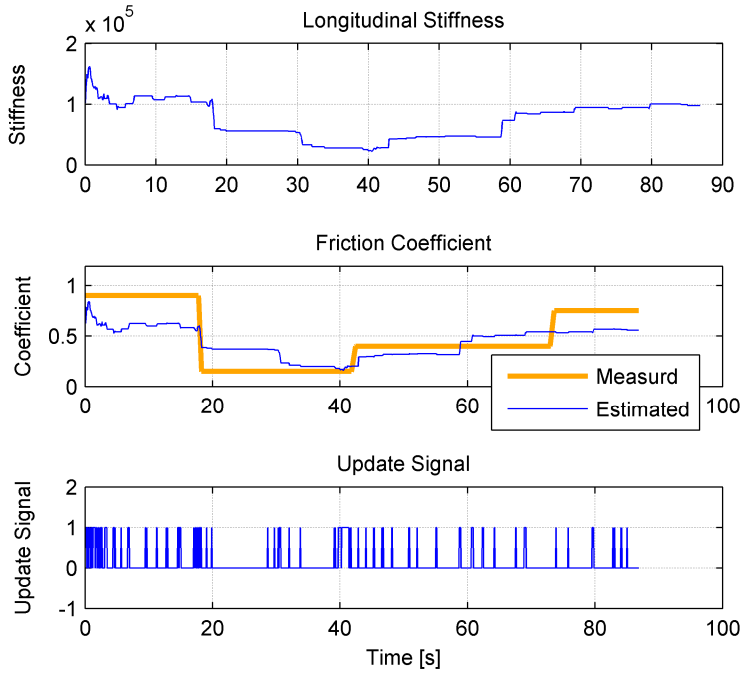

Figure 6.17 Evaluation of the longitudinal dynamics based algorithm using Test 5

In Test 7, the excitation was usually in the form of pure longitudinal acceleration. When combined slip occurred, such as acceleration with handling, the longitudinal tire force model in the linear range, introduced in (4.10) and Table 4.1, is no longer accurate . Therefore, use of the longitudinal dynamics based algorithm for Test 5, which has mainly lateral excitations, degrades the estimation accuracy, as shown in Figure 6.17.

6.5 Validation of the Integrated Algorithm

Test 8 was the main test conducted to the integrated algorithm, where both lateral and longitudinal excitations frequently exist but are not sufficient for either the lateral dynamic based algorithm or the longitudinal dynamic based algorithm. The measured signals of Test 8 are plotted in Figure 6.19.

Figure 6.20 shows the estimation results, which compared the three algorithms. As the longitudinal dynamics based algorithm does not estimate slip angle, only two algorithms are compared for the slip angle estimate. First of all, the longitudinal dynamics based algorithm is able to estimate the true friction coefficient when pure longitudinal excitation exists. If we look at the time between 20~30 seconds where only lateral excitations are rich, the longitudinal dynamics based algorithm does not update the estimated value; in this case, however, the lateral dynamics based algorithm has adequate excitation and its estimation is accurate. The integrated algorithm takes advantage of both excitations and thus has more chance to update the estimated value.

The other test conducted for evaluation is Test 5 and the measured signals were plotted in Figure 6.10 and Figure 6.16. In that test, we can see the benefit of integration much more clearly. The longitudinal dynamics based algorithm exhibits a very low level of accuracy of estimation due to the sparse occurrence of longitudinal excitation. The lateral dynamics based algorithm generally tracks the true friction coefficient well except during abrupt surface changes. The combination of algorithms improves the tracking performance because the integrated algorithm works with both excitations.

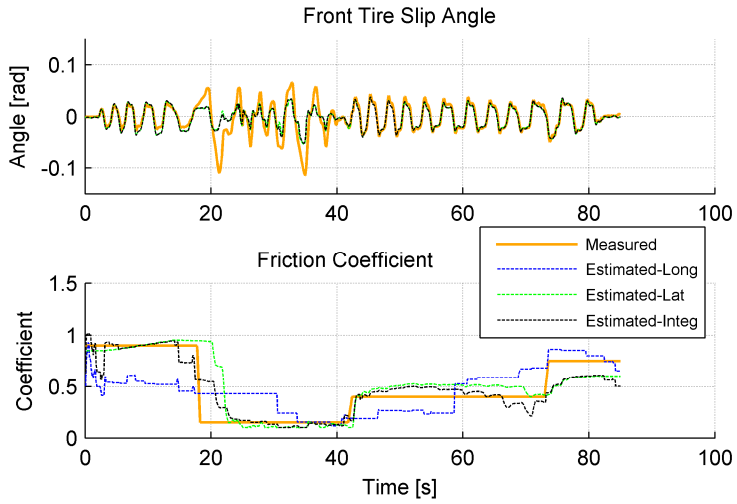

Figure 6.18 Comparison of three estimators using the data of Test 5

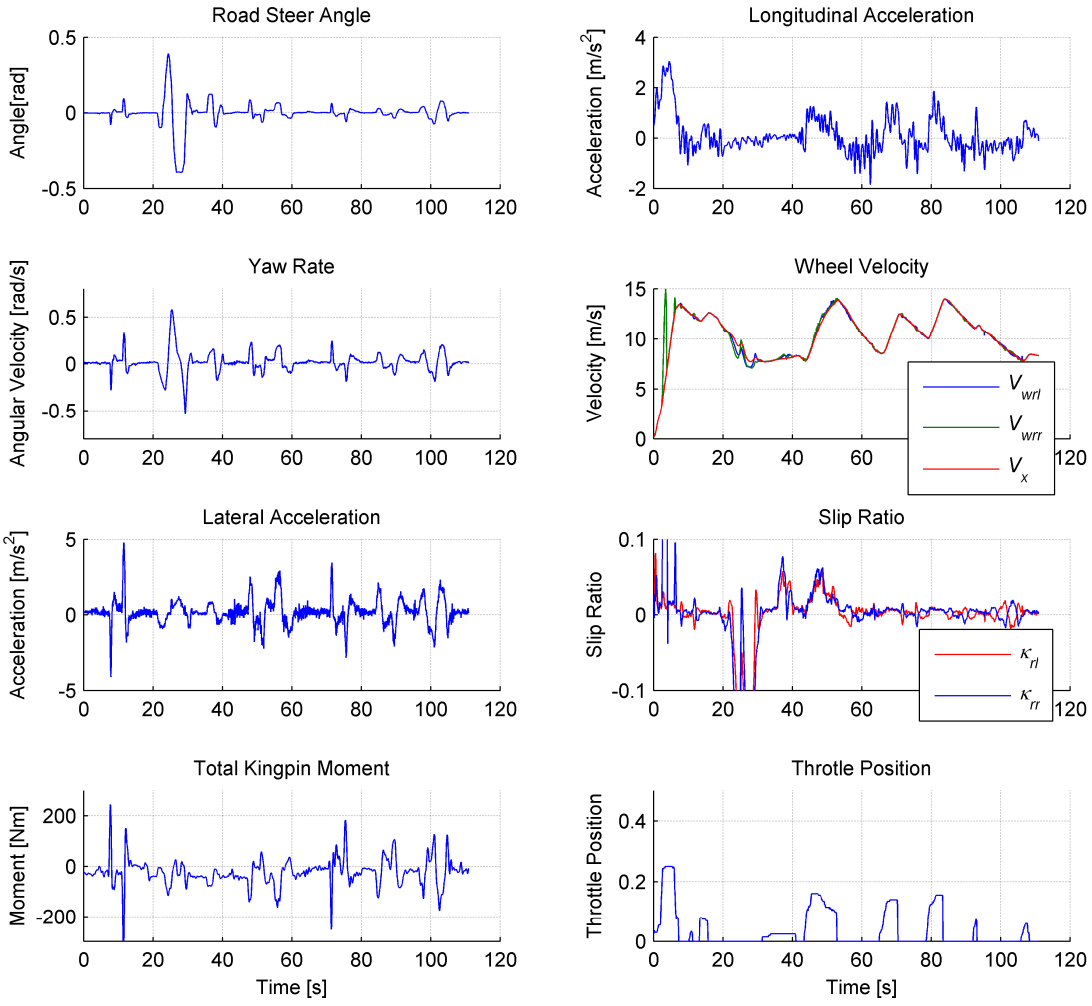

Figure 6.19 Measured signals of Test 8

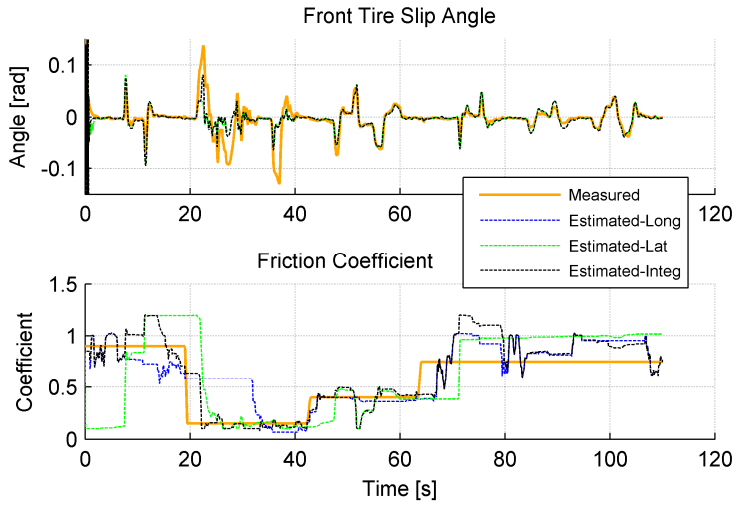

Figure 6.20 Comparison of three estimators using the data of Test 8

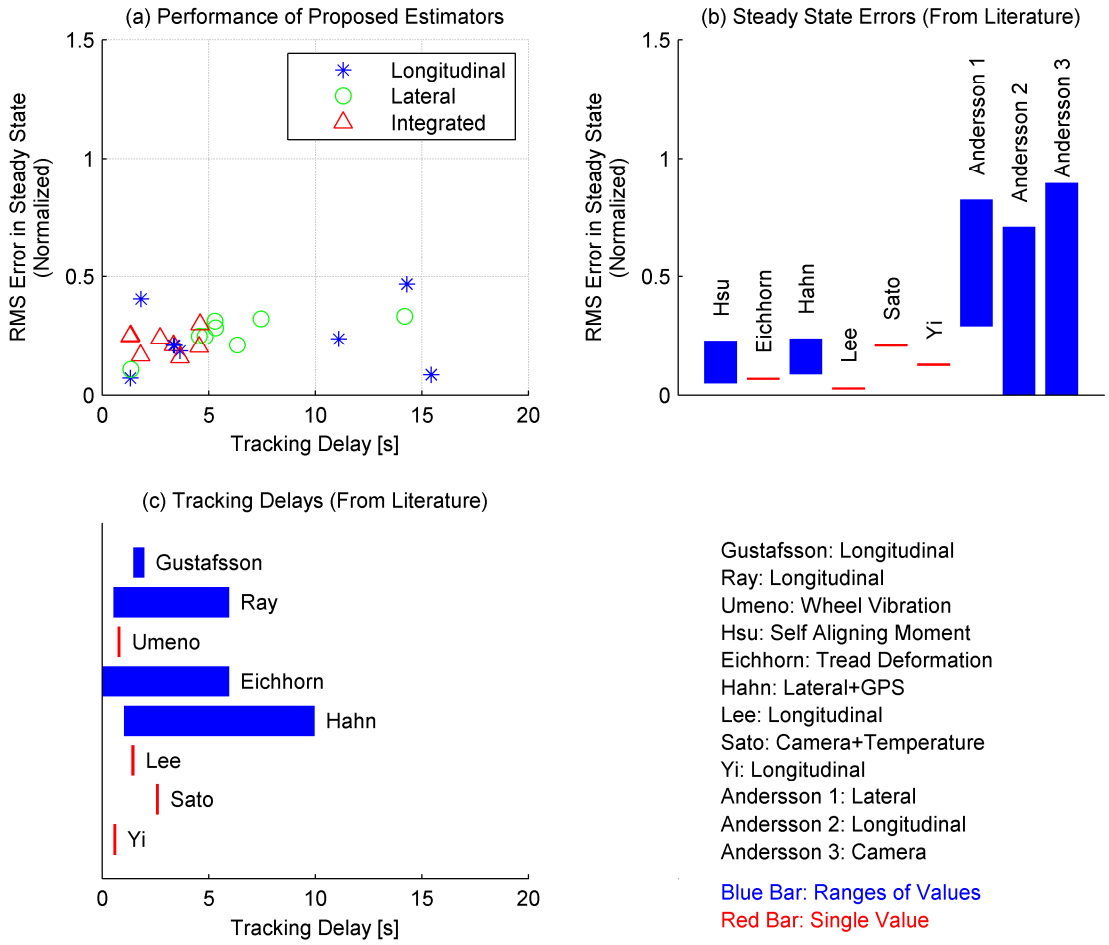

Figure 6.21 Performance of the integrated algorithm compared to the other excitation based algorithms, (a) and to the algorithms in literature, (b) and (c)

Figure 6.21 (a) shows comparisons between the integrated algorithm and the uni-directional excitation based algorithms, which are evaluated by using the same test data sets. The tracking delays are identified at the moments of surface changes and the steady state errors are identified on even surfaces. The integrated algorithm shows smaller distribution than the other two algorithms due to the wide range of preferable excitations. For the integrated algorithm, the steady state estimation errors are within 0.2~0.3 and the delays are within 1~5 seconds, whereas for the other two algorithms, the steady state estimation errors and the delays are distributed within 0.1~0.5 and 0~15 seconds, respectively. Figure 6.21 (b) and (c) show the steady state error and tracking delays obtained from literature [2, 7, 9, 15, 18, 20, 25, 26, 55, 59, 60], whose results may not be directly comparable to the performance of the estimators developed in this study because the surface conditions, tires, vehicles, and excitation conditions are not the same. However, if we consider that the test results in the literature were obtained under favorable excitations of their estimators, while we used test data emulating daily driving patterns, we can conclude that the integrated algorithm developed in this study shows a performance that is comparable to or even better than the performance of the algorithms found in the literature.

CHAPTER 7
CONCLUSION AND DIRECTION FOR FUTURE RESEARCH

7.1 Conclusion

Robust friction coefficient estimation algorithms are developed in this dissertation with the ultimate goal of improving the performance of vehicle active safety systems. These algorithms must produce accurate estimations in a wide range of vehicle states, be robust to plant uncertainties, and use sensors that are available on typical passenger cars. Two different approaches that are the main focus of this dissertation are lateral dynamics based algorithms and longitudinal dynamics based algorithms.

With respect to the lateral dynamics based methods, which are more robust to high frequency noises, a nonlinear least squares estimator and a nonlinear observer are proposed. The nonlinear least squares estimator is more accurate for estimation of the friction coefficients than the nonlinear observer, whereas, the latter is better for estimation of the slip angle. To improve tracking performance of friction coefficient estimation, two extended nonlinear observers are formulated. Furthermore, a design synthesis for robust nonlinear observers is developed using numerical implementation of Lyapunov stability conditions.

Regarding to the longitudinal dynamics based methods, identification of tire longitudinal stiffness is utilized to infer road friction. This approach is based on the observation that longitudinal tire stiffness is dependent on the friction coefficient, which is not well explained by most physics based tire models, such as the Brush model. The stress-strain relations in the tire contact patch are explored to explain the longitudinal tire stiffness, taking into account the effect of the friction coefficient leading to the finding that the pre-existing tire slip in the contact patch is likely to be the major reason that longitudinal tire stiffness is dependent on friction coefficient. The recursive least squares algorithm is utilized for identification of tire stiffness.

The original lateral and longitudinal dynamics based methods work well only under pure-slip excitation conditions. To increase the working range, the two algorithms are extended to work with combined slip conditions and are also integrated using switching rules.

The algorithms developed here are verified through extensive simulations in Carsim, a popular vehicle simulation software, and the use of experimental results. The identified friction coefficients and slip angles show reasonable accuracy. Depending on the excitation level, the delay in estimation convergence can be as long as a second. Reducing the estimation delay might be a possible topic further improvement.

7.2 Directions for Future Research

There are a few issues that remain to be solved before the proposed algorithms can be successfully implemented on production vehicles, including the following:

- Better side slip estimation using GPS

GPS (Global Positioning System) has become a popular vehicle navigation system. Though GPS is usually used for localization, the vehicle speed information provided by GPS is actually quite accurate (cm/sec) and could be further explored. Many algorithms to estimate vehicle states and parameters using GPS information have been published [18, 61, 62]. In addition, the availability and accuracy of GPS will be significantly improved when the Galileo system, the GNSS (Global Navigation Satellite System) project of EU, is brought online [63]. In the near future, there will be about 50 satellites instead of 24 from the EU and US GNSS system, which will improve the reliability of the position and speed measurements by orders of magnitude. Consequently, GPS will become a practical and affordable additional information sensor for vehicle state estimators. If we have vehicle lateral speed information, which was difficult to obtain and not accurately estimated with conventional methods, we can reduce one unknown variable in the estimation process and, in turn, the performance of the estimation algorithm will improve.

- Improvement of robustness in small excitation cases

The longitudinal dynamics based method has many advantages, the major one being the fact that it works using the small traction excitations present in daily driving. This approach, however, also has some drawbacks. The relationship between tire slip slope and road conditions depends on uncontrollable factors, such as tire pressure, tire wear, and the tire model. Thus, we need to know how these factors affect the relationship and how we can measure or identify these factors. Among these factors, tire pressure and tire wear affect the stiffness of tire lateral and longitudinal directions. Furthermore, tire pressure can be inferred using TPMS (Tire Pressure Monitoring System), which is almost standard on all new vehicles. Therefore, by detecting tire stiffness change and using the TPMS signals, we may be able to obtain information on a tire wear state. Using those identified factors, the relationship between the slip slope and road conditions can be adjusted, which will result in more robust estimation results.

- Verification of Performance Improvement of Active Safety Systems

Once we have a robust algorithm for estimation of the road friction coefficient, it can be used for control. Vehicle active safety systems, such as ABS, TCS and ESC, control the horizontal tire forces, which are heavily influenced by road friction. Current control algorithms are usually designed to be conservative due to the lack of road friction information. Knowledge of the friction coefficient can enable more sophisticated and precise control algorithms.

APPENDICES

Appendix A

Proof of Q>0

Fact 1:

$\begin{bmatrix} a & b \\ b & d \end{bmatrix} > 0$,if and only if, all eigenvalues are positive, i.e. $a+d>0$ and $ad-b^2>0$.

For a nonlinear system with an observer,

$$\begin{aligned} \dot{z} &= F(z,u), \\ y &= H(z,u), \\ \dot{\hat{z}} &= F(\hat{z},u) + L(\hat{z},u)\left(y - \hat{y}\right), \end{aligned}$$

where

$$F(z,u) = \begin{bmatrix} f(x, u, \theta) \\ 0 \end{bmatrix},$$

$$H(z,u) = \begin{bmatrix} h_1(x, u, \theta) \\ h_2(x, u, \theta) \end{bmatrix}.$$

The linearized system and measurement matrices are

$$A(\hat{z},u) = \left.\frac{\partial F(z,u)}{\partial z}\right|_{z=\hat{z}} = \begin{bmatrix} \dfrac{\partial f}{\partial x} & \dfrac{\partial f}{\partial \theta} \\ 0 & 0 \end{bmatrix}_{x=\hat{x},\theta=\hat{\theta}},$$

$$C(\hat{z},u) = \left.\frac{\partial H(z,u)}{\partial z}\right|_{z=\hat{z}} = \begin{bmatrix} \dfrac{\partial h_1}{\partial x} & \dfrac{\partial h_1}{\partial \theta} \\ \dfrac{\partial h_2}{\partial x} & \dfrac{\partial h_2}{\partial \theta} \end{bmatrix}_{x=\hat{x},\theta=\hat{\theta}},$$

Set $P=I$ and we have

$$Q = -\left\{(A-LC)^T + (A-LC)\right\} = \begin{bmatrix} q_1 & q_2 \\ q_2 & q_4 \end{bmatrix}, \tag{7.1}$$

where,

$$L = \begin{bmatrix} l_1 & l_2 \\ l_3 & l_4 \end{bmatrix},$$

$$q_1 = 2\left\{\left(l_1 \frac{\partial h_1}{\partial x} + l_2 \frac{\partial h_2}{\partial x} \right) - \frac{\partial f}{\partial x}\right\}\Bigg|_{x=\hat{x},\theta=\hat{\theta}},$$

$$q_2 = q_3 = \left(l_1 \frac{\partial h_1}{\partial \theta} + l_2 \frac{\partial h_2}{\partial \theta} + l_3 \frac{\partial h_1}{\partial x} + l_4 \frac{\partial h_2}{\partial x} \right) - \frac{\partial f}{\partial \theta}\Bigg|_{x=\hat{x},\theta=\hat{\theta}},$$

$$q_4 = 2\left(l_3 \frac{\partial h_1}{\partial \theta} + l_4 \frac{\partial h_2}{\partial \theta} \right)\Bigg|_{x=\hat{x},\theta=\hat{\theta}}.$$

Plug (3.25) into (7.1), then

$$q_1 + q_4 = 2k\left\{\left(\frac{\partial h_1}{\partial x}\right)^2 + \left(\frac{\partial h_2}{\partial x}\right)^2 + \left(\frac{\partial h_1}{\partial \theta}\right)^2 + \left(\frac{\partial h_2}{\partial \theta}\right)^2\right\}_{x=\hat{x},\theta=\hat{\theta}} \geq 0,$$

and

$$\begin{aligned} q_1 q_4 - {q_2}^2 &= 4k^2\left\{\left(\frac{\partial h_1}{\partial x}\right)^2 + \left(\frac{\partial h_1}{\partial \theta}\right)^2\right\}\left\{\left(\frac{\partial h_1}{\partial \theta}\right)^2 + \left(\frac{\partial h_2}{\partial \theta}\right)^2\right\} \\ &\quad - \left\{2k\left(\frac{\partial h_1}{\partial x}\frac{\partial h_1}{\partial \theta} + \frac{\partial h_2}{\partial x}\frac{\partial h_2}{\partial \theta}\right) + \frac{\partial f}{\partial x}\frac{\partial h_1}{\partial \theta}\Big/\frac{\partial h_1}{\partial x} - \frac{\partial f}{\partial \theta}\right\}^2 \\ &= 4k^2\left(\frac{\partial h_1}{\partial x}\frac{\partial h_2}{\partial \theta} - \frac{\partial h_1}{\partial \theta}\frac{\partial h_2}{\partial x}\right)^2 - 4k\left(\frac{\partial h_1}{\partial x}\frac{\partial h_1}{\partial \theta} + \frac{\partial h_2}{\partial x}\frac{\partial h_2}{\partial \theta}\right)\left(\frac{\partial f}{\partial x}\frac{\partial h_1}{\partial \theta}\Big/\frac{\partial h_1}{\partial x} - \frac{\partial f}{\partial \theta}\right) \\ &\quad - \left(\frac{\partial f}{\partial x}\frac{\partial h_1}{\partial \theta}\Big/\frac{\partial h_1}{\partial x} - \frac{\partial f}{\partial \theta}\right)^2 \\ &= 4k^2\left(\frac{\partial h_1}{\partial x}\frac{\partial h_2}{\partial \theta} - \frac{\partial h_1}{\partial \theta}\frac{\partial h_2}{\partial x}\right)^2 \geq 0. \end{aligned}$$

Therefore, from the Fact 1,

$$Q = \begin{bmatrix} q_1 & q_2 \\ q_2 & q_4 \end{bmatrix} \geq 0 \text{ with given } L \text{ and } P. \; Q.E.D.$$

BIBLIIOGRAPHY

[1] C. G. Wallman and H. Åström, "Friction measurement methods and the correlation between road friction and traffic safety. A literature review," Swedish National Road and Transport Research Institute, Linköping, Sweden, Technical Rep. VTI meddelande 911A, 2001.

[2] M. Andersson*, et al.*, "Road friction estimation," Intelligent Vehicle Safety Systems, Sweden, Project Rep. 2004:17750, 2007.

[3] NHTSA, "Federal motor vehicle safety standards; Electronic stability control systems; Controls and displays," NHTSA–200727662, 2007.

[4] M. Murphy, "Vehicle Dynamics: technologies and trends to 2015," Automotive World, London, UK 2007.

[5] H. B. Pacejka, "Tyre brush model," in *Tyre and Vehicle Dynamics*, 2nd ed Oxford, U.K.: Elsevier, 2005, pp. 93-134.

[6] F. Holzmann*, et al.*, "Predictive estimation of the road-tire friction coefficient," in *IEEE International Conference on Control Applications*, Munich, Germany, 2006, pp. 885-890.

[7] Y. Sato*, et al.*, "Study on recognition method for road friction condition," *JSAE Transaction,* vol. 38, pp. 51-56, 2007.

[8] M. Yamada*, et al.*, "Road surface condition detection technique based on image taken by camera attached to vehicle rearview mirror," *Review of Automotive Engineering,* vol. 26, pp. 163-168, 2005.

[9] U. Eichhorn and J. Roth, "Prediction and monitoring of tyre/road friction," in *FISITA*, London, U.K., 1992, pp. 67-74.

[10] A. Tuononen, "On-board estimation of dynamic tyre forces from optically measured tyre carcass deflections," *International Journal of Heavy Vehicle Systems,* vol. 16, pp. 362-378, 2009.

[11] A. Tuononen, "Vehicle lateral state estimation based on measured tyre forces," in *International Symposium on Dynamics of Vehicles on Roads and Tracks*, Stockholm, Sweden, 2009.

[12] M. Ito, *et al.*, "Estimation of road surface conditions using wheel speed behavior," in *International Symposium on Advanced Vehicle Control*, Tsukuba, Japan, 1994, pp. 533-538.

[13] F. Gustafsson, "Monitoring tire-road friction using the wheel slip," *IEEE Control Systems Magazine,* vol. 18, pp. 42-49, 1998.

[14] C.-S. Liu and H. Peng, "Road friction coefficient estimation for vehicle path prediction," *Vehicle System Dynamics,* vol. 25, pp. 413 - 425, 1996.

[15] T. Umeno, *et al.*, "Estimation of tire-road friction using tire vibration model," presented at the SAE 2002, Detroit, Michigan, USA, 2002.

[16] W. R. Pasterkamp and H. B. Pacejka, "The tyre as a sensor to estimate friction," *Vehicle System Dynamics,* vol. 27, pp. 409 - 422, 1997.

[17] C. Pal, *et al.*, "Application of neural networks in real time identification of dynamic structural response and prediction of road-friction coefficient from steady state automobile response," in *International Symposium on Advanced Vehicle Control*, Tokyo, Japan, 1994, pp. 527-532.

[18] J.-O. Hahn, *et al.*, "GPS-based real-time identification of tire-road friction coefficient," *IEEE Transactions on Control Systems Technology,* vol. 10, pp. 331-343, 2002.

[19] C. Sierra, *et al.*, "Cornering stiffness estimation based on vehicle lateral dynamics," *Vehicle System Dynamics,* vol. 44, pp. 24 - 38, 2006.

[20] K. Yi, *et al.*, "Estimation of tire-road friction using observer based identifiers," *Vehicle System Dynamics,* vol. 31, pp. 233 - 261, 1999.

[21] T. Umeno, "Detection of tire lateral force based on a resolver mechanism," *R&D Review of Toyota CRDL,* vol. 40, pp. 14-19, 2005.

[22] Y. Yasui, *et al.*, "Estimation of lateral grip margin based on self-aligning torque for vehicle dynamics enhancement," presented at the SAE 2004, Detroit, Michigan, USA, 2004.

[23] E. Ono, "Estimation and control of vehicle dynamics for active safety," *R&D Review of Toyota CRDL,* vol. 40, pp. 1-6, 2005.

[24] E. Ono, *et al.*, "Estimation of tire friction circle and vehicle dynamics integrated control for four-wheel distributed steering and four-wheel distributed traction/braking systems," *R&D Review of Toyota CRDL,* vol. 40, pp. 7-13, 2005.

[25] Y.-H. J. Hsu and J. C. Gerdes, "A feel for the road: A method to estimate tire parameters using steering torque," in *International Symposium on Advanced Vehicle Control*, Taipei, Taiwan, 2006.

[26] Y.-H. J. Hsu, *et al.*, "A method to estimate the friction coefficient and tire slip angle using steering torque," in *International Mechanical Engineering Congress and Exposition*, Chicago, IL, USA, 2006.

[27] H. E. Tseng, "Dynamic estimation of road bank angle," *Vehicle System Dynamics,* vol. 36, pp. 307-328, 2001.

[28] J. Ryu and J. Christian Gerdes, "Estimation of vehicle roll and road bank angle," in *American Control Conference*, Boston, MA, USA, 2004, pp. 2110-2115.

[29] H. B. Pacejka, "Semi-empirical tyre models," in *Tyre and Vehicle Dynamics*, 2nd ed Oxford, U.K.: Elsevier, 2005, pp. 156-215.

[30] H. Dugoff, *et al.*, "Tire performance characteristics affecting vehicle response to steering and braking control inputs. Final report," Highway Safety Research Institute, Ann Arbor, Michigan1969.

[31] C. Canudas de Wit and P. Tsiotras, "Dynamic tire friction models for vehicle traction control," in *IEEE International Conference on Decision and Control*, Phoenix, Arizona, USA, 1999, pp. 3746-3751.

[32] H. B. Pacejka, "The tread simulation model," in *Tyre and Vehicle Dynamics*, 2nd ed Oxford, U.K.: Elsevier, 2005, pp. 134-147.

[33] M. Grewal and A. Andrews, *Kalman filtering: theory and practice using MATLAB*: Wiley Online Library, 2001.

[34] J. Dakhlallah, *et al.*, "Tire-road forces estimation using extended kalman filter and sideslip angle evaluation," in *American Control Conference*, Seattle, Washington, USA, 2008.

[35] G. Baffet, *et al.*, "Sideslip angle, lateral tire force and road friction estimation in simulations and experiments," in *IEEE International Conference on Control Applications*, Munich, Germany, 2006, pp. 903-908.

[36] B. Friedland, "A nonlinear observer for estimating parameters in dynamic systems," *Automatica,* vol. 33, pp. 1525-1530, 1997.

[37] S. Raghavan and J. K. Hedrick, "Observer design for a class of nonlinear systems," *International Journal of Control,* vol. 59, pp. 515 - 528, 1994.

[38] H. K. Khalil, "Stability of Perturbed Systems," in *Nonlinear Systems*, 3rd ed Upper Saddle River, NJ: Prentice Hall, 2002.

[39] H. S. Bae, *et al.*, "Road grade and vehicle parameter estimation for longitudinal control using GPS," in *IEEE Intelligent Transportation Systems Conference*, Oakland, California, USA, 2001.

[40] H. K. Fathy, *et al.*, "Online vehicle mass estimation using recursive least squares and supervisory data extraction," *American Control Conference,* 2008.

[41] V. Winstead and I. V. Kolmanovsky, "Estimation of road grade and vehicle mass via model predictive control," in *IEEE Conference on Control Applications*, Toronto, Canada, 2005, pp. 1588-1593.

[42] A. Vahidi, *et al.*, "Recursive least squares with forgetting for online estimation of vehicle mass and road grade: theory and experiments," *Vehicle System Dynamics,* vol. 43, pp. 31 - 55, 2005.

[43] A. Balluchi, *et al.*, "Design of observers for hybrid systems," in *Hybrid ststems: computation and control*. vol. 2289, ed: Springer, 2002, pp. 76-89.

[44] C. R. Carlson and J. C. Gerdes, "Consistent nonlinear estimation of longitudinal tire stiffness and effective radius," *Control Systems Technology, IEEE Transactions on,* vol. 13, pp. 1010-1020, 2005.

[45] S. L. Miller, *et al.*, "Calculating longitudinal wheel slip and tire parameters using GPS velocity," in *American Control Conference*, Arlington, Virgina, USA, 2001, pp. 1800-1805.

[46] J. Wang, *et al.*, "Friction estimation on highway vehicles using longitudinal measurements," *Journal of Dynamic Systems, Measurement, and Control,* vol. 126, pp. 265-275, 2004.

[47] C. Canudas de Wit and R. Horowitz, "Observers for tire/road contact friction using only wheel angular velocity information," in *IEEE International Conference on Decision and Control*, Phoenix, Arizona, USA, 1999, pp. 3932-3937.

[48] C. Canudas de Wit, *et al.*, "A new model for control of systems with friction," *IEEE Transactions on Automatic Control,* vol. 40, pp. 419-425, 1995.

[49] J. Deur, *et al.*, "On low-slip tire friction behavior and modeling for different road conditions," in *IAVSD*, 2005.

[50] Y. Nakao and H. Kawasaki, "Estimation of friction levels between tire and road," presented at the SAE 2002 World Congress, Detroit, Michigan, USA, 2002.

[51] J. Svendenius, "Tire modeling and friction estimation," PhD, Department of Automatic Control, Lund University, Lund, 2007.

[52] D. Capra, *et al.*, "Experimental test of vehicle longitudinal velocity and road friction estimation for ABS system," presented at the SAE 2009 World Congress, Detroit, Michigan, USA, 2009.

[53] D. Sui and T. A. Hohansen, "Moving horizon estimation for tire-road friction during braking," in *IEEE Multi-conference of Systems and Control*, Yokohana, Japan, 2010.

[54] T. Dieckmann, "Assessment of road grip by way of measured wheel variables," in *FISITA*, London, 1992.

[55] F. Gustafsson, "Slip-based tire-road friction estimation," *Automatica,* vol. 33, pp. 1087-1099, 1997.

[56] S. K. Clark, *Mechanics of pneumatic tires*. Washington, D.C.: U.S. DOT, NHTSA, 1981.

[57] J. Y. Wong, *Theory of ground vehicles*. New York: John Wiley, 2001.

[58] S. Sastry and M. Bodson, *Adaptive control: stability, convergence, and robustness*. Englewood Cliffs, N.J.: Prentice Hall, 1989.

[59] L. R. Ray, "Nonlinear tire force estimation and road friction identification: simulation and experiments," *Automatica,* vol. 33, pp. 1819-1833, 1997.

[60] C. Lee*, et al.*, "Real time slip based estimation of maximum tire road friction coefficient," *IEEE/ASME Transactions on Mechatronics,* vol. 9, pp. 454-458, 2004.

[61] J. Ryu*, et al.*, "Vehicle sideslip and roll parameter estimation using GPS," in *International Symposium on Advanced Vehicle Control*, Hiroshima, Japan, 2002.

[62] D. M. Bevly*, et al.*, "The use of GPS based velocity measurements for measurement of sideslip and wheel slip," *Vehicle System Dynamics,* vol. 38, pp. 127 - 147, 2003.

[63] K. O'Keefe*, et al.*, "Global availability and reliability assessment of the GPS and galileo global navigation satellite systems," *Canadian Aeronautics and Space Journal,* vol. 48, pp. 123-132, 2002.